THE CHARACTERIZATION AND FEASIBILITY OF A LOW-DUTY-CYCLE DIAPHRAGMLESS SHOCK TUBE

A Thesis

by

DAVID CHRISTOPHER TAYLOR

Submitted to the Office of Graduate Studies of
Texas A&M University
in partial fulfillment of the requirements for the degree of

MASTER OF SCIENCE

August 2012

Major Subject: Aerospace Engineering

The Characterization and Feasibility of a Low-Duty-Cycle Diaphragmless Shock Tube

THE CHARACTERIZATION AND FEASIBILITY OF A LOW-DUTY-CYCLE DIAPHRAGMLESS SHOCK TUBE

A Thesis

by

DAVID CHRISTOPHER TAYLOR

Submitted to the Office of Graduate Studies of
Texas A&M University
in partial fulfillment of the requirements for the degree of

MASTER OF SCIENCE

Approved by:

Chair of Committee,	Rodney D. W. Bowersox
Committee Members,	Helen L. Reed
	Simon W. North
Head of Department,	Dimitris Lagoudas

August 2012

Major Subject: Aerospace Engineering

ABSTRACT

The Characterization and Feasibility of a Low-Duty-Cycle Diaphragmless Shock Tube.

(August 2012)

David Christopher Taylor, B.S., Texas A&M University

Chair of Advisory Committee: Dr. Rodney D. W. Bowersox

The feasibility and characterization of a novel diaphragmless shock tube was examined at the National Aerothermochemistry Laboratory at Texas A&M University. The goal was to design a facility that reliably produces shock waves through air in a repeatable manner sufficient for statistical analysis. The device is modular, automated, and compact. The proposed diaphragmless shock tube uses a shock wave generating mechanism that consists of a rotating door and locking cam-shaft system. The facility produced the desired driver gas pressures repeatedly to within 0.31% at low-duty-cycle of 6 seconds. The driven gas pressure profiles within the test-section suggest that shock waves may be forming within test section for a driver gas pressure of 200 psig and above, which corresponds to shock wave Mach numbers of 1.7 to 2.0. The measured wave speeds were within 3.1% of that predicted by ideal shock tube theory; however, the induced driven gas pressures within the constant pressure region were approximately half that expedited from ideal shock tube theory.

ACKNOWLEDGEMENTS

I would like to thank my committee chair, Dr. Rodney Bowersox, and my committee members, Dr. Helen Reed, and Dr. Simon North, for their guidance and support throughout the course of this research.

I want to thank my fiancée, friends, and colleagues, as well as, the department faculty and staff for making my time at Texas A&M University a great experience. I also want to extend my gratitude to the AFOSR (Col. R. Jefferies and Dr. Doug Smith) for sponsoring this study.

Finally, I thank Nicole Mendoza for completing much of the initial design and construction of the Shock Generator.

NOMENCLATURE

M_s	shock wave Mach number
ISTT	Ideal shock tube theory
P	Pressure
T	Time
DDPR	Driver gas pressure to driven gas pressure ratio
P4/P1	Driver gas pressure to driven gas pressure ratio
P4	Driver gas pressure
P1	Driven gas pressure
PSP	Post shock wave gas pressure
RD	Rotating door
RDLCV	Rotating door and locking cam-shaft valve
RCS	Rotating cam-shaft
RTDTR	Run time to down time ratio
CFT	Stainless steel compression fitting tube
CAC	Compressed air cylinders
NI	National Instruments
DAQ	Data acquisition unit
OPT	Omega pressure transducer
DnT	Driven gas pressure transducers
KPT	Kulite pressure transducers

LP	In-house Labview (Nation Instruments Corp.) program
RBDM	Rigid-body dynamics model
DPP	Driven gas pressure profiles

TABLE OF CONTENTS

Page

Page

LIST OF FIGURES

Page

LIST OF TABLES

1. INTRODUCTION

1.1. Motivation

Researchers have used traditional shock tubes and shock tunnels since the 1940s for a wide variety of research applications related to high-speed aerodynamics [1], gas dynamics [2], and chemical kinetics [3]. For a more complete description, see the Background Review in Section 2. A schematic of a traditional shock tube is given in Figure 1. In the simplest of terms, a shock tube consists of two pipes separated by a diaphragm. The driver section is on the left and the driven section is on the right. Once the pipes and diaphragm are joined together, the remaining open ends are closed. For a shock tunnel, a converging-diverging nozzle may be attached to the end of the driven section.

In order to operate the facility, a gas, often air or helium, is used to pressurize the driver section until the diaphragm ruptures. Once the diaphragm ruptures, the high-pressure driver gas is free to exhaust into the low pressure driven section.

The shock wave structure within the shock tube is predicted using unsteady gas-dynamics [2]. Ideal shock tube theory (ISTT), described in Anderson, is used herein to predict the shock wave and expansion fan structure shown in XT diagram of Figure 1 [4]. The XT diagram is produced from ISTT and depicts the time (y-axis) and location (x-axis) of the events inside a shock tube. Moreover, the XT diagram in Figure 1 shows that as the expansion fans move to the left they will eventually reflect off the back face of the driver section and move towards the right. This reflection will become important

This thesis follows the style of the *AIAA Journal.*

in Section 6. The driver gas pressure to driven gas pressure ratio (DDPR) dictates the speeds of these two waves, whereby the higher the DDPR, the faster wave speeds. The contact surface illustrated in Figure 1 represents the boundary between the driver gas and the driven gas in time and space.

The coalescence of compression waves creates the shock wave; therefore, if the diaphragm opens instantaneously then the compression waves will coalesce instantaneously (assumption in ISTT). However, if the diaphragm has a finite opening time, which is more conducive to reality, then the compression waves will coalesce at a time and a place downstream of the ruptured diaphragm. The location downstream of the broken diaphragm where the shock wave forms is the shock wave formation distance.

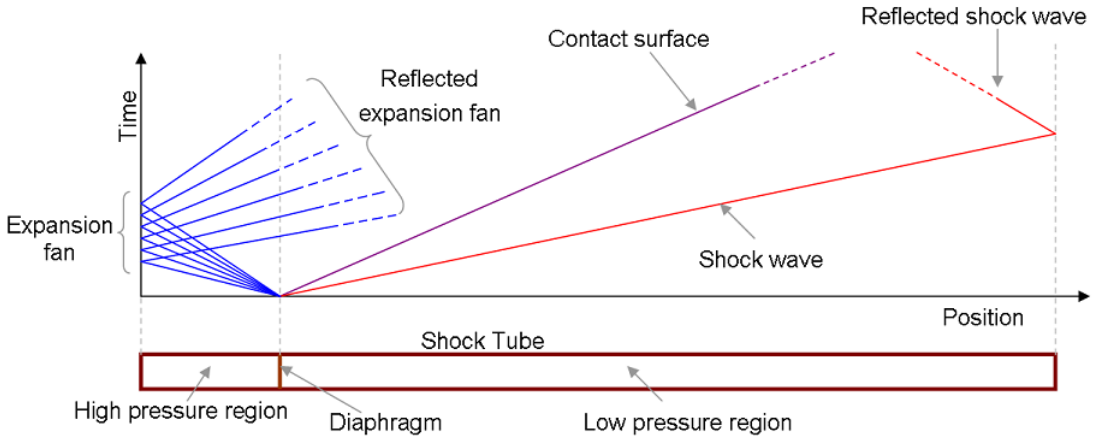

Figure 1 Traditional Shock Tube [5]

Statistical analyses of impulsive shock wave driven, unsteady flows are of both scientific and technical interest. However, statistical analyses in traditional shock tubes

are prohibitively time consuming due to the length of time required to replace diaphragms. In addition, diaphragm materials and machining costs can become exorbitant. Further detail is in Section 2.1.

As a result, a low-duty-cycle diaphragmless shock tube is desirable. Based on a review of the literature, three types of diaphragmless shock tube designs were identified, all of which have different performance characteristics. The following four metrics are often used to characterize the quality of performance:

1. Accuracy as compared to ideal shock tube theory
2. Repeatability from one run to the next
3. Shock wave Mach number range
4. Shock wave formation distance

To date, none of the current diaphragmless shock tube designs identified in the literature review performs well in all four categories; see the review in Section 2.2. Thus, providing a new diaphragmless shock tube concept that has balanced performance is the focus of this study. Furthermore, the U.S. Air Force has interest in fast opening diaphragmless valves for Ludweig tunnel operations and dynamic sensor calibration through impulsively driven shock waves at modest speeds are useful for the laboratory.

1.2. Research Objective and Approach

The objective of this research project is to investigate the feasibility of a novel repeatable diaphragmless shock tube facility for statistical experiments by completing a performance characterization study. The basic concept of this novel shock tube is based

on the operation of a new fast-acting valve concept, developed at TAMU that uses a rotating door and locking cam-shaft valve (RDLCV) system to generate shock waves. The rotating door (RD) operates like a valve by allowing the driver gas to accelerate the RD to an open position when a rotating cam-shaft (RCS) rotates to a position that allows the RD to freely move. After the driver gas has been expelled, the RD is returned to its original closed position via the force of gravity. The RCS then compresses the RD onto an O-ring (locking it into place) to form a sealed driver section ready for another cycle. Thus, the cycle is repeatable. For more details on the rotating door and locking cam-shaft mechanism, see Section 4. The tasks necessary to meet the project objective are:

- Design, construct, and instrument a prototype system
- Assess the performance as compared to ideal shock tube theory (ISTT)

1.3. Expected Contributions

The primary contribution from this master's thesis project is the performance characterization and feasibility determination of the novel rotating door and locking cam-shaft valve (RDLCV) concept as the shock wave generating mechanism for a low-duty-cycle repeatable shock tube. If successful, then the low-duty-cycle diaphragmless shock tube will permit new unsteady gas dynamic experiments that a statistical quantification to be conducted. Such experiments are designed to study shear mixing layers, shock wave formation phenomena, and high-temperature channel flow. Furthermore, if successful, the RDLCV mechanism can be used as a fast acting valve for U.S. Air Force Ludweig tunnel operations. Moreover, the facility could be used to produce impulsively driven shock waves at modest speeds that are useful for dynamic

sensor calibration. A more complete description of the background review, the facility design and RDLCV apparatus, as well as results to date, is in the following sections.

2. BACKGROUND REVIEW

2.1. Evolution of the Traditional Shock Tube Design

Shock tubes have been around since the 1940s and are used extensively for research involving high-speed aerodynamics [1], gas dynamics [2], chemical kinetics [3], non-equilibrium processes [6], re-entry flows [7], multi-phase [8] and multi-gas [2] flows, shock wave interaction [9], and shock wave propagation [10]. Furthermore, shock tubes are used as wind tunnels for application-driven supersonic and hypersonic research involving re-entry vehicles, ramjets, and scramjets, because shock tubes are able to recreate flight conditions for millisecond time intervals. Shock tubes also have a relatively low setup cost versus the high setup costs of traditional wind tunnels, which offer multi-second run times. As a result, shock tubes are valuable test facilities; however, they have at least three persistent drawbacks.

2.1.1. 1st Drawback

The first drawback to traditional shock tubes is that the mechanism used to generate shock waves does not form the same shock wave every time; thus, each run must be treated as a separate statistical event. The inconsistency between runs is a result of the destructive mechanism used to create each shock wave, wherein a diaphragm, which is generally made from metal or Mylar, is broken by the pressure differential between the driver and driven sections of the shock tube. Since the diaphragm is broken, it can only be used for one run and, thus, must be replaced before each new run. Additionally, each diaphragm has unique characteristics, ranging from the material

impurities within each diaphragm to the manufacturing inconsistencies of each diaphragm. Therefore, each diaphragm has unique opening characteristics, leading to the production of unique shock waves, which results in unique flow fields downstream of the diaphragm.

As a result, researchers have devised methods for controlling the manner in which a diaphragm bursts (how) and the pressure differential at which a diaphragm ruptures (when). One such method for controlling the manner in which the diaphragm breaks is a manufacturing technique that creates “failure paths” by scoring the surface of the diaphragm. The depth and pattern of the score controls the pressure differential at which the diaphragm bursts, i.e., the burst pressure differential. Typically, diaphragms are scored in an “X” pattern to create four triangular petals that bend out of the flow path as the driver gas travels through the driven section, as illustrated in Figure 2. Each of these petals opens differently and at a different rate with respect to each other and from one run to the next. In some cases, a petal may break off and tumble down the shock tube, potentially damaging the shock tube, instruments, or models. However, this technique ensures the creation of four petals every time. Therefore, this technique aids in fabricating diaphragms with similar opening characteristics [3].

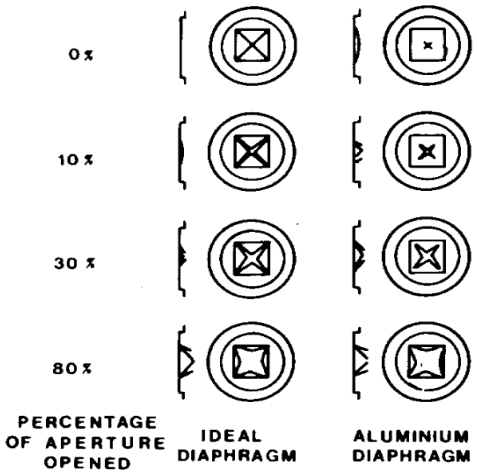

Figure 2 Diaphragm Opening Order [11]

Over time, innovative approaches have been developed to overcome the violent nature of the diaphragm bursting mechanism and the unpredictability of the manner and conditions under which the diaphragm ruptures. Two common methods for controlling how and when the diaphragm ruptures are the puncturing method and the double diaphragm method. The puncturing method uses an apparatus that cuts the diaphragm once the desired driver gas pressure is achieved. The puncturing device can be in either the driver section or the driven section of the shock tube. However, this forces the flow to move around the apparatus, because it is in the flow field, causing flow disturbances and unsteadiness. Therefore, this approach is unfavorable. The double diaphragm method replaces the traditional single diaphragm holder with one that holds a single diaphragm on either side. The chamber between the two diaphragms is pressurized to roughly half the pressure differential required to break each diaphragm. Then the driver is pressurized until the desired driver gas pressure is reached. Venting the chamber

between the diaphragms causes the two diaphragms to burst in succession. Roughly one shock tune diameter separates the two diaphragms, which ensures that, when the first diaphragm breaks, it does not hit the second diaphragm thus ensuring that only the pressure deferential ruptures each diaphragm.

The benefit of the double diaphragm method over all previously mentioned methods is that it facilitates control over the time and pressure at which the diaphragms will rupture. Furthermore, due to the sudden exposure to a large pressure differential, the diaphragm opening characteristics from one run to another become more similar because each diaphragm is made to burst at roughly half the driver gas pressure. Moreover, the lower rated driver gas pressure diaphragms tend to have lower material and manufacturing costs. Although this method is non-intrusive, it uses two diaphragms, which leads to a higher upkeep cost and longer down time. Nevertheless, because of these improvements and others, traditional shock tubes now form comparable shock waves from one run to the next, which enables statistical measurements to be conducted.

2.1.2. 2nd Drawback

The second drawback with traditional shock tubes is that the ratio of run time (~milliseconds) to down time (~minutes) is very low when compared the ratio of run time (~multi-second) to down time (~minutes) of traditional wind tunnels. The down time of traditional shock tubes is due to the time necessary to change out diaphragms, while the down time for traditional wind tunnels is dependent upon the time necessary to recharge the air supply. The run time to down time ratio (RTDTR) in traditional shock tubes is a problem because many experiments require a statistical analysis for various

reasons, such as gathering information for phenomenon modeling and reducing measurement uncertainties. However, regardless of the reason for using statistics, all statistical analyses require hundreds or even thousands of runs. As a result, methods have been developed that decrease the down time for traditional shock tubes, such as using fewer bolts to hold the diaphragm(s) in place or using a diaphragm holder that slides into place. However, these methods are still very time-consuming, thus result in a relatively low RTDTR when compared to the RTDTR of traditional wind tunnels.

2.1.3. 3rd Drawback

The third drawback with traditional shock tubes is the cost of disposable diaphragms and their direct effect on the upkeep cost of the traditional shock tube. Furthermore, this cost increases as the driver gas pressure increases because diaphragms that are designed to burst at higher pressure differentials are often made from thicker and heavier metals. Thus, a method that lowers the upkeep cost of a traditional shock tube is very desirable.

2.2. Diaphragmless Repeatable Shock Tubes Designs

Consequently, the drawbacks of the traditional shock tube design outlined above motivated studies in repeatable diaphragmless shock tube solutions with relatively short down time. To date, all solutions incorporate some type of fast-acting value. However, each fast-acting value solution has different performance characteristics, which make it suitable for certain applications. To quantify and categorize the performance of each type of shock tube, the performance metrics used are as follows:

1. Accuracy – how close the shock wave strengths are compared to ideal shock tube theory (ISTT)
2. Repeatability – the amount of variance or jitter between runs
3. Shock wave Mach number range – the range of shock wave Mach numbers the shock tube can operate
4. The shock wave formation distance – the downstream distance from the diaphragm needed for a shock wave to fully form

For comparison, from Section 1, traditional shock tubes have been designed that produce short forming highly accurate shock waves over a large range of shock wave Mach numbers (M_s). However, traditional shock tubes have a poor repeatability.

To date, there are three categories of repeatable diaphragmless shock tubes, excluding free piston and combustion driven shock tubes. The first type of repeatable diaphragmless shock tube, and by far the most common, is a piston-driven fast-acting valve, wherein the driver and driven sections are concentric cylinders that share one end with the diaphragm section containing a sliding piston. Kosig et al. (1999) uses a piston that is held in place by hydraulic brakes that, when released, allows the driver gas to push the piston back into a vacuum cavity located behind the piston, thus allowing the driver gas to turn 180 degrees and escape into the driven section. It produces shock waves that are accurate to from 1% to 9% of ISTT. It is capable of producing $1.1 \leq M_s \leq 2.0$ for air and $M_s \leq 5.0$ for lighter driver gases such as helium. The shock waves form at 20-40 tube diameters downstream [12]. Rêgo et al. (2007) uses a piston held in place by an auxiliary pressure chamber, instead of a vacuum cavity and brake, located behind the

piston that allows the driver gas to accelerate the piston once the pressure in the auxiliary pressure cavity is vented. As the driver gas pushes the piston backward, the gas turns 180 degrees into the driven section and eventually forms a shock wave [13]. This design also produces $2.0 \leq M_s \leq 5.0$ using helium but within 20% to 38% of ISTT. There was no mention of shock wave formation distance, repeatability, or the use of air as the driver gas. One drawback with both of these designs and all fast acting valve designs, including the valve that is the subject of this project, is that they are limited by the time it takes for the valve to move from the closed position to the open position; therefore, shock waves may only form if the valve moves fast enough [12]. Furthermore, as the opening time increases the shock formation distance increases [1]. Another drawback with the piston design is the vibrations that occur when the piston undergoes a sudden stop at the open position, which also causes fatigue in the piston. These vibrations can excite measurement equipment in the shock tube, leading to measurement errors. Tranter et al. uses a third bellows type mechanism for releasing the piston. However, they did not report performance data for the facility [3].

The second type of repeatable diaphragmless shock tube is a spring-loaded piston design. This design allows the driver section and driven section to be in-line with each other. This design, used by Kashitani et al. (2010), produces shock waves at $1.2 \leq M_s \leq 2.1$ with air and within 11%-30% of ISTT. Kashitani's design also has a repeatability of < 1% with shock wave formation distances of 20-100 tube diameters downstream of the piston valve. The benefit of this piston design over the other piston designs is that the

flow must only flow around the piston and not turn 180 degrees. This difference results in steadier flows in the driven section [1].

The third type of repeatable diaphragmless shock tube utilizes a flexible diaphragm. The configuration of the driver section and driven section, as well the auxiliary pressure chamber, is in the same configuration as the piston design used by Rêgo et al. described above. However, the flexible diaphragm type may be preferred over the piston type because the flexible diaphragm is much lighter than the piston, thus, opens much faster and causes weaker wall vibrations. This may result in shorter shock wave formation distances and greater repeatability. Hosseini et al. (2000) uses a flexible membrane and reports a repeatability of 0.2% using helium driver gas, and states that it is very low compared to traditional shock tubes. The flexible membrane also produces shock waves within 5% of ISTT using air as the driver gas and within 1% of ISTT using helium as the driver gas. However, the fatigue life of the flexible diaphragm is much shorter than the fatigue life of the piston. Furthermore, the material's elasticity severely limits the shock wave Mach number range, $1.15 \leq M_s \leq 1.35$ using air as the driver gas and $1.1 \leq M_s \leq 1.7$ using helium as the driver gas. There was no reported information on shock wave formation distance [14].

3. LOW-DUTY-CYCLE SHOCK TUBE CONCEPT

3.1. Objectives

As indicated in the previous section, all diaphragmless shock wave generating methods have some limitation. Hence, none were deemed acceptable for our plans to study unsteady shear mixing layers and shock wave formation phenomena though statistical analyses. Therefore, a novel shock tube design tailored to our applications was necessary. The objectives for this new system are as follows:

1. Two-dimension flow through the test section for planned studies
2. Low-duty-cycles for rapid acquisition for statistical measurements
3. Rapid shock waves formation for a compact design such that it would fit on a single optical table
4. Accurate shock waves as compared to ideal shock tube theory (ISTT)

To meet these objectives, the new shock tube design must include

1. A smooth and continuous connection from the driver section to the driven section with no obstructions
2. A shock wave generating apparatus with an opening time comparable to a traditional diaphragm, 0.2 to 0.8 milliseconds [11][15][16]
3. A shock wave generating mechanism that is repeatable
4. A mechanism that seals the driver section such that the shock wave Mach number range is maximized

Therefore, in order to accommodate all of the design constraints, a simple concept based on an in-line rectangular cross section driver section and driven section with a rotating door and a locking cam-shaft valve (RDLCV) mechanism was conceived.[1]

3.2. New Shock Tube Concept

The basic notion behind the concept is that a single rotating door (RD) mimics the single petal opening in a conventional scored diaphragm as illustrated in Figure 2. The high-aspect ratio of the rectangular cross section facilitates planar two-dimensional flow throughout the shock tube and has the additional benefit of lowering the rotational inertia of the RD when compared to circular and square cross sections with the same surface area. The lower rotational inertia of the rectangular cross section enables the RD to open faster, resulting in the formation of more accurate shock waves when compared to ideal shock tube theory (ISTT) and at shorter shock wave formation distances. Additionally, the rotating door and locking cam-shaft valve (RDLCV) mechanism enables the sealing of the driver section at a wide range of driver gas pressures thus providing a dynamic range of shock wave Mach numbers (M_s). Moreover, the duty-cycle of the device becomes dependent on the speed at which the driver section can be pressurized and the rotational speed of the RCS.

In the present novel shock tube design known as the Shock Generator (SG), the rotating door (RD) rotates upward from the applied pressure force of the escaping driver gas and then falls back down via the force of gravity. By allowing gravity to close the

[1] Nicole Mendoza, a companion PhD student within the Texas A&M University Aerospace Engineering Department, performed the original design.

RD, the system becomes less complicated. A rotating cam-shaft (RCS) was chosen as the RD's locking and releasing mechanism because the RCS is designed to have two sections, the cutout section and uncut section. The uncut section is a simple cylinder that applies a uniform force along the bottom of the RD. Therefore, the RCS can lock the RD in place until the RCS's cutout section lines up with the bottom of the RD. The alignment between the cutout section and the RD enables the RD to rotate open. Further detail on the rotating door and locking cam-shaft valve (RDLCV) mechanism is provided in Section 4. Therefore, the system allows for both a high degree of repeatability and low-duty-cycles between runs as long as the driver gas pressure is consistent every cycle, which will be shown to be the case is the Results Section (Section 6).

To provide a smooth and continuous flow path from the driver section to driven section, the flow path is kept free of turns and obstructions. The Shock Generator (SG) accomplishes this by stopping the rotating door (RD) in its open position by a rubber wedge that has the appropriate angle to provide a smooth and continuous flow path from the driver section to the driven section. Further details are provided in Section 4.2.5.

3.3. Optimizing the Rotating Door Design

To provide a RD that meets the proposed requirements, the RD must rotate out of the flow path on the order of milliseconds. Unfortunately, the RDLCV is similar to all fast-acting values in that the performance is dependent upon the opening time of the mechanism. For the RD, the opening time is dependent upon the difference in applied force between the driver gas pressure and the driven gas pressure. Therefore, designing

the RD appropriately becomes critical. The RD design must satisfy the two following opposing criteria:

1. Have the smallest rotational inertia as possible for rapid opening times.
2. Have a rigid enough structure that ensures a sealed driver section with driver gas pressures up to 500 psig.

The driver gas pressure of 500 psig is the upper tested limit of this study. Furthermore, in order to provide a properly sealed driver section at the desired driver gas pressures, the RD must only be allowed to deflect minimally (Ø1/1000”). Therefore, an optimal rotating door design is essential.

In order to determine the optimal RD design a two-step analytical design approach was taken. First, a three-dimensional model of the RD was designed in SolidWorks (Dassault Systèmes) and then structurally analyzed using the finite element structural analysis software called Abaqus (Dassault Systèmes). The structural analysis ensures that the RD’s geometry will provide the necessary sealing surface for all desired driver gas pressures. Next, an in-house Matlab (The MathWorks, Inc.) code calculates the RD’s opening time based on a rigid-body dynamics model (RBDM) of the RD. The RBDM considers the forces and moments on the RD from the driver gas pressure. Additionally, the RBDM requires five input parameters obtained from the three-dimensional SolidWorks model (Dassault Systèmes), which are the:

1. RD’s mass (m)
2. RD’s center of mass location relative to the center of the hinge location (r_{cg})
3. RD’s moment of inertial of the z plane along the z axis or rotational inertia (I_{zz})

4. Driver gas pressure surface area exposed to the back face of the RD (A)
5. Driver gas center of pressure location relative to the center of the RD's hinge location (r_{cp})

These design parameters close the following equations of motion to provide a theoretical model for the opening time for the RD, where "P" and "g" represent the driver gas pressure and the acceleration due to gravity, respectively.

$$F_{gravity} = m \cdot g = \left[kg \cdot \frac{m}{s^2}\right] = [N] \tag{3.1}$$

$$F_{pressure} = P \cdot A = \left[\frac{kg\frac{m}{s^2}}{m^2} \cdot m^2\right] = [N] \tag{3.2}$$

$$M_{gravity} = F_{gravity} \cdot r_{cg} = [N \cdot m] \tag{3.3}$$

$$M_{pressure} = F_{pressure} \cdot r_{cp} = [N \cdot m] \tag{3.4}$$

$$Rate_{gravity} = \frac{M_{gravity}}{I_{zz}} = \left[\frac{kg \cdot \frac{m}{s^2} \cdot m}{kg \cdot m^2}\right] = [s^{-2}] \tag{3.5}$$

$$Rate_{pressure} = \frac{M_{pressure}}{I_{zz}} = \left[\frac{kg \cdot \frac{m}{s^2} \cdot m}{kg \cdot m^2}\right] = [s^{-2}] \tag{3.6}$$

Once the two rate equations are established, the Matlab ODE45 solver function (The MathWorks, Inc.) solves the following equation for the angular position of the RD around the z axis denoted by "θ_z" as a function time.

$$Torque = Rate_{pressure} \cdot \cos(\theta_z) - Rate_{gravity} \cdot \sin(\theta_z) \tag{3.7}$$

When the angular position is greater than $\pi/2$ the RD has fully opened. Therefore, the time at which the RD opened is easily obtained. Presented in Figure 3 are the opening

times (y-axis) for the final designs, titanium and aluminum, as a function of driver gas pressure (x-axis).

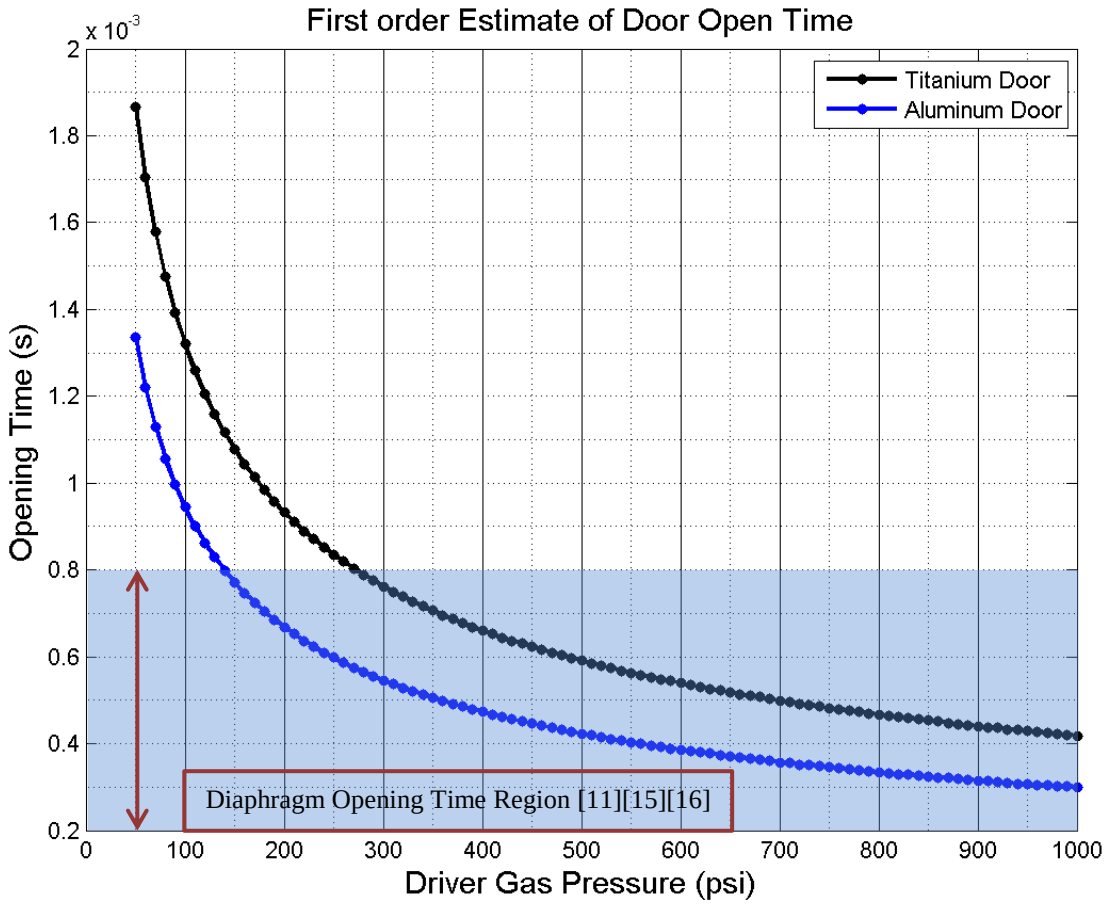

Figure 3 Rotating Door's Rotational Rate

Therefore, the RD's theoretical opening time model is a tool that predicts the minimum driver gas pressure that allows the Shock Generator (SG) to produce shock waves. Because traditional diaphragms open anywhere from 0.2 to 0.8 milliseconds, if the RD opens in less than 0.8 milliseconds then the SG should produce a shock wave

[11][15][16]. This provides the lower operational limit of the SG. The driver section O-ring seal, discussed in more detail in the Section 4.2, determines the upper operational limit of the SG.

From the two-step analytical design approach, two designs were deemed acceptable for testing. One made from aluminum and the other made from titanium. Both of these designs have comparable opening times as illustrated in Figure 3. From Figure 3, it is clear that the aluminum RD design outperforms the titanium RD design for all driver gas pressures, which is a result of the density in aluminum being lower than in titanium, thus the rotational inertial is lowered. However, prior to the design of the aluminum RD, the titanium RD was tested and fractured during testing due to its low ductility. Therefore, the aluminum RD design is the RD design considered for the remainder of the study.

From Figure 3, the aluminum RD design has a maximum opening time on the order of a millisecond for the lowest driver gas pressure. However, from Figure 3, it is clear that for driver gas pressures above 150 psig the aluminum RD falls into the regime of traditional diaphragm open times. Furthermore, as Figure 3 illustrates, the opening time decreases exponentially with increasing driver pressure.

As mentioned above, the driver section O-ring seal is necessary to create a seal in between the RD and the driver section every cycle for all desired driver gas pressures. The O-ring seal design proved to be an arduous task and will be explained in Section 4.2.

3.4. Design Conclusion

From the descriptions of the new diaphragmless shock tube design, named the Shock Generator (SG), given is Sections 3.1 through Section 3.3, one can understand how this design will produce shock waves and flow fields similar to those produced by a traditional shock tubes. Additionally, one can understand how the SG design will exhibit several desirable characteristics that are deficient in traditional shock tubes and current repeatable shock tube solutions. Specifically, the SG should exhibit a high degree of repeatability and accuracy to ideal shock tube theory (ISTT), as well as form shock waves in short distances with relatively low-duty-cycles, thus enabling the administration of rapid statistical analyses.

4. SHOCK GENERATOR

4.1. Apparatus Overview

The present Shock Generator design is composed of five sections: the driver, actuation, driven, test, and muffler, as illustrated in Figure 4. The driver, driven, actuation, and test sections all have rectangular cross sections (though a circular driver section could be used). This geometry was chosen as described in Section 3.2 to generate planar shock waves.

The driver section is made from 19.05 mm (3/4") thick 304-stainless steel plate. It has an internal cross section of 15.24 x 66.04 mm (0.6" x 2.6"), height by width, and is constructed from two 184.15 mm (7.25") long sections bolted and sealed together for a total length of 368.3 mm (16.5").

The driven sections and test section are made from 19.05 mm (3/4") thick 6061-T6 aluminum, have an internal cross section of 25.4 x 76.2 mm (1.0" x 3.0"), height by width, and are each 190.5 mm (7.5") long. The driver section, the driven section, and the test section are all made from a C-channel with a welded plate on top to create the rectangular channel. The designed aspect ratio of three inside the driven sections and test section minimizes the three-dimensionality of the flow field as discussed in Section 3.2.

The test section has two 25.4 x 101.6 mm (1.0" x 4.0"), height by length, viewing windows on either side and two 31.75 x 95.25 mm (1.25" x 3.75"), width by length, windows on the top and bottom. All the test section windows are (1/2") thick to prevent the optical glass from fracturing due to the exposer to the maximum expected post shock

wave gas pressure. These windows provide optical access for diagnostic techniques such as shadowgraph, schlieren, or particle image velocimetry. To provide further optical access to the bottom window the entire Shock Generator (SG) is elevated above the optical table by bolting it on top of 152.4 mm (6”) aluminum C-channel, which puts the bottom of the test section at 184.15 mm (7.25”) above the optical table. To secure the SG in place the C-channels are bolted to the optical table. When optical techniques are not necessary, the replacement of the glass windows with either aluminum plugs or G-10 fiberglass composite plugs is possible. The G-10 fiberglass composite plugs provide electrical isolation for instrumentation, more details about the G-10 fiberglass composite plugs are in Section 4.5.

The actuation section is constructed from 6061-T6 aluminum, has a cross section of 107.95 x 91.44 mm (4.25” x 3.6”), height by width, and is 76.2 mm (3”) long. The actuation section is discussed in more detail below in Section 4.2. The muffler is an Allied Witan C.O. Model 60 atomuffler and has four screened barrels, which allows the driver gas to vent into the room at a low velocity to prevent damage to equipment and personnel in the room, and reduce the noise level of the Shock Generator (SG). The atomuffler screws into a mounting flange that is bolted to the end of the last driven section. Each section of the Shock Generator is bolted together using 16 1/4-20 steel bolts along the edges of the flanges. The 16 bolts ensure that the O-ring between each 158.75 mm x 177.8 mm x 19.05 mm (6.25” x 7” x 0.75”), height by width by length, flange is properly compressed to provide the best seal.

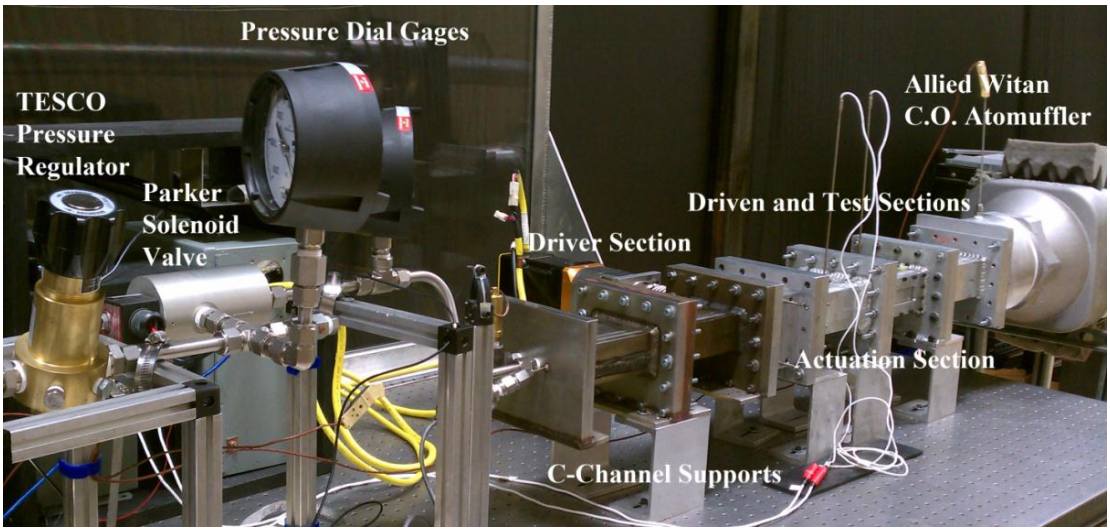

(a) Built Facility

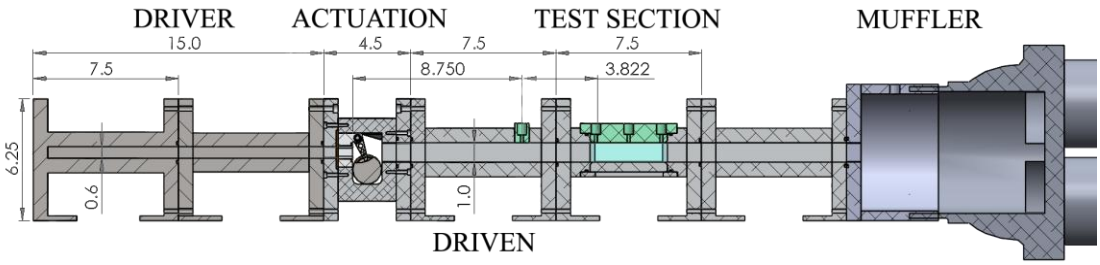

(b) Schematic Representation – Enlarged view is presented in Appendix C (Units: inch)

Figure 4 Shock Generator

4.2. Design and Component Descriptions of the Actuation Section

The actuation section illustrated in Figure 4 contains five components: the rotating door (RD), side-walls, support piece, rotating cam-shaft (RCS), and rubber wedge.

4.2.1. Rotating Door

The rotating door (RD), as seen in Figure 5, is a hinged wedge made from 7075-aluminum. This material was chosen for its high strength, high ductility, and low

density. As discussed in Section 3.3, a lower density material lowers the overall weight and thus lowers the rotational of inertia of the RD, therefore allowing it to open faster and improving the overall performance of the Shock Generator (SG). The original design of the RD used grade 3 titanium. However, due to titanium's low ductility, the RD fractured after a few cycles. Furthermore, titanium also has a higher density and thus higher rotational inertia than aluminum. Therefore, 7075-aluminum is the material of choice for the RD. The RD is 38.6 mm (1.52") tall, 76.2 mm (3") long, and 12.7 mm (0.5") wide at the hinge point and 2.54 mm (0.1") wide at the tip. The through-holes along the length of the RD reduce the weight and thus the rotational inertia of the RD. The through-holes' size and placement maintain the strength and integrity of the RD during operation.

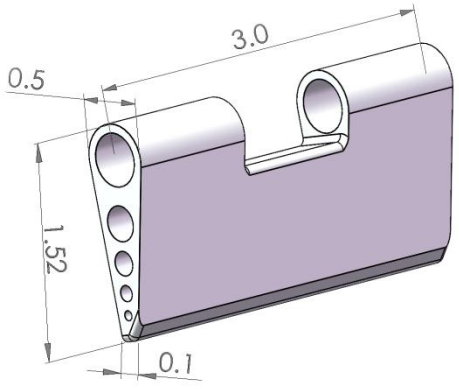

Figure 5 Rotating Door (Units: inch)

The rotating door (RD) is constrained such that it can only rotate 90° along the hinge axis. The hinge axis is constrained at three points, one hinge support in each side-

wall, shown in Figure 6, and the third hinge support in the support piece shown in Figure 7. The hinge pin is made from 4140 steel, and is designed to transmit all of the loads from the RD to the Shock Generator's (SG) structure. The hinge pin is 106.68 mm (4.2") long and 6.35 mm (0.25") in diameter. To ensure that the RD is always well lubricated and free to rotate with as little friction as possible, the hinge pin is surrounded by 1.59 mm (1/16") of brass oilite bearings, which is oil impregnated into brass (Beemer Precision, Inc.).

4.2.2. Side-Walls

The two side-walls support the RD's hinge pin as well as the RCS. Both side-walls are made from 6061-T6 aluminum attach and are attached to the actuation section using two 38.1 mm (1.5") long by 6.35 mm (1/4") diameter steel alignment pins and four 1/4-28 steel bolts. Each side-wall is 107.95 mm (4.25") tall, 19.05 mm (0.75") wide, and 76.2 mm (3") long. These side-walls were designed to be removable in order to gain access to the interior components of the actuation section and the flow path.

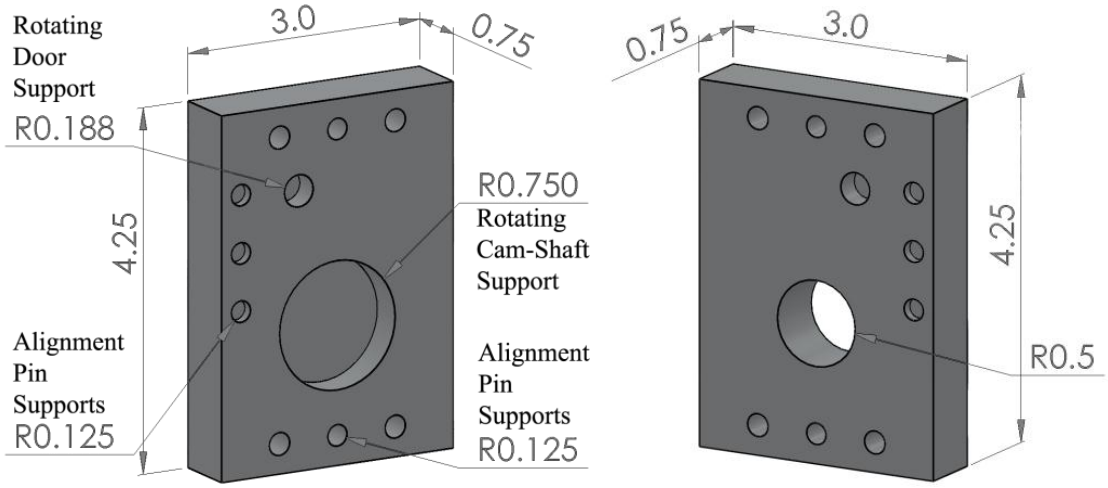

(a) Left Side-Wall **(b) Right Side-Wall**

Figure 6 Side-Walls (Units: inch)

4.2.3. Support Piece

The support piece, as illustrated in Figure 7, is made from 7075-aluminum and contains the center support for the RD, as well as, the O-ring dovetail groove that in conjunction with the RD seals the driver section's 6th face. The support piece is 44.32 mm (1.745") tall, 82.42 mm (3.245") wide, and 25.4 mm (1.0") long. It is kept in place using four 6.35 mm (1/4") long by 6.35 mm (1/4") diameter steel alignment pins that go through the sides of the actuation sections and into the side-walls. To prevent leaks around the support piece when the RD is closed the back of the support piece is pressed against a rubber gasket that pressed against the actuation section flange. Additionally, RTV silicon fills in any remaining gaps. The radius along the top provides extra support for the RD as it rotates to reduce the deflection of the hinge pin. The flow path of the support piece has a cross section of 17.17 x 67.89 mm (0.676" x 2.673"), height by

width, with edge fillets of 3.175 mm (0.125”) radius. The fillets inside the flow path add support to the groove because the distance between the groove and the flow path is 0.328 mm (0.0129”). The groove geometry is essential in order to keep the O-ring in place as the RD quickly opens and releases the driver gas. The groove is 2.1 mm (0.0827”) deep, 2.18 mm (0.0858”) at the throat and 3.51 mm (0.138”) at the base, with a 66° slope angle from the base to the throat, as illustrated by Figure 7c.

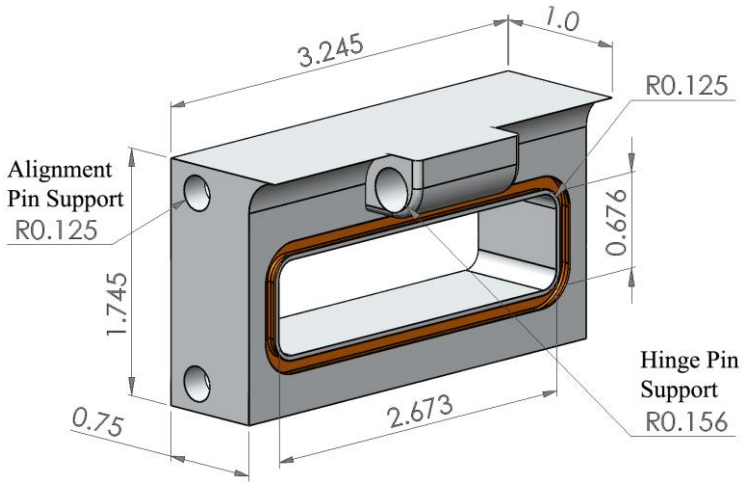

(a) Profile View

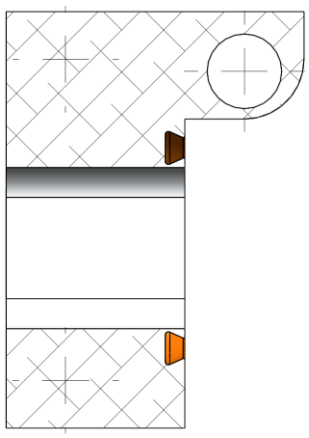

(b) Cross Section View

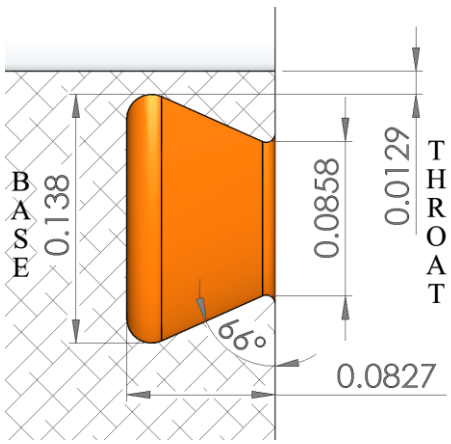

(c) Groove Profile

Figure 7 Support Insert Piece (Units: inch)

The primary obstacle in the design and implementation of the rotating door and locking cam-shaft valve (RDLCV) was preventing the O-ring from being dislodged from its groove and carried downstream by the fast-moving, high-pressure driver gas. The current design is a product of many design iterations. Previous designs implemented different O-ring groove geometries, different sized and shaped O-rings, and different glues and lubricants to attach and / or seal the O-ring inside its groove. These previous designs failed primarily due to the high-pressure driver gas permeating into the O-ring groove and pushing the O-ring out during the opening of the RD. Sometimes the O-ring was pushed out only slightly, in which case the RD pushed the O-ring back into place during the next cycle. However, other times the O-ring was pushed far out of place, which caused the O-ring to be torn as the rotating cam-shaft (RCS) closes the RD, thus breaking the seal. Occasionally the O-ring was completely ejected from the O-ring groove during operation. The last two cases only occurred when the O-ring or the mechanism for holding it in the O-ring groove has fatigued resulting in the failure. Regardless of how the seal fails, replacement of the O-ring results in longer down time.

Every tested seal design has a fatigue life. The fatigue life is the number of cycles completed before the seal fails. The fatigue life has been attributed to two factors. First, the repeated compression and expansion of the O-ring eventually causes it to fracture. Second, and the most common, is the driver gas pressure permeates into the groove forcing the O-ring further and further out of its O-ring groove with each successive cycle, until the RD tears the O-ring. Moreover, the fatigue life tends to decrease with increasing driver gas pressure.

The current O-ring of choice is a Buna-N AS568A-137 O-ring with a durometer[2] of 90A. This O-ring is a standard size and made from Buna-N; thus, it is inexpensive. Furthermore, a durometer of 90A ensures a good seal every cycle, resulting in a wider range of achievable driver gas pressures because more force is needed to compress a high durometer O-ring than a low durometer O-ring. Therefore, with a high-required compression force the O-ring is more likely to stay inside the O-ring groove during operation. Additionally, with a high durometer O-ring, greater force is applied onto the RD when the RD is closed. Thus, the O-ring acts like a spring, pushing the RD open as the O-ring returns to its native state, resulting in faster opening times. Previously tested O-rings included those made from Alfas and Buna-N with durometers from 50-90A. In addition, PTFE O-rings were tested, which have a durometer of 55D and is the hardest durometer available, but fractured from the force necessary to install the O-ring into the dovetail groove. Therefore, PTFE O-rings were an unsuitable solution.

Ultimately, the seal design that provides the best performance, and is used for the remainder of this study, uses the combination a Buna-N AS568A-137 O-ring with a durometer of 90A surrounded by PolySi Technologies silicone O-ring Lubricant number 841 (PST-841) and placed inside the dovetail groove mentioned above. The PST-841 allows for easy installation of the O-ring and fills in any gaps in the dovetail groove not

[2] Albert F. Shore developed a hardness measurement device in the 1920s. The term durometer can be referred to the measurement of hardness or the device itself. The durometer of a material is generally used as a measurement of hardness in polymers, elastomers, and rubbers [17].

filled by the O-ring. The PST-841 also prevents the driver gas from permeating into the O-ring groove and ejecting the O-ring out during operation.

Four important design criteria that were necessary in designing the current O-ring and dovetail groove seal are the following:

1. The O-ring diameter should be as large as possible.
2. The length of the dovetail groove track needs to be the same length as the O-ring used.
3. The O-ring is not stretched or compressed into the groove.
4. The minimum track radius of the O-ring groove must be at least three O-ring diameters.

The current seal design also provides no apparent fatigue life because the seal lasted for every cycle at every tested driver gas pressures, thus providing an upper operation limit for the SG above 500 psig driver gas pressure. Thus, the upper operational limit was not documented SG because the highest tested driver gas pressure was 500 psig.

4.2.4. Rotating Cam-Shaft

The rotating cam-shaft (RCS) illustrated in Figure 8 serves two purposes. The first purpose is to apply and maintain a uniform force with the RCS's uncut section along the bottom of the rotating door (RD) thus sealing driver section while the RD is closed. The second purpose of the RCS is to allow the RD to rotate freely when the RCS's cutout section lines up with the bottom of the RD. Therefore, in order to

accomplish both purposes, the RCS and RD must remain parallel to each other and be kept in place throughout the operation. Therefore, the tolerances between all the following pieces were designed to tolerances less than 0.0635 mm (0.0025”):

- RCS and oilite bearings (Beemer Precision, Inc.)
- Oilite bearings and RCS’s side-wall support
- RD and oilite bearings
- RD’s hinge pin and oilite bearings
- Oilite bearings and RD’s side-wall support
- Alignment between both side-wall supports of all alignment holes and support holes

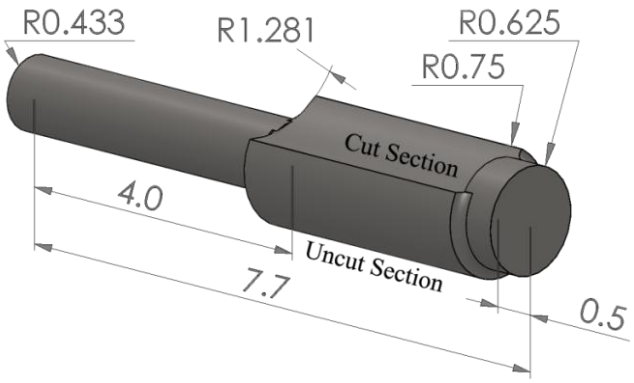

Figure 8 Rotating Cam-Shaft (Units: inch)

The rotating cam-shaft (RCS) is made from 304-stainless steel and is 195.58 mm (7.7”) long and 38.1 mm (1.5”) in diameter. The cam-shaft is supported on both ends by

the two side-walls to minimize deflections from the force of RD onto the RCS. The cam-shaft is tapered down to 31.75 mm (1.25”) in diameter on one side in order to fit into the left side-wall RCS support and is tapered down to 21.99 mm (0.866”) in diameter on the other side in order to fit into the right side-wall RCS support. The two tapered ends of the RCS are surrounded with 3.175 mm (1/8”) brass oilite for lubrication (Beemer Precision, Inc.).

The RCS is then coupled a shaft bearing through the 21.99 mm (0.866”) in diameter tapered end. The shaft bearing is then coupled to a Parker BE 342HQ series servomotor through a Parker PS90 50:1 ratio gearbox, as illustrated in Figure 9. The servomotor is a feedback-controlled, very low position error (four hundred thousand encoder counts), high rotational speed (4500 RPM), and low output torque device (76 lb.-in). The servomotor’s output shaft is permanently connected to a gearbox that converts the high speed, low torque rotation of the servomotor to the high torque, low speed rotation of the cam-shaft. The motor-gearbox system is capable of producing up to 1,000 in-lbs. of torque in order to overcome the loads exerted by the RD on to the RCS, up to 2,000 psig driver gas pressure. Additionally, a Parker Aries motor controller is used to control the servomotor because it offers the ability to send commands to and receive feedback from the servomotor. Moreover, the Aries motor controller allows for the programming of any motion profile into the servomotor. An in-house Labview (Nation Instruments Corp.) and the Parker ACR program that comes with the Aries unit control the Aries motor controller. Further explanation on the in-house Labview program (Nation Instruments Corp.) is in Section 5.2.

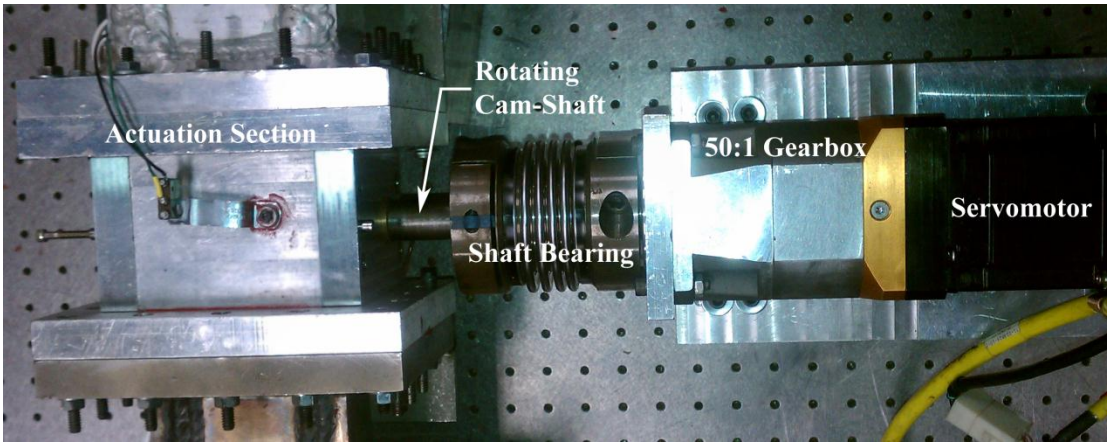

Figure 9 Rotating Cam-Shaft and Servomotor Assembly

4.2.5. Rubber Wedge

The rubber wedge cushions the impact of the rotating door (RD) in order to increase the lifespan of the RD. The rubber wedge is 6.675 mm (0.263") tall, 82.55 mm (3.25") long, 25.4 mm (1") wide at the base and comes down to a point at the tip. Additionally, the rubber wedge has a wedge angle of 16.26°, which ensures that front surface of the RD hits flush against the rubber wedge. Therefore, this wedge angle enables the RD to evenly transfer its momentum to the rubber wedge thereby reducing the stress on the RD as it stops in the open position. Moreover, as mentioned in Section 3.2, this wedge angle allows the RD to create a continuous and smooth flow path from the driver section to the driven section when the RD is fully opened as illustrated in Figure 10e. The rubber wedge is secured to the ceiling of the actuation section by two #8 steel bolts that come through the top of the actuation section and thread into a metal

plate that is glued to the rubber wedge using Loctite 5 minute epoxy. To prevent leaks, RTV silicone is used in between the metal plate and the ceiling of the actuation section.

4.3. Actuation Cycle Process

The actuation of the rotating door (RD) is controlled by the rotation of the rotating cam-shaft (RCS) and the driver gas pressure on the back face of the RD. Each step of the cycle is illustrated in Figure 10. Each cycle begins with the in-house Labview program (Nation Instruments Corp.) commanding one 360° rotation of the Parker servomotor. After the servomotor and RCS have rotated for 2 seconds, the RCS will have closed the RD to seal the driver section (Figure 10a). After the 2 seconds, the in-house Labview program (Nation Instruments Corp.) opens the Parker EH50 solenoid valve until the Omega PX-303 (0 to 3000 psig) pressure transducer in the driver section reads 95% of the desired driver gas pressure, which usually occurs at 3/4 the rotation (Figure 10b). At this point, the in-house Labview program (Nation Instruments Corp.) waits one second before closing the Parker solenoid valve. However, due to delays in the system, by the time the solenoid valve is closed the driver section will be filled to regulated pressure. Once the servomotor has completed approximately 99% of the rotation, the RCS's cutout section will line up with the bottom of the RD to allow it to open freely by the force applied by driver gas (Figure 10d). As the driver gas pressure is released, the RD opens in the sequence illustrated in Figure 10d to Figure 10f. Once the RD has opened, the servomotor has stopped to allow the RD to fall back down via gravity (Figure 10f). This cycle repeats itself every six seconds.

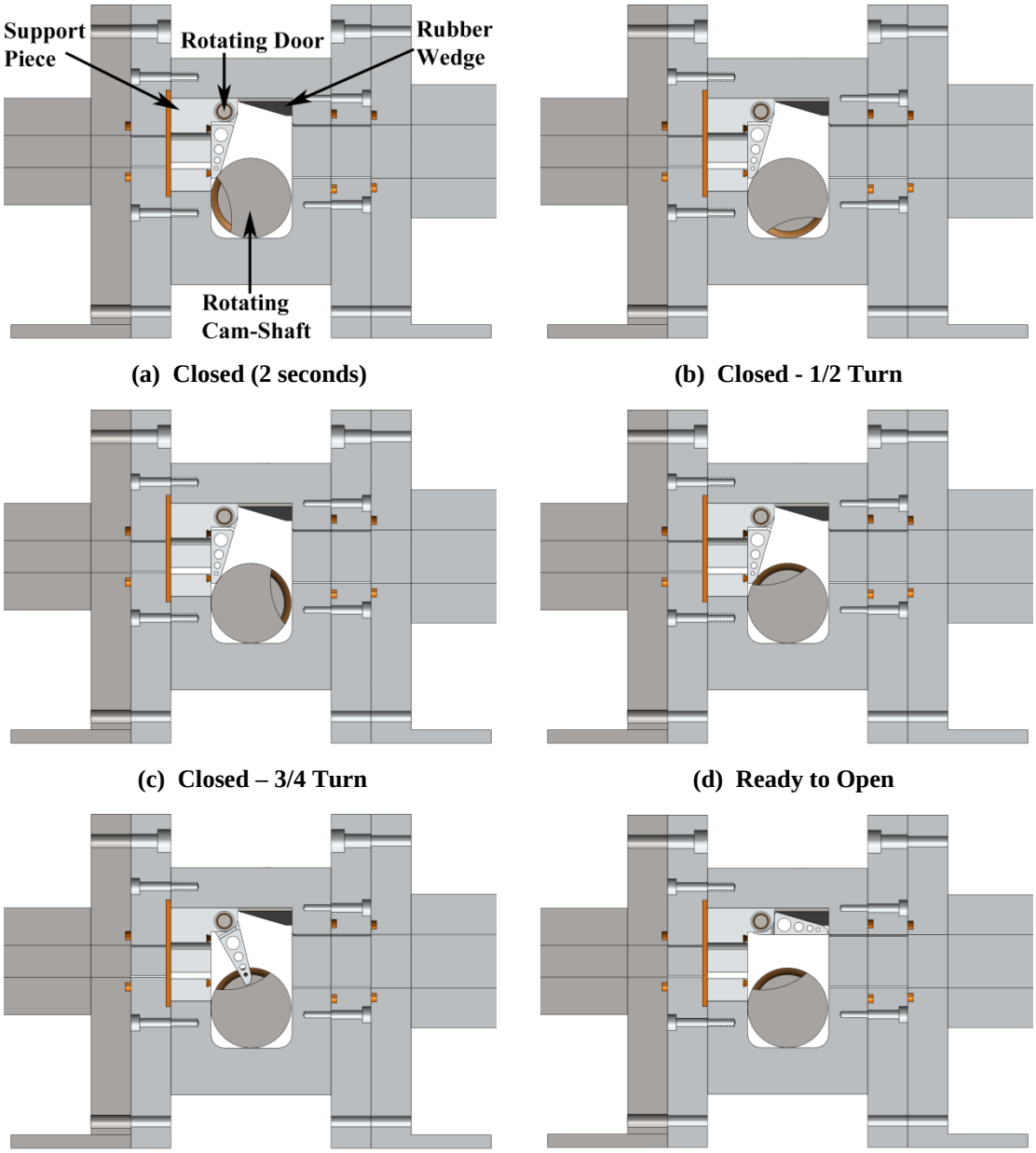

(a) Closed (2 seconds)

(b) Closed - 1/2 Turn

(c) Closed – 3/4 Turn

(d) Ready to Open

(e) Free Swinging

(f) Open Position

Figure 10 Actuation Device

4.4. Air Supply System

4.4.1. Flow Path

The Shock Generator uses compressed air as the driver gas and ambient air as the driven gas. The compressed air for the driver section originates from a manifold of two compressed air cylinders (CACs) attached to the wall illustrated in Figure 11. Each CAC arrives containing pressurized air between 2200 and 2500 psig. After the opening the valve on top of each CAC, the air flows through a 1/2” pipe check valve, which prevents the CACs from filling each other, which would be unsafe. Afterward, the air flows through a 1/2” pipe into a 1/2” pipe cross. The 1/2” pipe is converted to a 1/2” stainless steel compression fitting tube (CFT) because CFT is much easier to work with than pipe. The air then flows through a 90° bend inside 1/2” braided flexible CFT.

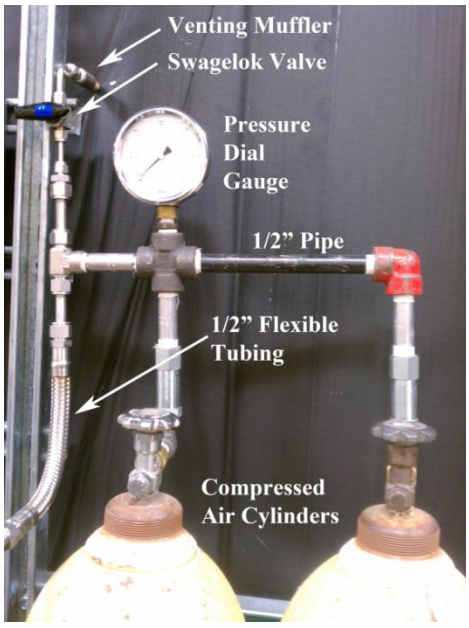

Figure 11 Upstream Air Supply System

From the 1/2” braided flexible CFT, the air travels through eight feet of CFT until it reaches the Tescom 44-1317 high-pressure regulator, shown in Figure 12 and is used to control the driver gas pressure. Next, as depicted in Figure 12, the regulated compressed air flows to a Parker EH50 solenoid value controlled by the previously mentioned in-house Labview program (Nation Instruments Corp.). When the in-house Labview program (Nation Instruments Corp.) opens the solenoid valve, the regulated compressed air flows into the driver section, filing it to the regulated gas pressure**.**

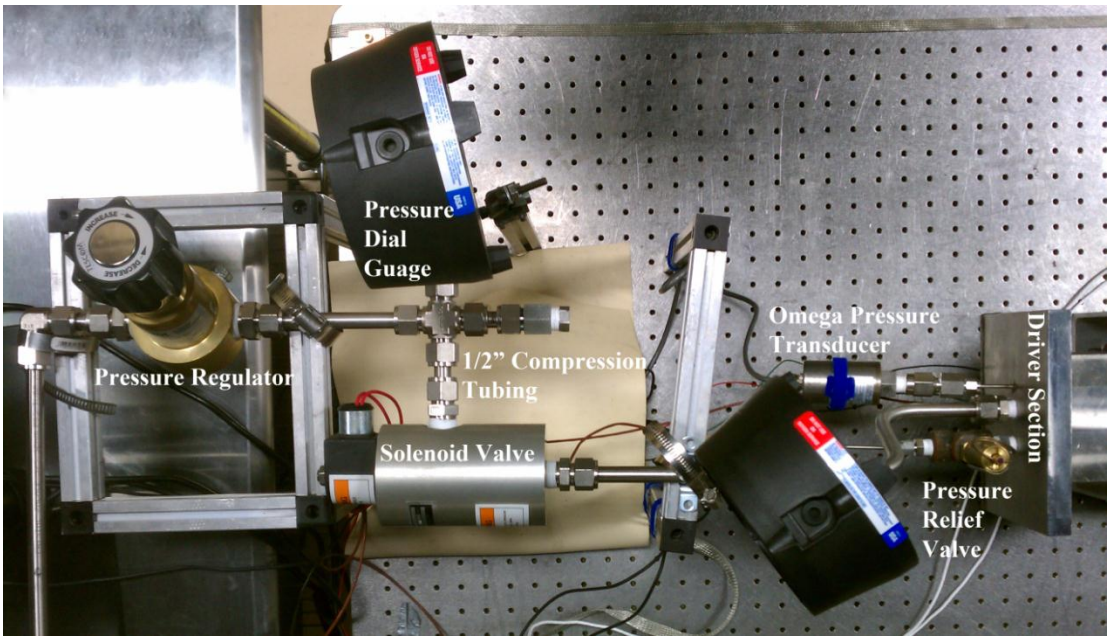

Figure 12 Downstream Air Supply System

4.4.2. Safety Precautions

Many precautions were taken throughout the air supply system in order to maximize the safety associated with this high-pressure system. First, every component in the air supply system is factory rated to either 2500 or 3000 psig. The exception is the driver section, which, as mentioned in Section 4.2, was hydrostatically tested at 3000 psig. Second, 0 to 3000 psig pressure dial gauges were placed throughout the air supply system as illustrated by Figure 11 and Figure 12. These pressure dial gauges were placed in between the

- Compressed air cylinders and pressure regulator
- Pressure regulator and solenoid valve
- Solenoid valve and driver section

The pressure dial gauges act as a safety check that ensures only the desired gas pressure is in each segment of the air supply system at the desired time. Third, a 1500 psig pressure relief valve in the back flange of the driver section ensures that the driver section and the rotating door never reach the possible 2500 psig gas pressure inside the CACs. Fourth, when the Shock Generator is not operational the air supply system is vented into the room through a Swagelok valve that then flows into a muffler, illustrated in Figure 11.

Furthermore, the extensive use of stainless steel compression fitting tube (CFT) throughout the air supply system instead of pipe is due its many advantages over pipe. CFT is easy to cut to length, assemble, and rearrange. CFT does not need Teflon tape to seal and can be bent to any desired angle.

For safety, no component is free to move off the optical table. Furthermore, all components have been designed to withstand 1.5 times the maximum exposure pressure, except for the door which was only designed to withstand the 1.25 times the maximum exposure pressure. Furthermore, the individual driver sections, driven sections, and test section were hydrostatically pressure tested at the designed condition, which was 1.5 times exposure pressure. Therefore, the driver sections were hydrostatically pressure tested at 2500 psig; the driven sections and test section were hydrostatically pressure tested at 200 psig.

4.5. Electrical System and Noise Reduction

The basic wiring diagram for the Shock Generator's electrical system is illustrated in Figure 13. From Figure 13, one can see how all of the components are grounded together (green wires). However, one may not realize the importance of proper grounding for eliminating Electro Magnetic Interference (EMI) or noise from a system. EMI in a system can cause bias and / or random error in measurements. The amount of error induced into a measurement by EMI is dependent upon the level of EMI in the system. If the level of EMI is lower than instrument's accuracy then the measurements obtained will be as accurate as the instrument used to obtain it. However, if the EMI is higher than the instrument's accuracy then the EMI will induce error into the measurements.

In the Shock Generator (SG), there were two main sources of EMI or noise, the solenoid valve's power supply and the servomotor. This EMI permeated into the

measurements of the driver gas pressure and the driven gas pressure. Therefore, a great deal of care was taken to eliminate the EMI from these measurements.

The Parker servomotor and Aries controller were put onto their own power grid, 210V and 120V, respectively. As directed by the installation manual, the Parker servomotor and Aries controller were grounded together through the shielding of both the power cable and the feedback and control cable.

The solenoid valve's power supply was grounded to the Endevco DC amplifier (the driven gas pressure transducer's power supply and signal filter), and the computer chassis. To ensure the best grounding, AlphaWire copper grounding cable was used along with 1/8" thick copper plate and 1/4-20 brass fittings. Therefore, by grounding these components in this manner the resistance between the components is lowered, which equalizes the voltage potential between all the components, reducing the EMI.[3] Furthermore, a common ground for the entire system was established by grounding these components to the stainless steel top of the optics table and then grounding them to the electrical ground of the instrumentation surge protector. The grounding setup just described, reduces the EMI below the measurement level of the driver gas pressure transducers, however, it does not lower the EMI below the measurement level of the driven gas pressure transducers (DnT). Therefore, in order to remove the EMI from the DnT, four additional steps were taken.

[3] As a note, using unlike metals in the grounding connections induces a voltage potential, thus induces noise in the system.

First, the DnT' power supply, the Endevco DC amplifier, was removed from the instrumentation surge protector and plugged directly into an electrical outlet because surge protectors cause ground loops, which induces low level EMI into the system. Although the EMI caused by the surge protector was small, it was still large enough to be measured with the DnT.

Second, the DnT is electrically isolated from the Shock Generator (SG). This was accomplished by using G-10 fiberglass composite, which offers an excelent balance between strength, level of electrical isolation, and ease in machinability.

The reasoning for electrically isolating the DnT is because EMI travels through electrical pathways; therefore, electrically isolating the measurement equipment should eliminate the EMI. The EMI would also be eliminated if the sources of the EMI were electrically isolated; however, this option was not feasible for our system.

Third, the DnT measurements were low-pass filtered using the Endevco DC amplifier - model 136, which serves as the DnT' power supply, signal amplifier, and signal filter. The filter used in the Endevco DC amplifier - model 136 is a 10 kHz 4-pole Butterworth lowpass filter. Although 125 kHz would have been optimal to satisfy nyquist, which would be half the sampling frequency, the 10 kHz filter was built into the Endevco unit and could only be turned on or off.

Fourth, the driver gas pressure transducer and the solenoid valve relay control cable had to be removed from the DnT data acquisition unit and placed on its own data acquisition unit. The USB data acquisition unit offered the additional benefit of electrically isolating these signal.

After using all of the EMI reduction techniques described above the driver gas pressure transducer and the driven gas pressure transducers have a mean error of 2.25% and 0.085% respectively. This error was calculated by obtaining the percent standard deviation, which will be explained in Section 5.3.2.

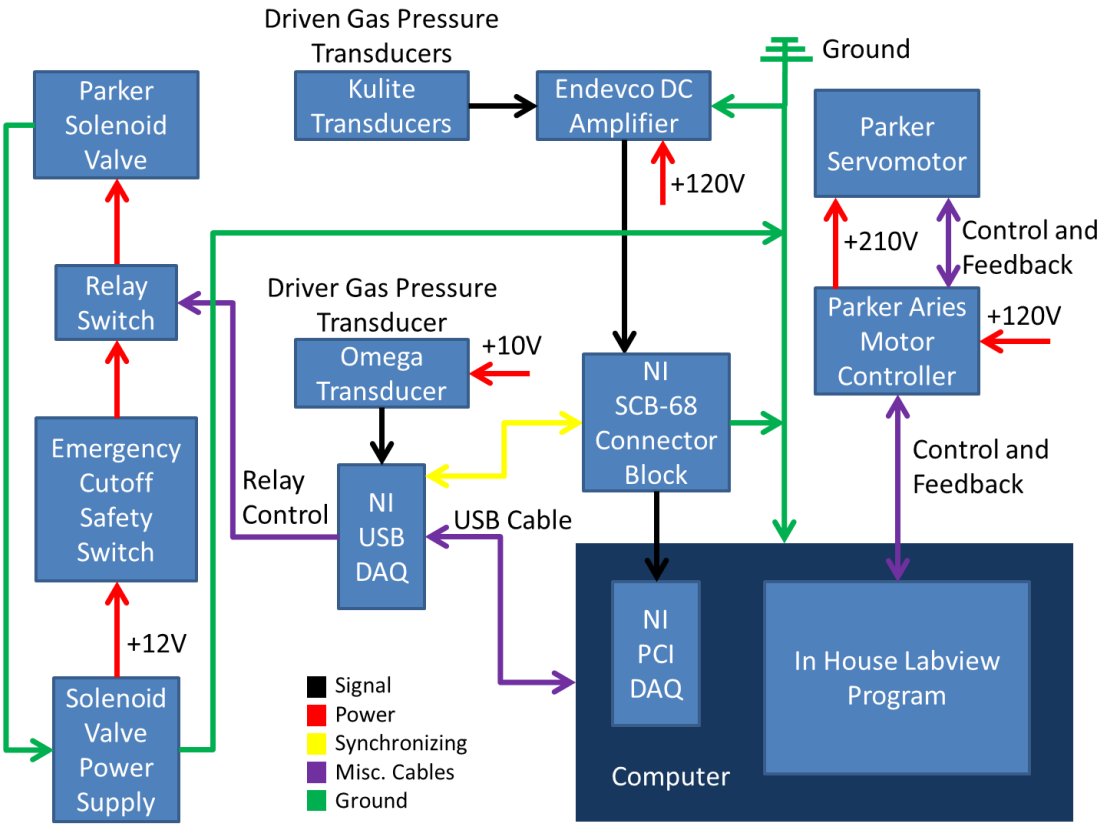

Figure 13 Wiring Diagram

From Figure 13, one can see how the Parker EH50 Solenoid valve is cycled open and closed by the in-house Labview program (Nation Instruments Corp.) mentioned in

Section 4.2. The in-house Labview program (Nation Instruments Corp.) sends a 5 VDC output from a National Instruments USB-6211 data acquisition unit that switches a relay switch, which is connected to the Parker EH50 solenoid valve. The power necessary to cycle valve comes from a 120 VAC to 12 VDC power inverter, previously been called the solenoid power supply. Moreover, if the 5 VDC is severed from the relay switch then the relay switch will sever the 12 VDC power to the solenoid valve. Because the solenoid valve is nominally closed, when the power is removed the solenoid valve, the solenoid valve closes. Therefore, for safety, the solenoid valve's power goes through an emergency cutoff switch before it passes through the relay switch. The emergency cutoff switch enables prompt solenoid valve shut off if the driver section O-ring seal fails and adds an extra layer of safety during maintenance on the Shock Generator (SG).

The driver gas pressure transducer has an excitation voltage of 9-30 VDC and is connected to a standard 120 VAC to 12 VDC power inverter, however, because sensitive measurement equipment like transducers are calibrated based on a given input voltage, if that input voltage fluctuates then the calibration is incorrect resulting in incorrect measurements. Therefore, a 10 VDC voltage regulator was installed in between the 12 VDC power supply the driver gas pressure transducer.

5. INSTRUMENTATION AND DATA ACQUISITION

5.1. Experimental Setup

The primary goal of the characterization and feasibility study of the Shock Generator (SG) was to determine if a shock wave has formed inside the test section. If a shock wave did form, then how close is the shock wave speed to ideal shock tube theory (ISTT), how repeatable is the shock wave, how quickly did the shock wave form, and what range of shock wave Mach numbers (M_s) can be produced. Therefore, in order to accomplish these goals, information about the flow as it passes from the driver section through the test section must be collected. Three pressure transducers and two thermocouples are used to collect this information.

5.1.1. Pressure Transducers

For every experiment reported in this study, compressed air is used as the driver gas and ambient air is used as the driven gas. The driver gas pressure is recorded during each cycle with an Omega PX-303 (0 to 3000 psig) pressure transducer (OPT) that outputs a signal from 0-5.5 VDC, with ±0.25% full scale accuracy. The signal is sampled at 250 kHz by a National Instruments (NI) USB-6211 data acquisition unit as a 16-bit, differential, analog signal. As Figure 14 illustrates, the OPT measures the driver gas pressure through a pressure snubber and a 1/8” diameter steel tube that is welded to the back flange of the driver section. Both of which prevent the rapid filling and venting of the driver section from damaging the OPT. They prevent damage to the OPT by acting like a pressure low-pass filter. Therefore, fast high-pressure fluctuations cannot

damage the measurement membrane inside the OPT. As a result, the OPT is not expected to capture or resolve frequencies above 1 kHz. Therefore, the reason behind OPT sampling at a frequency that is much faster than it can resolve will be clarified below.

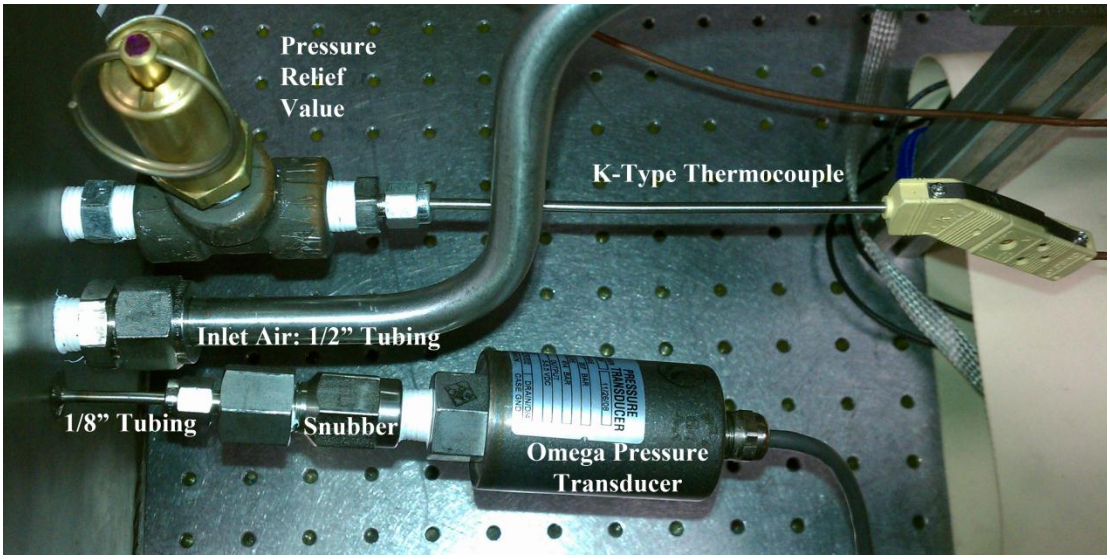

Figure 14 Driver Inlet Flange

The driven gas pressure is measured using two Kulite XTEH-10L high-frequency-response pressure transducers (KPT) that are also sampled at 250 kHz by a NI PCI-6259 data acquisition unit as 16-bit, differential, analog signals. These KPT have a pressure range of 0 to 200 psia, with ±0.1% typical full scale accuracy, and resonance frequencies of 500 kHz. The KPT were chosen because they have fast-response times and short rise times. The KPT's are powered by an Endevco Model 136 DC amplifier

that also amplifies the KPT' signals from nominally 0.1-1 VDC to 1-10 VDC such that the NI PCI-6259 data acquisition unit can read the signals at the maximum resolution.

Both of the NI PCI-6259 and USB-6211 units are controlled by the in-house Labview program (Nation Instruments Corp.) mentioned in Section 4.2. Refer to Section 5.2 for a detailed description of the in-house Labview program (Nation Instruments Corp.). Additionally, these two data acquisition units (DAQs) are synchronized together such that the measured pressure profiles, from the OPT and KPT, have the same starting time and share the same sampling clock. The drawback to synchronizing the two DAQs is that they must have the same sampling rate. Therefore, because the OPT resolve frequencies higher than 1 kHz due to the pressure lowpass filter, sampling faster than the resolvable frequencies is unnecessary for capturing the desired driver gas pressure information. However, even though the KPT cannot resolve frequencies higher than 10 kHz due to the 4-pole Butterworth lowpass filter, sampling faster than the resolvable frequencies is necessary because capturing as many data points along the rising slope of the test section traversing pressure wave is desired for the analysis required in order to conduct the characterization study.

Figure 15 illustrates that even through the OPT and KPT are sampled at a rate higher than they can resolve, they can still capture the lower frequency information. However, the frequency content is not as important as the number of data points along the changing driven gas pressure profile (DPP), which will be explained in further detail in the pressure rise analysis in Section 5.3.1.

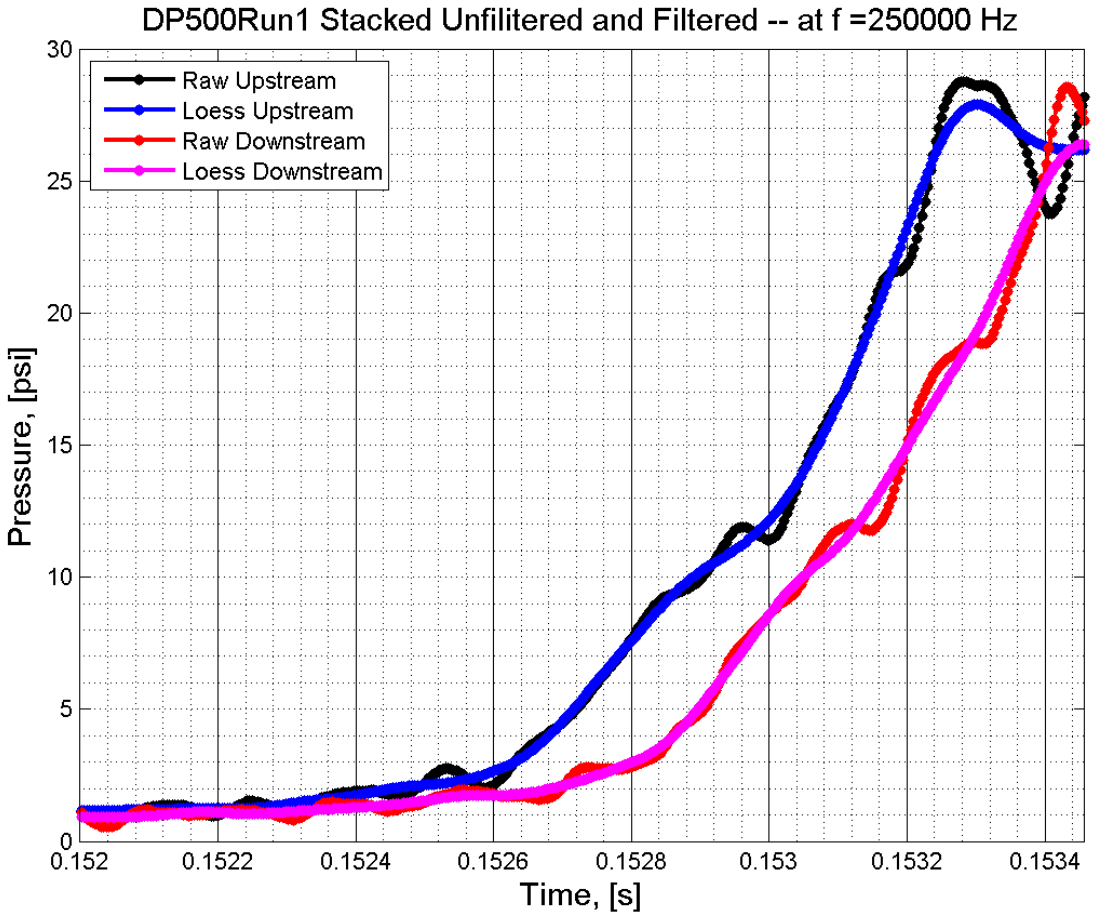

Figure 15 500 psig Stacked Unfiltered and Filtered Transducers

For every experiment, the driven gas pressure transducers (DnT or KPT) remained in the same location. The KPT are separated by a distance of 97.08 mm (3.822") and are 22.1 mm (8.7") from the driver section or the back face of the closed rotating door. In Figure 16, one can observe the KPT inside the instrumentation plugs made from the electrically isolating G-10 fiberglass composite material mentioned in Section 4.5.

The two remaining unused holes in the G-10 instrumentation plug, to the right in Figure 16, enable flexability in determining the shock wave Mach number and shock wave formation distance. This flexibility enables the best measurements to be obtained because the KPT can be moved to any configureation of the four holes. In the current configuration, the KPT are separated by a distance of 97.08 mm (3.822”), which was determined to provide accurate values for the shock wave Mach number, while minimizing potential shock wave degradation due to viscous losses, bases on moving the KPT to a few locations. However, a study of the optimal configuration of KPT was not conducted. Additionally, all three holes of the test section instrumentation plug are separated by 42.92 mm (1.69”), and any of the four holes are plugged with #10-32 bolts when not in use to prevent leaks.

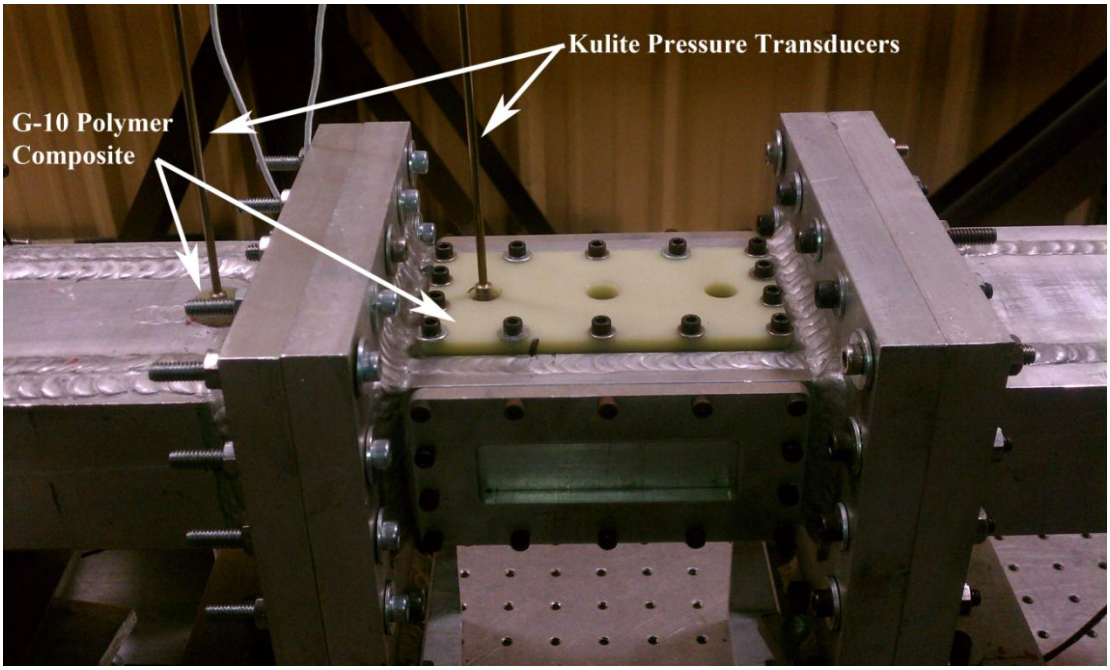

Figure 16 Test Section

5.1.2. Thermocouples

The two thermocouple used in this experiment are placed in the driver section (illustrated in Figure 14) and in the muffler. As seen in Figure 14, the driver thermocouple is located off the centerline; however, the tip of the thermocouple is located in the center of the driver section. The tip of the muffler thermocouple is located along the centerline of the Shock Generator and in the center of the flow as illustrated in Figure 17. Although the muffler thermocouple is in an expansion region of the flow, the recorded thermocouple temperature is at the steady state condition in between runs. Therefore, each thermocouple can be used to approximate the speed of sound in the region they are located in.

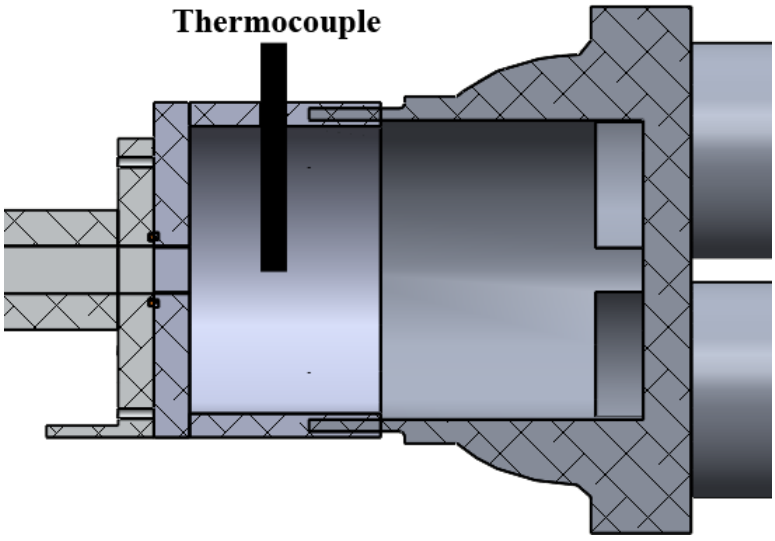

Figure 17 Muffler Thermocouple

The approximate speed of sound is then used to obtain the shock wave Mach number. Therfore, it is assumed that the thermocouple in the muffler will provide the most accurate speed of sound estimate for the shock waves traveling through the driven sections and test section while the thermocouple in the driver should provide the best estimate for the speed of sound of the upstream moving espansion fans.

5.1.3. Servomotor Odometry and Rotating Door Open Switch

Additionally, in order to attempt to find out when the RD opens the servomotors, odometry is obtained from the Aries controller using the in-house Labview program (Nation Instruments Corp.) and a limit switch is placed behind the rubber wedge such that when the RD hits the rubber wedge the rubber wedge will compress and trigger the limit switch. The limit switch closes a circuit between a 9 Volt battery and the NI PCI-6259 DAQ, which read the signal as another 16-bit, differential, analog signal, just like KPT and OPT signals.

5.1.4. National Instrument Data Acquisition Units

Two National Instrument data acquisition units USB-6211 and PCI-6259 are used. The National Instrument data acquisition units are synchronized together by connecting their Sample Clock and Start Trigger Inputs/Outputs respectively together. Then, using the in-house Labview program (Nation Instruments Corp.) to properly configure the DAQs the timing information is shared between the two DAQs. Furthermore, all pressure data is acquired as 16-bit, differential, analog inputs. Moreover, all of the inputs on the NI PCI-6259 unit, which acquires the KPT signals, are

separated by one input channel in order to reduce cross talk between channels. The NI PCI-6259 manual states that the cross talk of two adjacent channels is -75 dB while the cross talk between non-adjacent channels is -95 dB.

Furthermore, because, both DAQs are synchronized together, the fastest sampling rate obtainable is limited by the slowest DAQ. The maximum sampling rate of the NI USB-6211 DAQ is 250 kHz for a single channel. Additionally, the maximum sampling rate of NI PCI-6259 DAQ is 1.25 MHz for a single channel. However, like the NI USB-6211 DAQ, the NI PCI-6259 DAQ has an on board multiplexer. Therefore, the more channels read by the DAQ the lower the maximum sampling rate becomes. The general rule for the maximum sampling rate is as follows

$$\text{Maximum Obtainable Sampling Rate} = \frac{\text{Maximum Single Channel Sampling Rate}}{\text{Number of Sampled Channels} + 1} \qquad (5.1)$$

In the present setup, the NI PCI-6259 DAQ scans the two driven gas pressure transducers (DnT or KPT) and the RD's open switch. Therefore, the maximum obtainable sampling rate in the NI PCI-6259 is $\frac{1250\ \text{kHz}}{3+1} = 312.5\ \text{kHz}$. As a result, the NI USB-6211 DAQ is the slowest DAQ. Therefore, for all experiments, a sampling rate of 250 kHz was used.

5.1.5. Pressure Transducer Calibration

The calibration of each pressure transducer is obtained by recording the voltage output from the pressure transducer at a known pressure. For precise calibrations, the pressure transducers are kept in the electrical configuration, described in Section 4.5. Additionally, the pressure transducers are read through the same in-house Labview

program that records the data. This process ensures that all potential errors throughout the system are accommodated inside the calibration, thus providing the most accurate possible calibration.

Furthermore, the “known” pressure is “known” by measuring it using a Grade 3 mirror backed test dial gauge from Omega Engineering with 0.25% accuracy. The calibration is completed by obtaining eight to ten data points of voltage output versus gas pressure. These eight to ten data points are distributed over the full range of pressures that each pressure transducer is expected to experience during the all testing conditions.

With these eight to ten data points, Microsoft Excel is used to create a voltage versus pressure plot. A linear trend line is then obtained for each pressure transducer calibration curve. This trend line is entered into National Instruments Measurement & Automation Explorer, which enables the use of voltage to pressure conversion profiles. From Figure 18, one can see that all three pressure transducers perform as designed with linear pressure responses. Moreover, one can see that the OPT, labeled as “Driver T”, has a much greater slope than either of the KPT, which are labeled as upstream driven transducer (UDT) and downstream driven transducer (DDT). This difference in slope is a result of the type of transducer and the pressure range of the transducer. Remember the OPT is a 0 to 3000 psig slow-response pressure transducer, while the KPT are a 0 to 200 psia fast-response pressure transducer.

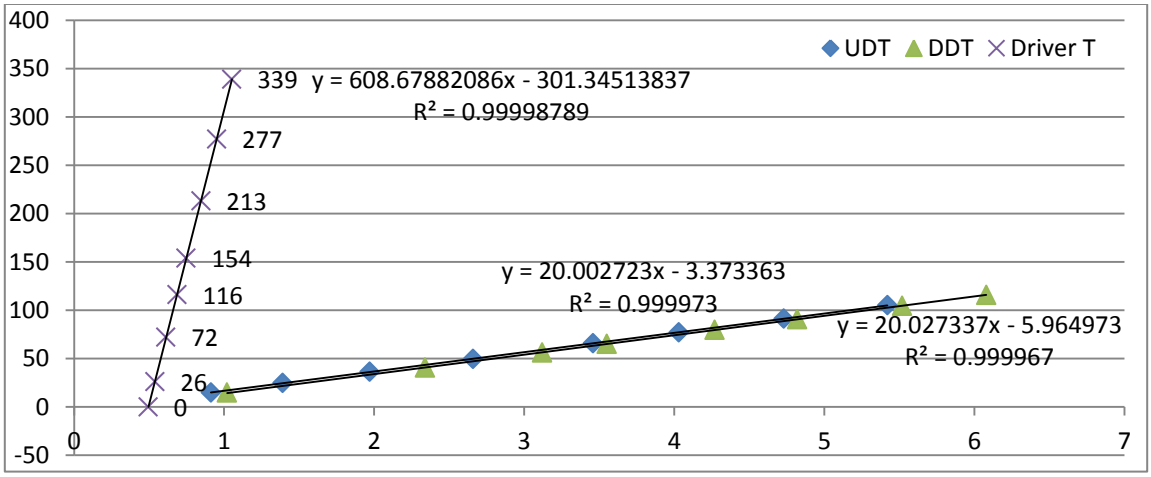

Figure 18 Calibration Plot

5.2. Servomotor Control and Data Acquisition Program

As mentioned in the previous sections, the in-house Labview program (LP) controls the entire system (Nation Instruments Corp.). The LP controls the Parker BE 342HQ series servomotor and the Parker EH50 solenoid valve as well as acquires pressure transducer, thermocouple, servomotor odometry, and RD open switch information. Furthermore, the LP is broken up into two segments, the front panel and the back panel.

5.2.1. Front Panel

Figure 19 illustrates the front panel, which contains the initialization and input parameters, cycle process indicators, and real-time pressure analysis tools.

5.2.1.1. Initialization and Input Parameters

Prior to running the LP, all initialization parameters must be set on the front panel. These parameters include the desired driver gas pressure, sampling rate, and update rate. Therefore, prior to testing each driver gas pressure region, the initialization parameters must be set. For all experiments conducted, only the desired driver gas pressure initialization parameter was changed between tested driver gas pressure regions.

The desired driver gas pressure serves three purposed. First, the desired driver gas pressure names the output files. Second, the desired driver gas pressure determines when to start recording data. Third, the desired driver gas pressure determines when to open the solenoid valve.

The sampling rate is defined as the samples per second one wish to acquire information. As mentioned in Section 5.1.4, both DAQs are synchronized together, therefore the fastest sampling rate obtainable is limited by the slowest DAQ, which for the present setup is the NI USB-6211 at 250 kHz.

The update rate determines the length of time before the screen is updated, which is related to the size of each data segment. If the sampling rate is 1 kHz and the update rate is 0.5 seconds then every half a second the LP will read five hundred samples, or data points, from each active channel on the DAQ. Therefore, as the update rate decreases, the size of each data segment decreases. Additionally, the smaller the data segment the faster the computer can process and write it to a file. For the conducted experiments, an update rate of 0.02 seconds is sufficient to allow all the data to be processed and written to the output files prior to the start of the next cycle.

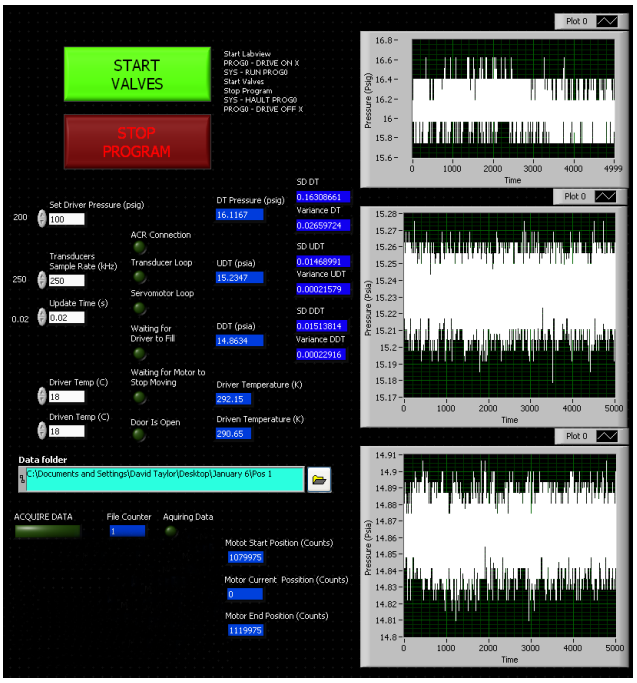

Figure 19 Labview Front Panel (Nation Instruments Corp.)

During any cycle, the input parameters can be changed. These input parameters include the output file location and the thermocouple temperatures.

The output file location is the directory in where all the output files are written. This parameter generally remains unchanged in between cycles but, if desired, one could change it. The LP writes two files every cycle. One file contains the following (in this order):

- Desired driver gas pressure
- Sampling rate
- Update rate
- Driver section thermocouple temperature

- Driven section thermocouple temperature
- Driver gas pressure transducer pressure profiles – OPT
- Upstream driven gas pressure transducer pressure profiles – KPT
- Downstream driven gas pressure transducer pressure profiles - KPT
- RD open switch

The other output file contains the servomotor odometry information in the form of rotational counts and entails the following:

- Starting servomotor location
- Ending servomotor location
- Servomotor location in time

The thermocouple temperatures are manually entered in the front panel at the beginning of each cycle in degrees Celsius. Degrees Celsius are used because that is the output unit of the thermocouple's readout display. In the back panel, discussed later in this section, the LP converts the degrees Celsius into degrees Kelvin before writing the temperatures to an output file.

The reason for manually entering the temperature is a result of not having the proper equipment available that would allow the DAQs to read the thermocouple information. Furthermore real-time temperature profiles are not necessary, therefore, by adding the two extra signals the maximum sampling rate would drop to 200 kHz.

Furthermore, the front panel has three buttons, the Start Valves button, the Stop Program Button, and the Acquire Data button. The Start Valves button is pressed to start

the automation of the servomotor, solenoid valve, and data collection. This button is only pressed after all the system checks and safety checks have been satisfied. The startup procedure is in Appendix B.

The Stop Button is pressed when the desired test has completed. By pressing the Stop Button all processes will finish their current operational loop, which includes properly saving and closing all output files. If the emergency stop button inside Labview (Nation Instruments Corp.) is pressed then any data that is currently being written will become corrupted.

The Acquire Data button is pressed whenever one wants to record data to the output files without running through a test cycle. It is normally used for data recording debugging.

5.2.1.2. Cycle Process Indicators

Additionally, the LP's front panel indicates the progress of the cycle with on screen LEDs, illustrated in Figure 19. These LED's aid in debugging problems in either the LP or the SG's cycle.

5.2.1.3. Real-Time Analysis Tools

The front panel also displays useful information for all of the acquired signals. For the three pressure transducers, an instantaneous graphical plot shows all the data in a single data segment. This plot is very useful for identifying broadband noise. Additionally, the LP computes the mean, standard deviation, and variance of each data segment and presents them on the front panel in the form of numerical displays; they are

colored blue in Figure 19. Moreover, in order to see how the pressure changes in time the mean of each data segment is plotted versus the sample clock.

Additionally, in order to gain a more effective understanding of the EMI level in the system, a plot of the percent standard deviation was created. This plot, in conjunction with the instantaneous plot of each data segment were used in order to find which electrical components induce EMI into the system and the proper order in which the components must be grounded to eliminate as much EMI as possible. This plot of percent standard deviation is created by taking the standard deviation of each data segment and dividing it by the mean of each data segment, then multiplying it by one hundred.

Furthermore, the front panel indicates the servomotors odometry information in the form of position counts, where four hundred thousand counts equal one rotation. The LP obtains the odometry information by communicating with the Aries controller through the ACR-view communications sever program. This connection is established via a serial connection through an Ethernet cable. The communication server and ACR-view are both products of Parker and come with the Aries controller. From this connection, the LP reads a set of bit p12295 from the Aries controller to obtain the motor's shaft location.

5.2.2. Back Panel

The back panel contains the flow chart style of programing that Labview (Nation Instruments Corp.) uses to create a program.

5.2.2.1. Process

The LP's back panel uses two loops, the servomotor control loop and the data acquisition loop. The servomotor control loop controls the servomotor, acquires the odometry information, and opens and closes the solenoid valve. The data acquisition loop acquires, processes, and records the various input signals. These two loops allow the LP to parallel process, thus increasing the speed of the program. The LP goes through the following steps for each desired driver pressure region:

1. The LP starts by using the initialization parameters to setup the DAQs such that all the desired input signals can be acquired and all of the output signals can be sent.
2. The LP synchronizes the DAQs and starts the data acquisition loop where the LP starts acquiring the driver gas pressure, driven gas pressure, and RD open switch data one segment at a time. Additionally, the Transducer loop LED indicator on the front panel is turned on.
3. The LP checks for a connection with the Aries motor.
    a. The LP sets bit 129 to true, which loads the preprogramed motion profile into the servomotors memory.
    b. The ACR connection LED indicator on the front panel is turned on.
    c. The LP starts the servomotor control loop where it waits for the Starts Valves button to be pressed on the front panel.
    d. Data acquisition loops starts recoding the servomotor's odometry information every servomotor loop cycle by reading bit p12295.

4. At this point the real-time analysis tools: mean values, variance, standard deviations, and percent standard deviation are computed and displayed on the front panel inside the data acquisition loop.

Once the Transducer loop LED and ACR connection LED are on, which takes on the order of milliseconds, the Starts Valve button can be pressed. In the meantime, the data acquisition loop continues to read the input signals and compute the various real-time analysis tools.

5. Once the Start Valves button is pressed on the front panel, the LP:
    a. Turns on the Servomotor loop LED indicator on the front panel
    b. Sets bit 128 to true on the Aries controller, thereby, activating one rotation of the pre-programed motion profile of the servomotor
    c. Obtains the initial servomotor odometry location by reading bit p12295 and calculates the final odometry location
6. After the servomotor starts to move, bit p4112 is read inside the servomotor control loop to determine if the servomotor is rotating. If it is then the Waiting for Motor to Stop Moving LED indicator on the front panel is turned on.
7. A wait timer inside the servomotor control loop halts activity in the loop for 2 seconds. After which the solenoid valve is triggered open by the process mentioned in Section 4.5.

The 2 second wait period allows the RCS to close and seal the RD.

8. Once the solenoid valve opens, the regulated compressed air fills the driver section. Additionally, the Waiting for Driver to Fill LED indicator on the front panel is turned on.
9. When the driver gas pressure reaches 90% of the desired driver gas pressure initialization parameter, the driver gas pressure, driven gas pressure, RD open switch, and servomotor odometry information starts to be recorded to their respective output files. Additionally, the Acquiring Data LED indicator is turned on.
10. Once the driver gas pressure reaches 95% of the desired driver gas pressure initialization parameter
    a. The servomotor control loop waits 1.8 second before turning off the solenoid valve, which allows the system to reach its maximum pressure.
    b. The Waiting for Driver to Fill LED indicator on the front panel is turned off.

By the time the solenoid valve closes, there is about a half a second before the bottom of the RD lines up with the RCS' cutout section and allows the pressurized driver gas to push the RD open.

11. As the RD opens, the driver gas pressure will drop. When the driver gas pressure falls below 90% of the desired driver gas pressure initialization parameter a counter starts. The counter counts to ten updates, or ten data acquisition loop cycles, before halting data recording. Additionally, the Acquiring Data LED indicator is turned off.
12. After the data has stopped recording, the output files are closed.

At this point in time, another wait timer inside the servomotor control loop halts activity for 2 second in order to allow the servomotor to stop moving, all the driver gas to vacate, to allow the RD to fall back down to its closed position, and to allow the output files to be closed.

13. When all the output files are closed, a file counter increases by one, such that output files are not overwritten.
14. After the 2 second wait time in the servomotor control loop has elapsed, a new cycle starts from Step 4.

5.2.2.1. Speed Optimizations

The purpose for optimizing the speed of the LP is to ensure that all the data can be written to the appropriate output files prior to the next cycle, where new output files are opened. If new output files are opened prior to closing the current output files then the LP will crash and the data will be lost. Therefore, three processes were implemented to optimize the speed of the LP.

1. The update time initialization parameter is reduced until the LP does lasts for at least ten cycles. Then one can assume it will last for cycle numbers much larger than ten.
2. All output files are written in a binary format, which is the fastest format possible.
3. While recording data to output files no real-time analysis tools are calculated or displayed on the front panel, which reduces the workload onto the computer's CPU.
4. To further reduce the computer's CPU workload, while the Start Valve button is pressed on the front panel only the graphical plot and numerical display of the mean driver gas pressure are displayed.

5.3. Post Processing Program

All of the post processing and data reduction was completed using an in-house Matlab program (The MathWorks, Inc.). This Matlab program (The MathWorks, Inc.) has three hierarchical levels. The lowest level processes each cycle individually. The middle level processes the information from each cycle and computes statistics for the each pressure region. The upper level processes the statistical information from each pressure region and produces performance information for the entire Shock Generator over the entire desired driver gas pressure range.

As a reminder, the objective of this study is to characterize the performance and determine the feasibility of the rotating door and locking cam-shaft valve (RDLCSV) apparatus as an alternative to other shock wave generating mechanisms. In order to accomplish this task, the two driven gas pressure maximum value, profile shape, and calculated shock wave Mach number (M_s) must be compared to that predicted by ISTT in order to obtain a comprehensive analysis that truly assesses the accuracy Shock Generator (SG). The cycle analysis function obtains and compares the calculated shock wave Mach number (M_s) to that predicted by ISTT. The performance analysis function obtains the mean driven gas pressure profiles (DPP) and the mean maximum driven gas pressure value or post shock wave gas pressure of an entire desired driver gas pressure region and compares them to the theoretical DPP and post shock wave gas pressure (PSP).

5.3.1. Lower Level – Cycle Analysis

The cycle analysis function of the Matlab program (The MathWorks, Inc.) completes the following steps each time it is called by the statistical analysis function in order to compute and compare the calculated M_s to that predicted by ISTT:

5.3.1.1. Reading in the Data

1. The desired driver gas pressure, cycle number, plotting type, and output type variables are obtained from the statistical analysis function.
2. The appropriate desired driver gas pressure and cycle number output file, from the in-house Labview program (Nation Instruments Corp.), are opened and read into the Matlab (The MathWorks, Inc.) workspace. The Labview (Nation Instruments Corp.) output file contains the sampling frequency, update rate, temperature, pressure, and RD open switch information.
    a. The sampling frequency, update rate, and temperatures are read first because these are single values and they are at the beginning of the output file.
    b. The sampling frequency and update rate are used to parse the rest of the Labview (Nation Instruments Corp.) output file in order to reconstruct the driver gas pressure, driven gas pressure, and RD open switch information, which were written one segment at a time, illustrated by Figure 20.

Labview Output File Layout

Driver Pressure Transducer Segment 1	Upstream Driven Pressure Transducer Segment 1	Downstream Driven Pressure Transducer Segment 1	RD Open Switch Segment 1
Driver Pressure Transducer Segment 2	Upstream Driven Pressure Transducer Segment 2	Downstream Driven Pressure Transducer Segment 2	RD Open Switch Segment 2

Figure 20 Labview Output File Layout

3. Once the pressure and limit switch data have been read into the workspace, the output file is closed and all intermediate values are deleted.

Because a few seconds of data is recorded every cycle and the region of interest (the large pressure rise indicative of a shock wave) is on the order of milliseconds, only a few time data segments are necessary in order to capture the entire region of interest. Because the region of interest will occur near the end of the Labview (Nation Instruments Corp.) output file, the reconstruction of the pressure and RD open switch information starts at sixteen data segments from the end of the file. This process decreases the size of the vectors processed in Matlab (The MathWorks, Inc.) thus increasing processing time.

4. The servomotor odometry output file is opened.
5. The servomotor starting rotational position, ending rotational position, and rotational position in time is read into the Matlab (The MathWorks, Inc.) workspace.
6. Using the starting rotational position and ending rotational position, the rotational position in time of the servomotor is scaled from position count to 0° to 360°.

7. The servomotor odometry output file is closed.

5.3.1.2. Pressure Profile Reduction Processing

1. The measured driver gas pressure is obtained by finding the maximum value from the driver gas pressure transducer or OPT.
2. The driven gas pressure measurements from the KPT are converted from absolute pressure to gauge pressure such that they start from zero psig. This is accomplished by taking the mean of the first one hundred data points in each pressure measurement, which is far upstream of the event, and subtracting this mean from the entire pressure signal.
3. Each driven gas pressure measurement passed through a loess moving average filter using the "smooth" function in Matlab (The MathWorks, Inc.). This filter is used to eliminate the remanding EMI from the signals and smooth out oscillations along the first pressure rise of the driven gas pressure profiles. The loess option in the "smooth" Matlab (The MathWorks, Inc.) function uses a weighted linear least squares and a 2^{nd} degree polynomial model. When the filter considers one hundred data points in its averaging the best results are produces.

The product of the loess filtering can be observed in Figure 15 from Section 5.1.1 and Figure 21 below. From Figure 15, we can see that the loess filtering does indeed smooth out oscillations along the first pressure rise of the DPP. Therefore, instead of having an erratic time differences along the first pressure rise of the DPP, the behavior is smoothed out, resulting in a time difference of ~0.180 milliseconds, ~0.128 milliseconds, and

~0.180 milliseconds at the base, middle, and peak, respectively. Thus, it seems as if the trend of the profiles is converging then diverging. However, then we look at a similar DPP at a driver gas pressure of 200 psig, represented by Figure 21, we see that the first pressure rise of the DPP is smoothed out significantly by the loess filtering, resulting in a time difference of ~0.252 milliseconds, ~0.192 milliseconds, and ~0.144 milliseconds at the base, middle, and peak, respectively. Thus, it seems as if the trend of the profiles is converging. This information will become important in the next section that discussed the method for obtaining the wave speed.

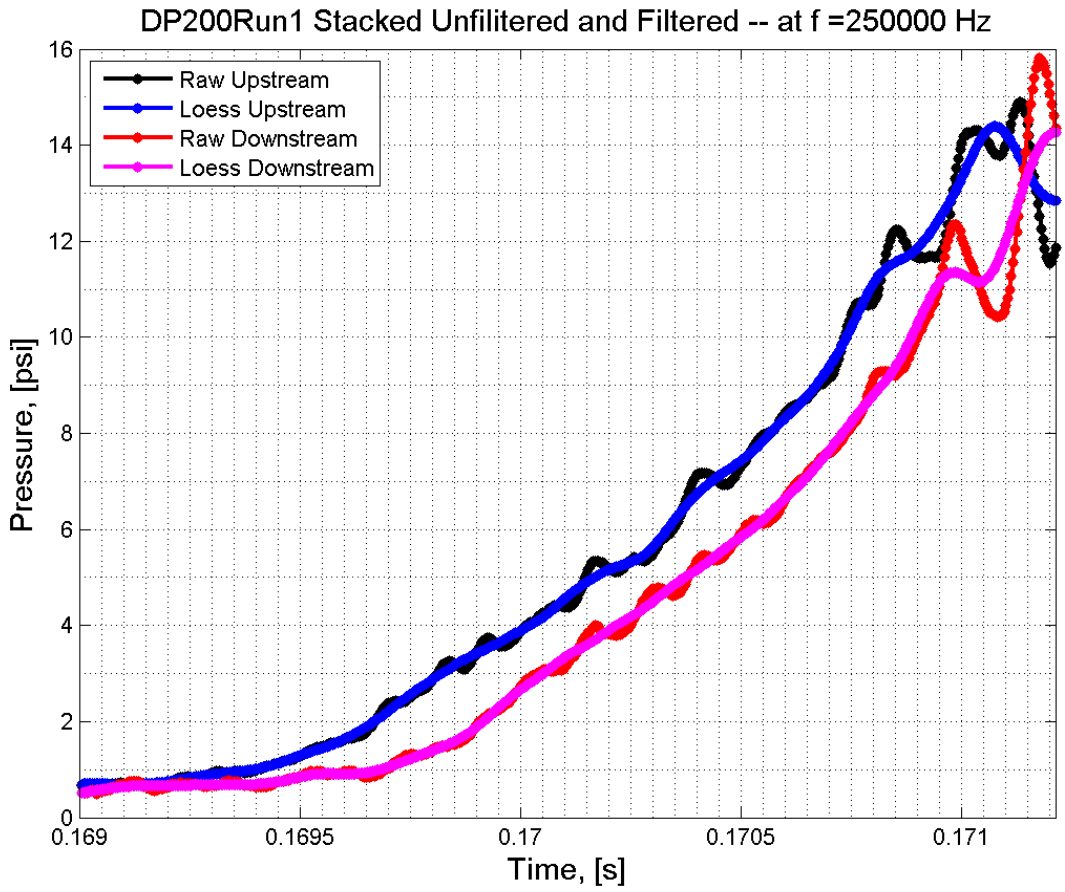

Figure 21 200 psig Stacked Unfiltered and Filtered Transducers

4. The loess filtered driven gas pressure signals are saved as separate vectors such that future processing can be conducted on the raw signals.
5. Processing speed is increased by reducing the size of the driven gas pressure vectors to only the region of interest and a small region around the event. This is accomplished by:
    a. Finding the location of the maximum value along the first pressure rise from each loess filtered driven gas pressure signal
    b. Surround the maximum value with ten thousand points on either side

Therefore, the millions of data points recorded every cycle are reduced to twenty thousand data points to contain the passing pressure wave information. This data region is used for the remainder of the cycle analysis function.

6. The measured post shock wave gas pressure is obtained by taking the maximum of the maximum value along the first pressure rise from each unfiltered driven gas pressure signal.

5.3.1.3. Shock Wave Mach Number Calculation

From the beginning of Section 5.3, the purpose of the cycle analysis function is to obtain and compare the shock wave Mach number (M_s) to that predicted by ISTT, which is dependent on the driver gas pressure. However, because, the RD has a finite opening time, as explained in Section 3.3, and the SG system has losses, the calculated M_s might be representative of a theoretical M_s that is predicted by the maximum driven gas pressure or post shock wave gas pressure (PSP).

Therefore, the upper bound is set by the M_s predicted by the driver gas pressure because when using ISTT, one assumes an instantaneous opening time and calculates all values based on the driver gas pressure. The lower bound is set by the M_s predicted by post shock wave gas pressure (PSP) because it inherently accounts for losses in the system, namely slow opening time, leaks, and expansions in the SG.

From the previous section, the measured driver gas pressure (P4) and the measured post shock wave gas pressure (PSP) are known. Therefore, by using table lookup functions in Matlab (The MathWorks, Inc.), the theoretical M_s predicted by P4 and PSP can be obtained. This table was constructed using normal shock wave relations.

Once the theoretical values of the shock wave Mach number (M_s) are determined, the M_s can finally be obtained. The simplest and most effective way of calculating the M_s from the two driven gas pressure profiles with a known separation distance is by the following process:

1. Find the time difference (Δt) between the two driven gas pressure profiles (DPP) by locating the time of the first pressure rise in each DPP, then subtract these times from each other. The first pressure rise is chosen because ISTT predicts that the pressure rise across a shock wave is a step function, thus it the most logical location for time difference calculations. To illustrate this further, consider the DPP in Figure 22. Locate the pressure value (y-axis) that is halfway up the pressure rise (~15 psi), then draw a horizontal line. Next, subtract the time location (x-axis) of the two points (one point from each signal) that intersect this horizontal line to obtain a time difference (Δt).

2. Find the velocity between the two pressure signals by the following equation:

$$\text{Velocity} = \frac{\Delta x}{\Delta t} = \frac{0.09708}{\Delta t}\left[\frac{m}{s}\right] \tag{5.2}$$

Where Δx is the driven gas pressure transducer separation distance and Δt is the time difference. From Section 5 the KPT are separated by 97.08 mm (3.822”).

3. Calculate an estimate for the local speed of sound using the ambient temperature measured from the thermocouple in the muffler as discussed in Section 5.1.2, by the following equation.

$$a = \sqrt{\gamma \cdot R \cdot T} = \sqrt{1.4 \cdot 286.9 \cdot T} \tag{5.3}$$

Where γ is the ratio of specific heat of air, which is 1.4 for the temperatures involved in all conducted experiments. R is the gas constant of air, which is 286.9.

4. Calculate the shock wave Mach number or wave speed from the calculated velocity in Step 2 and the estimated speed of sound in Step 3 using the following equation:

$$M_s = \frac{\text{Velocity}}{\sqrt{\gamma \cdot R \cdot T}} = \frac{\text{Velocity}}{\sqrt{1.4 \cdot 286.9 \cdot T}} = \frac{0.00484}{\Delta t \cdot \sqrt{T}} \tag{5.4}$$

Therefore, the M_s is calculated in four simple steps. However, from Figure 22, it is clear that the slope of pressure rises for both driven gas pressure transducers are not step functions. Moreover, they do not have a constant slope, which is most apparent from the loess filtering justification in the previous section. Therefore, one must determine the most appropriate location to obtain the time difference between the two DPP. It was determined that the most appropriate location lies in between 30% to 70% of the pressure rises. Therefore, a mean time difference (Δt) of all the points within the

pressure threshold parameter, 30% to 70% of pressure rise region, would provide the most comprehensive representation of the time difference between the two DPP.

To illustrate the pressure threshold parameter concept further, review Figure 22. The red and magenta points along pressure rise of the upstream DnT and the downstream DnT respectively, highlight the pressure threshold parameter. The horizontal green lines represent the time difference (Δt) between individual points. Within the pressure threshold parameter of Figure 22 three hundred Δt are calculated. However, from Figure 22, it is apparent that some of the green lines are larger than others; therefore, an average of all three hundred Δt would provide the best result. Consequently, one M_s is obtained for one pair of driven gas pressure profiles (DPP) of each cycle.

In order to obtain an understanding of how filtering alters the calculated M_s, this process is completed for the raw, loess filtered, normalized raw, and normalized loess filtered driven gas pressure data. Furthermore, it became clear that the most accurate results are obtained when the driven gas pressure measurements start from the same pressure and rise to their respective locations, thus converting the driven gas pressure measurements to gauge pressure is a useful step.

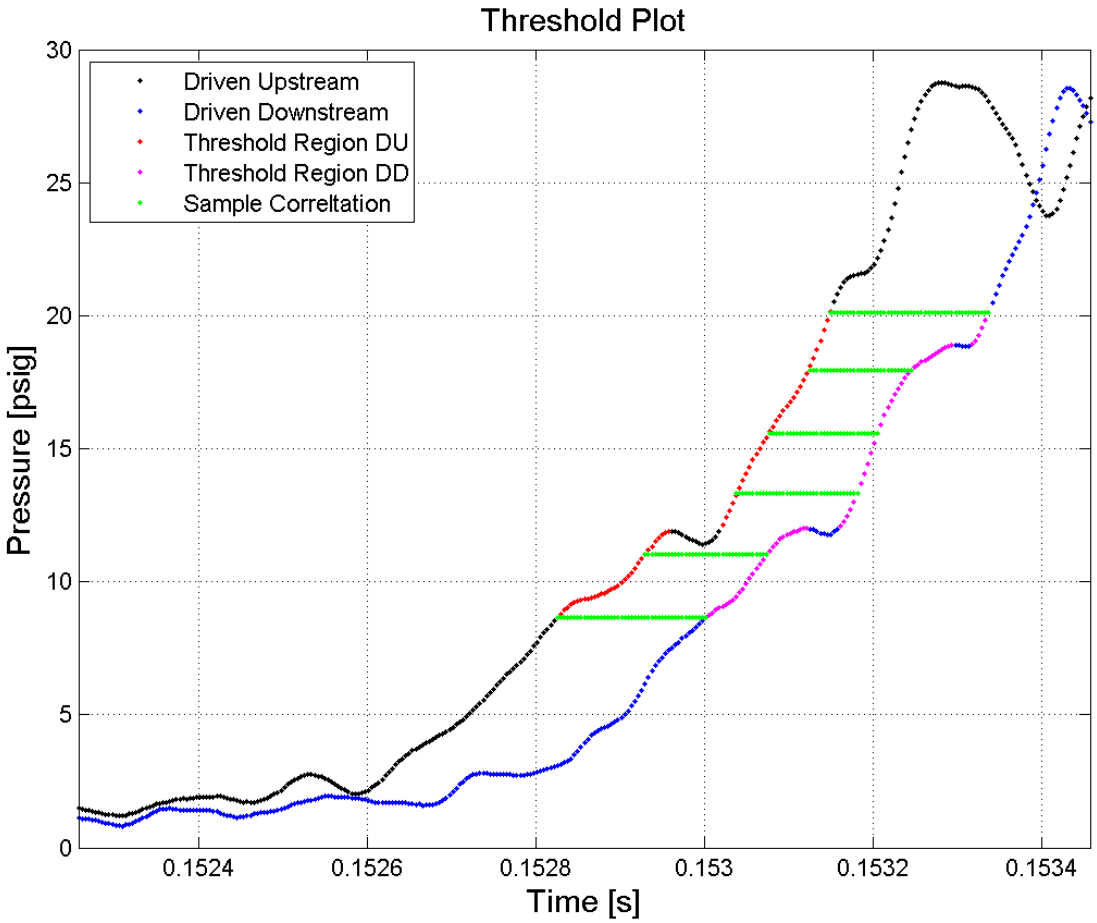

Figure 22 Threshold Plot

Additionally, as we can see in Figure 22, the rising slopes of the measured driven gas pressures are not asymptotic as theory predicts. The cause of this phenomenon is fluid dynamics, the rise time and response time limitation of the Kulite driven gas pressure transducers, or lowpass filtering the DPP. The lowpass filtering option was eliminated as by comparing cycles at the same driver gas pressure with the lowpass filter turned on and off. The results concluded that the lowpass filtering had no noticeable influence on the rising slopes of the measured driven gas pressures. Therefore, if the

phenomenon is caused by the rise time and response time limitation of the Kulite driven gas pressure transducers, then the only option would be to use PCB transducers as time of arrival sensors. PCB transducers have nanosecond response times and rise times but they can only measure pressure fluctuations and not the pressure value. Because, as will be explained later, the analysis of the post shock wave gas pressure (PSP) is important, the Kulite pressure transducers are used. Moreover, as explained in the Future Work and Lessons Learned Section, the facility should be instrumented with both Kulite and PCB transducers.

Finally, the results of the calculated M_s for each type of pressure signal (raw, loess filtered, normalized raw, and normalized loess filtered) are displayed on the screen and / or recorded to an output file.

The cycle analysis function also allows for any combination of the driver gas pressure, driven gas pressures, RD open switch, and servomotor odometry data to be plotted using any combinations of raw, loess filtered normalized raw, and normalized loess filtered driven gas pressure data.

To compute the normalization filtered values (zero to one) of the driver gas pressure, RD open switch, and servomotor odometry data the following equation is used:

$$\text{Normalized Signal} = \frac{\text{Signal} - \text{Signal}_{min}}{\text{Signal}_{max} - \text{Signal}_{min}} \tag{5.5}$$

However, to compute the normalized filtered values of the of the driven gas pressure signals the Signal_{max} and Signal_{min} values equal the global maximum and global minimum values from both driven gas pressure transducers. As will be discussed in the

Results Section (Section 6) the normalization filter values are only useful for viewing plots because it changes the slopes and thus the results for the calculated M_s.

5.3.2. Middle Level – Statistical Analysis

The statistical analysis function of the Matlab (The MathWorks, Inc.) program receives the desired driver gas pressure, cycle number, plotting type, and output type variables from the performance analysis function then calls the cycle analysis function for each cycle of the desired driver gas pressure region and computes the maximum, minimum, mean, and standard deviation for following measurements:

1. Driver gas pressure (P4)
2. Post shock wave gas pressure (PSP)
3. Driver and driven gas temperature
4. Calculated M_s
5. Theoretical M_s from the
    a. Driver gas pressure
    b. Post shock wave gas pressure
6. Driven gas pressure profiles (DPP)
    a. Raw
    b. Loess filtered
    c. Normalized raw
    d. Normalized loess filtered

These statistical values were calculated using Matlab's (The MathWorks, Inc.) imbedded functions ("max", "min", "mean", "std"). Furthermore, the percent standard deviation for the calculated M_s is calculated by the following equation.

$$\text{Percent Standard Deviation} = 100 \cdot \frac{\text{Standard Deviation}}{\text{Mean}} \tag{5.6}$$

The standard deviation and the mean in the equation are computed for all the calculated M_s of the desired driver gas pressure region and are used to determine the accuracy of the SG. The percent standard deviation is also explained in Section 5.2.1, and is used as a measure for the repeatability of the SG in the Results Section (Section 6).

Once the statistics are computed, they can be displayed onto the screen and / or written to an output file. Normally, the statistics are both written to the screen and to an output file.

Next, the Statistics Analysis function produces several difference plots such as plotting all the upstream or downstream driven gas pressure profiles on top of each other, illustrated in Figure 23. Figure 23 illustrates the inconstancy in the driver fill time, run times, and repeatability because the data is recorded when the drive gas pressure is 95% of the desired driver gas pressure as discussed in Section. A possible better solution could have been to use the servomotor rotational location.

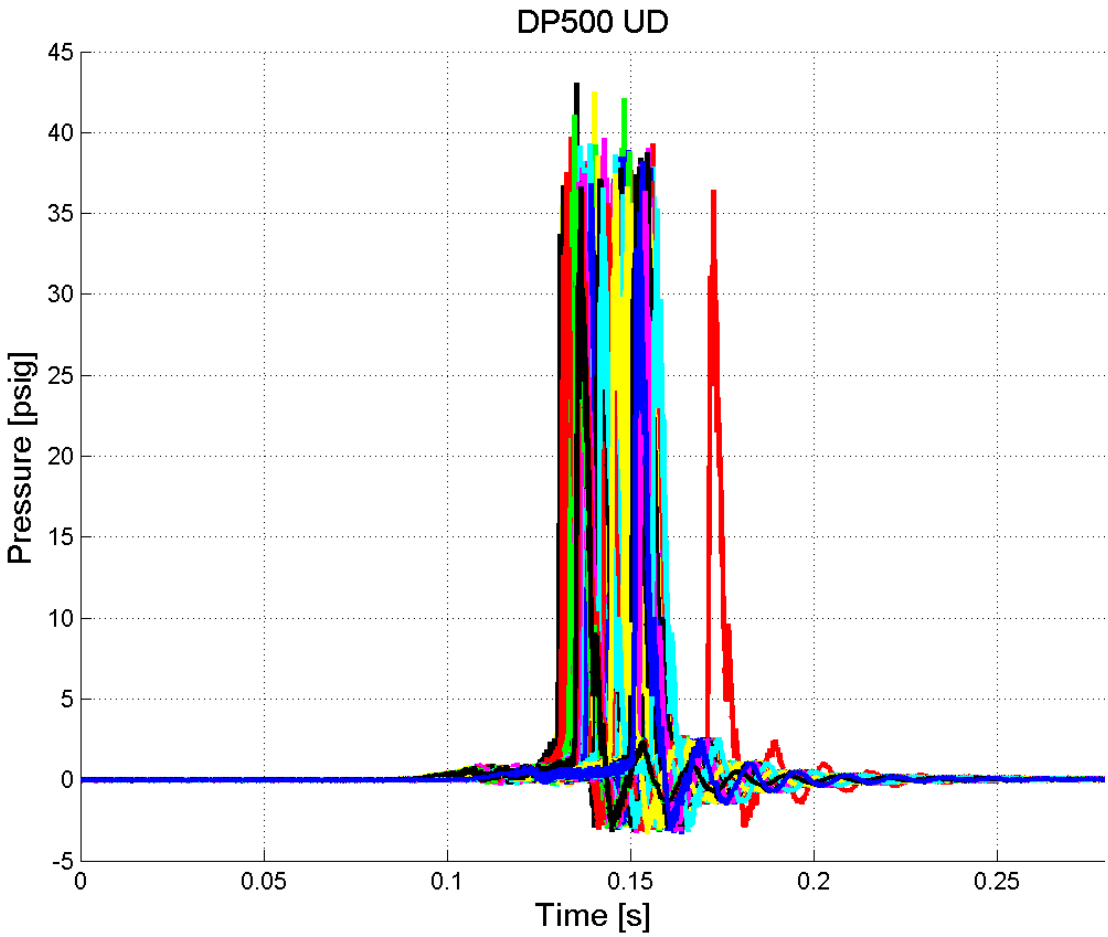

Figure 23 Upstream Pressure Variation – 100 cycles

Another plot option in the statistical analysis function is the time shifted upstream or downstream driven gas pressure profiles. These pressure profiles are time shifted to the location of ten percent of pressure rise. This plot aids in determining how the rising slope changes over the entire desired driver gas pressure region, which is used for the repeatability analysis in the Results Section (Section 6). A sample is illustrated in Figure 24. Further plot options involve comparing individual driven gas pressure profiles to those pressure profiles predicted by ISTT. However, for a more accurate description

of the driven gas pressure profile for the entire desired driver gas pressure region, the mean driven gas pressure profile is compared to the pressure profile predicted by ISTT in the performance function.

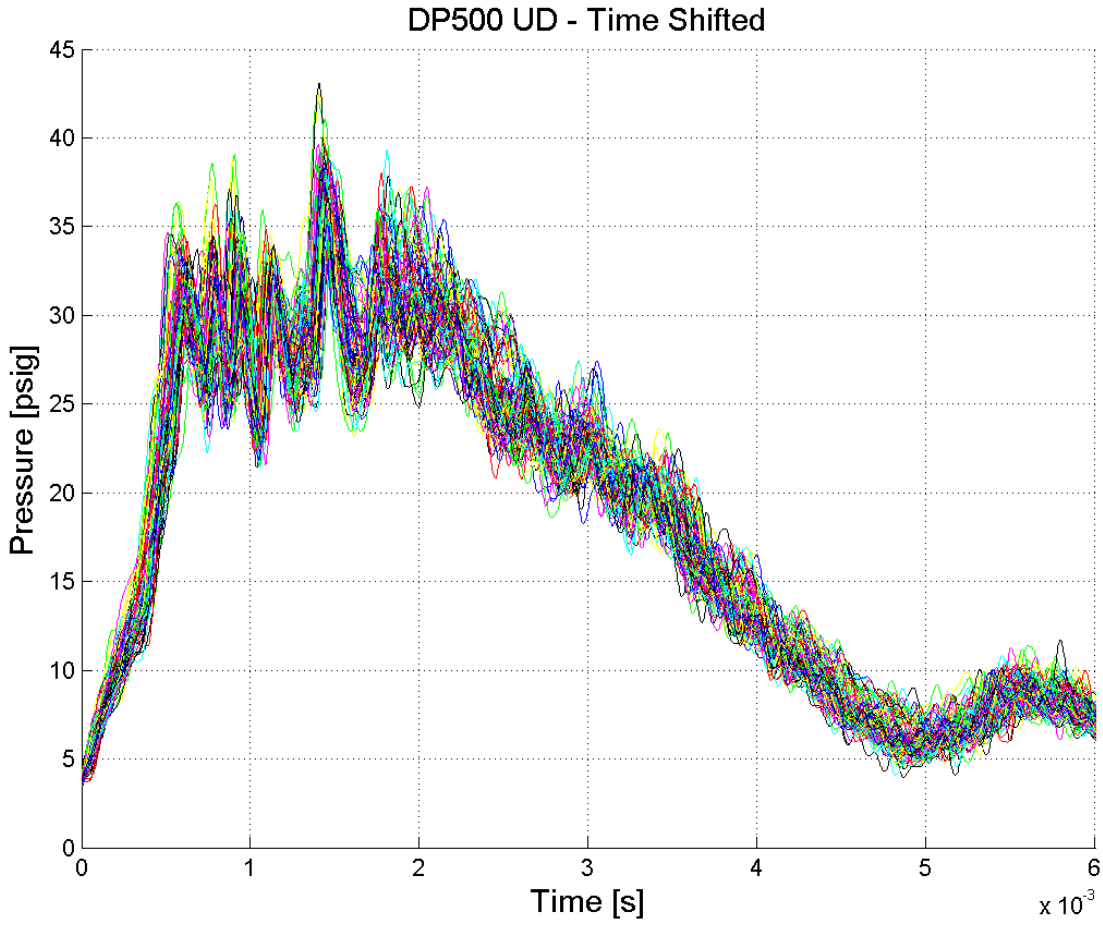

Figure 24 Upstream Pressures – 100 cycles

5.3.3. Upper Level – Performance Analysis

The performance analysis function of the Matlab (The MathWorks, Inc.) program sets all desired driver gas pressure, cycle number, plotting type, and output type variables that will be processed by the statistical analysis function. From the output of the statistical analysis function, three plots are produced.

1. Plot all the statistical measurements of the calculated shock wave Mach number from all the desired driver gas pressure regions onto one plot. This plot is particularly useful in analyzing how the calculated M_s of the SG compares to the M_s predicted by ISTT.
2. Plot all the mean upstream and downstream driven gas pressure profiles (DPP) from all the desired driver gas pressure regions onto one plot.
3. Plot the mean DPP and the theoretical driven gas pressure profiles predicted by ISTT. This plot offers a comparison between the measured and theoretical PSP and DPP, which was determined to be necessary in Section 5.3 in order to provide a comprehensive analysis of the accuracy of the SG.

The mean upstream and downstream DPP are calculated by taking the average of the time shifted upstream and downstream driven gas pressure profiles at each time location, respectively, which were calculated in the statistical analysis function. This plot is particularly useful in analysis how the driven gas pressure profiles change as the driver gas pressure increases.

6. RESULTS

To reiterate, the purpose of this master's thesis project is to assess the feasibility of a rotating door and locking cam-shaft valve (RDLCV) mechanism as an alternative to currently available diaphragmless shock tube designs by characterizing the performance of this mechanism in the Shock Generator (SG) facility at Texas A&M University. The quality of the SG's performance is characterized by the following four metrics:

1. Accuracy
2. Repeatability
3. Shock wave Mach number range
4. The shock wave formation distance

Thus, in order to acomplish this task, driver gas pressures from 100 to 500 psig in increments of 100 psig were tested. At each driver gas pressure one hundred runs or cycles were completed, which ensures that all statistical calculations have an adequate statistical value based on an error analysis.

6.1. Accuracy

The accuracy of the Shock Generator is defined by comparing the following parameters to their representative thoeretical values:

1. Measured driven gas pressure profiles (DPP)
2. Maximum value of the measured driven gas pressure or the post shock wave gas pressure (PSP)
3. Calculated shock wave Mach number (M_s)

The methods for measuring, calculating, and comparing these parameters were discussed in Section 5.3. By analysing the driven gas pressure profile shape, the PSP value, and the calculated M_s, a comprehensive analysis is completed that truly assesses the accuracy Shock Generator (SG).

Therefore, in order to understand how the driven gas pressure profiles (DPP) are predicted by ISTT, an XT diagram can be used. Figure 25 shows an XT diagram for the SG at a desired driver gas pressure of 513 psig. The XT diagram illustrates how the shock wave, expansions fans, and contact surface move through the SG in time (y-axis) and space (x-axis) during a single cycle.

The expansion fans (colored blue) form inside the driver section and will typically move to the left, towards the driver section's filling flange. If the driver gas pressure to driven gas pressure ratio (DDPR) is large enough then a right moving expansion wave will form as well. Eventually, the initially left moving expansion fans will reflect off the driver section's filling flange and move rightward. Once all the expansion fans are moving downstream, they will catch up and interact with the downstream moving shock wave (colored black). The contact surface (colored red) is the moving interface between the driver gas and the driven gas. Additionally, the magenta and cyan lines represent the location of the two driven gas pressure transducers (DnT or KPT). Therefore, at any given spatial location inside the SG, one can observe when an event will occur.

The reflection at the right end of Figure 25 represents the reflection of the shock wave off the driven section's end cap flange, which is ignored because the SG has a

muffler, instead of an end cap, that vents the driver gas directly into the atmosphere, therefore no reflection will occur.

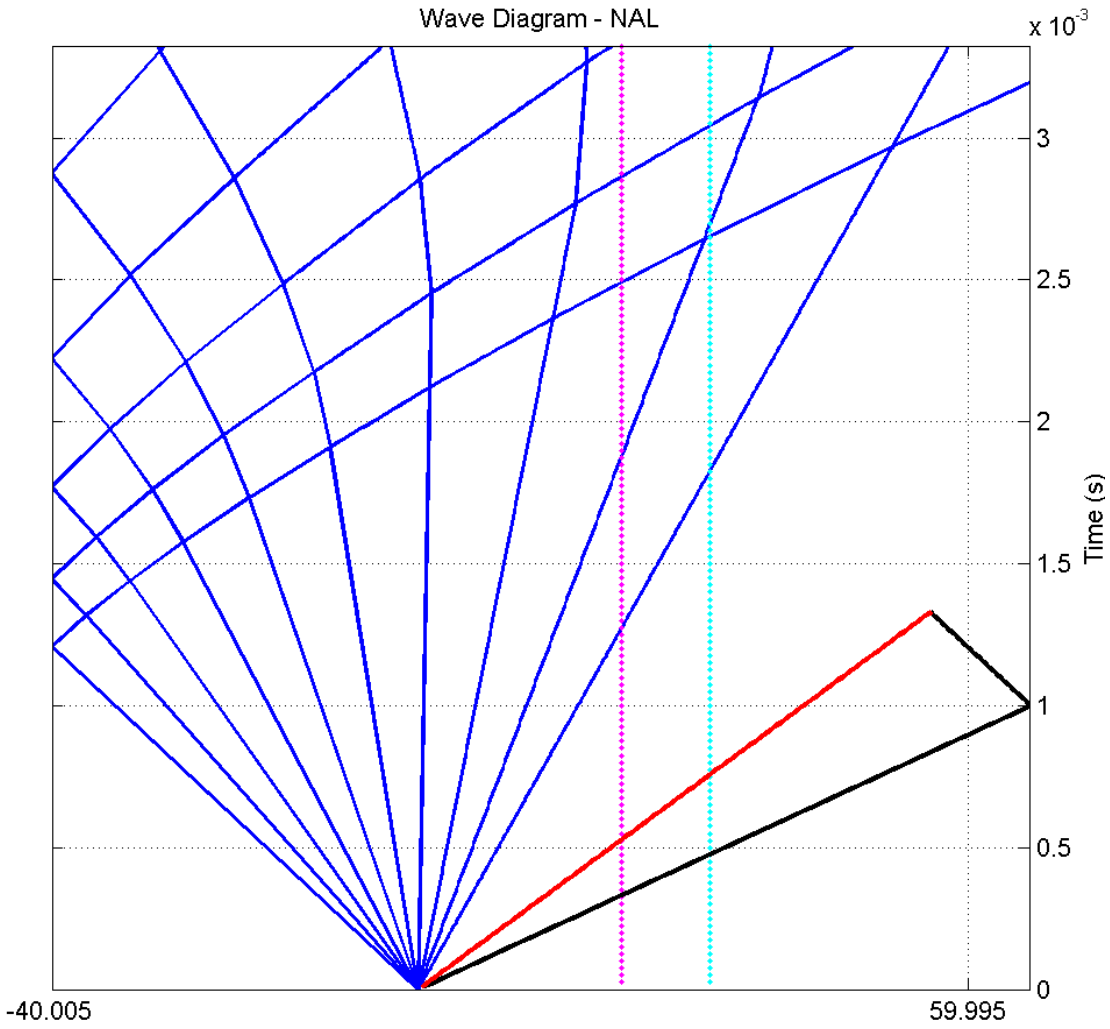

Figure 25 XT Diagram

Because the XT diagram illustrates when events will occur during a cycle at any spatial location in the SG, theoretical driven gas pressure profiles (DPP) can be created

from the XT diagram. At each DnT location, a timer starts from zero when the diaphragm or in this case the RD opens. The measured driven gas pressure by the DnT will be zero until the shock wave passes by. At this point, the DnT will measure the theoretical PSP value predicted by the normal shock wave relations of ideal shock tube theory (ISTT) based on the desired driver gas pressure. For the XT diagram in Figure 25 the driver gas pressure is 513 psig, therefore, the PSP is 66.7 psig. According to ISTT and driven gas pressure measurements from traditional shock tubes, the driven gas pressure measured after the shock wave passes (PSP) remains constant until an expansion fan passes by. Each passing expansion fan reduces the measured driven gas pressure. Therefore, as each wave passes the DnT a segment of the driven gas pressure profile can be constructed.

The region of constant driven gas pressure in between the passing shock wave and the passing expansion fans is referred to as the constant pressure region in a shock tube. Additionally, the definition of shock tube run time is the length of time of the constant pressure region.

Figure 26 represents the comparison between the upstream and downstream theoretical DPP[4] described above and the mean DPP for one hundred cycles at a driver gas pressure of 513 psig. How the mean DPP were obtained is described in Section 5.3.3. In Figure 26, the black line and blue line refer to the upstream theoretical driven gas pressure profile and the downstream theoretical driven gas pressure profile,

[4] As a note, the XT diagram and the theoretical driven gas pressure profiles are produced by another in-house Matlab (The MathWorks, Inc.) program titled Hypersonic Shock Tunnel/Tube Program whose operation is not described in this document.

respectively. They are based on the mean driver gas pressure (P4) of 513 psig. The red line and the magenta line refer to the upstream theoretical driven gas pressure profile and the downstream theoretical driven gas pressure profile, respectively. They are based on the mean driver gas pressure at the location of the post shock wave gas pressure (P4@PSP) of 449 psig. The green line and the cyan line refer to the upstream mean driven gas pressure profile and the downstream mean driven gas pressure profile, respectively. Additionally, the vertical dashed lines on the theory DPP represent the time at which the expansion fans[5] pass the DnT.

The theoretical DPP for the driver gas pressure at the location of the post shock wave gas pressure (P4@PSP) is a result of the rotating door's (RD's) opening time. As the RD opens, some driver gas escapes from the driver section, thus reducing the driver gas pressure. Additionally, ISTT states that the pressure of the bulk moving driver gas dictates the resulting PSP. Therefore, if the RD opens slowly (Ø1 millisecond) in comparison to theory (instantaneous opening times), then the reduction in the driver gas pressure from the leaking driver gas as the RD is opening, results in lower post shock wave gas pressure produced from the lower driver gas pressure. Therefore, the theoretical DPP of P4@PSP must be analyzed. To illustrate this concept review Appendix D.

[5] The expansion fans are difficult to model with the available tools; therefore, this study does not analyze them.

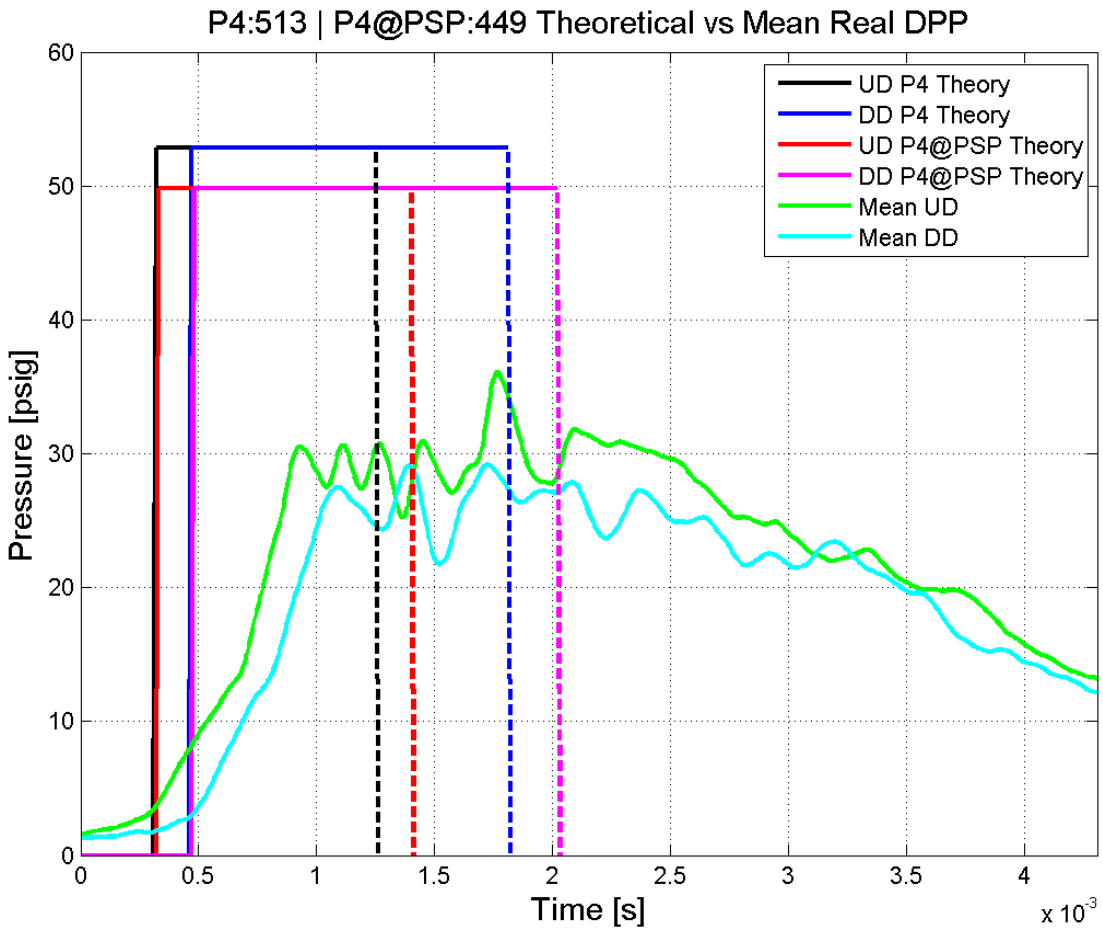

Figure 26 Real vs. Ideal Driven Gas Pressure Profiles

From Figure 26, one can see that the mean DPP are not vertical asymptotes as ISTT predicts. However, it appears that the timing of the events illustrated by the XT diagram is correct. To investigate the comparison of the DPP in Figure 26 further, let us assume the mean DPP has asymptotic slopes along their first pressure rise. In order to perform this assumption, the location of the PSP in the upstream mean driven gas pressure profile is shifted in time to match PSP location of the upstream theoretical

driven gas pressure profile. The time separation between the upstream and downstream DPP remains unaltered. Figure 27 represents this assumption.

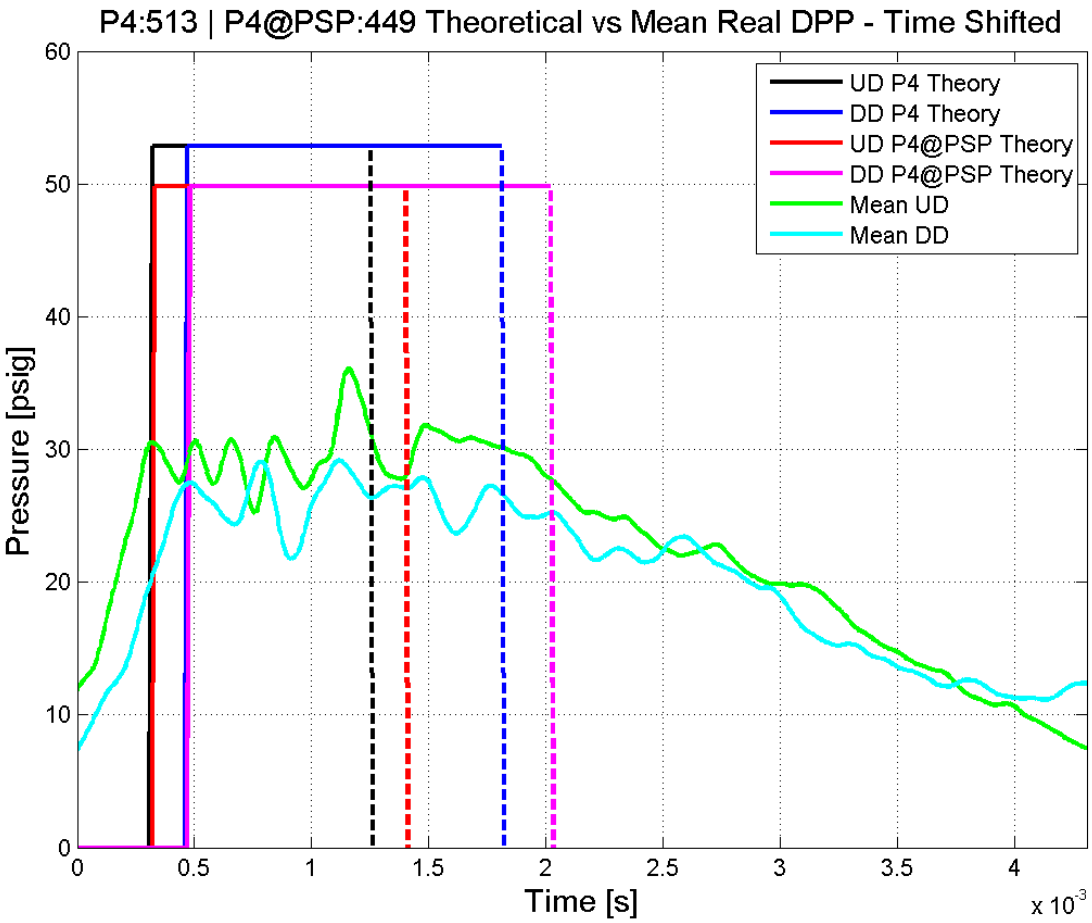

Figure 27 Time Shifted Real vs. Ideal Driven Gas Pressure Profiles

From Figure 27, one can observe that the measured mean PSP is ~30 psig, where the theoretical value using the mean driver gas pressure of 513 psig is 52.8 psig and using the mean driver gas pressure at the post shock wave location of 449 psig is 49.8

psig. Thus, at an average driver gas pressure of 513 psig the mean PSP is more than 50% of that predicted by ISTT, 57.8% of P4 theory and 61.3% of P4@PSP theory. Additionally, the difference in the result between the P4 theoretical lines and the P4@PSP theoretical lines is negligible (5.7%). Although the purpose of the P4@PSP theoretical line is to accommodate for some losses in the system by providing a theoretical PSP value that is closer to the measured PSP value, there is still a great discrepancy between the values. For mean driver gas pressures other than 513 psig, similar plots to Figure 26 and Figure 27 can be found in Appendix A.

However, the discrepancy between the measured mean PSP value and the theoretical PSP values is expected for numerous reasons. First, as described in Section 4, the driver section has smaller cross sectional area than the driven section. Moreover, the cross sectional area through the support piece that holds the RD in place is slightly smaller than the cross sectional area of driver section. Therefore, the overall flow expands as it passes from the driver section to the driven section. Literature on shock tubes with area changes states that if the area is contracted from the driver section to the driven section then the shock waves will form at shorter distances and have higher PSP values than ISTT theory predicts [18]. Therefore, by having an expansion through the driver section to the driven section, we should expect weakened shock waves, resulting in lower than predicted PSP values.

Second, the measured flow field could be a complicated structure that results in the discrepancy between the measured mean PSP value and the theoretical PSP values. A compression region that has not fully formed into a shock wave is a potential result

because it would resemble a bulk fluid moving at the predicted wave speed but with compression waves continuously stacked on top of each other. Another complicated flow field could be one involving interactions between the boundary layer and oscillating shock waves traveling normal to the flow direction. This phenomenon has been observed by Mendoza[6] using simulated ducted flows with area changes. Additionally, this could explain the significant oscillations observed in the constant pressure region, where each oscillation in the DPP represents each time the oscillating shock wave hits the driven gas pressure transducer. As observed by Mendoza, this shock wave is oscillating normal to the flow, thus resonating between the driven sections' centerline and ceiling as well as the centerline and the floor.

Third, this discrepancy could be a result of three dimensional effects, viscous losses, circulation regions near the wall, pressure leaks though the walls of the driven section, or a boundary layer effect that causes the wall driven gas pressure to not equal the centerline driven gas pressure. However, for a mean driver gas pressure of 513 psig the door appears to open sufficiently fast to provide a profile shape that resembles a shock wave profile.

Additionally, in Figure 27, it appears that the time separation between the upstream and downstream DPP is exactly what theory predicts. Furthermore, it appears that the constant pressure region time and the location of the first passing expansion fan

[6] A companion PhD student within the Texas A&M University Aerospace Engineering Department performed the original design.

occurs as predicted by the P4 theory lines and not that predicted by the P4@PSP theory lines.

Certain trends appeared when the same process of comparing the mean measured PSP to the theoretical PSP values was completed for the rest of the mean desired driver gas pressure regions. As the driver gas pressure increases, the mean PSP becomes closer to the theoretical PSP value. However, the mean PSP value is never closer than 57.8% of the theoretical P4 value and never closer than 61.3% of the theoretical P4@PSP value, represented by Table 1. Moreover, as the driver gas pressure increases, the measured run times become more similar to that predicted by the P4 value rather than that predicted by the P4@PSP value. However, in these plots, the time of separation between the mean DPP and the two theoretical values is indistinguishable. Therefore, a more accurate time separation analysis will be discussed later.

Table 1 PSP Ratio

Driver Gas Pressure (psig)	Mean PSP (psig)	P4 Theoretical PSP (psig)	P4 PSP Ratio (%)	P4@PSP Theoretical PSP (psig)	P4@PSP PSP Ratio (%)
60	0.5	16.8	3.0	10.7	4.7
100	4.9	23.0	21.4	16.9	29.2
157	6.1	29.8	20.5	20.1	30.4
213	14.2	35.0	40.5	28.5	49.7
301	19.1	41.5	46.0	34.9	54.8
408	23.1	47.7	48.3	40.8	56.6
513	30.5	52.8	57.8	49.8	61.3

Additionally, Table 1 shows that a major change in the PSP ratio (mean PSP over theoretical PSP) occurs at a driver gas pressure of ~200 psig, where the P4 PSP ratio jumps from ~20% at a mean driver gas pressure of 157 psig to ~40% at a mean driver gas pressure of 213 psig. A similar jump occurs for the P4@PSP PSP ratio. This change is to be expected, because as explained in Section 3.3, the theoretical model for the RD's opening time suggests that the RD will open too slowly (>0.8 milliseconds) to produce shock waves for driver gas pressures below ~150 psig.

Therefore, in order to gain perspective on how driver gas pressure affects the mean DPP, Figure 28 was created. As a note for the legend, the DP represents the desired driver gas pressure, UD represents the upstream driven gas pressure, and DD represents the downstream driven gas pressure. From Figure 28, one can see that as the driver gas pressure increases the slopes of the first pressure rise of each mean DPP increase as well. Thus, one can see that for desired driver gas pressures above 200 psig, represented with magenta, green, cyan, and black colors, the mean DPP has a first pressure rise slope above 45°. While the mean DPP of desired driver gas pressures below 200 psig have a first pressure rise slope below 45°, colored in red, blue and yellow. Therefore, only the mean DPP of desired driver gas pressures above 200 psig have a first pressure rise slope that semi-resembles the vertical asymptote predicted by ISTT. Additionally, in Figure 28, only for mean DPP of desired driver gas pressures above 200 psig does a constant pressure region seemingly exist. Moreover, Figure 28, illustrates an expected negative gauge pressures for all driver gas pressures, because lower than atmospheric pressures occur following the expansion fans of supersonic flow. Therefore,

there is a phenomenological difference between these two types of mean DPP. From analysing the mean PSP, the mean first pressure rise of the mean DPP, and the prediction from the RD opening time model, one can see that for driver gas pressures below 200 psig, shock waves are not likely to be produced.

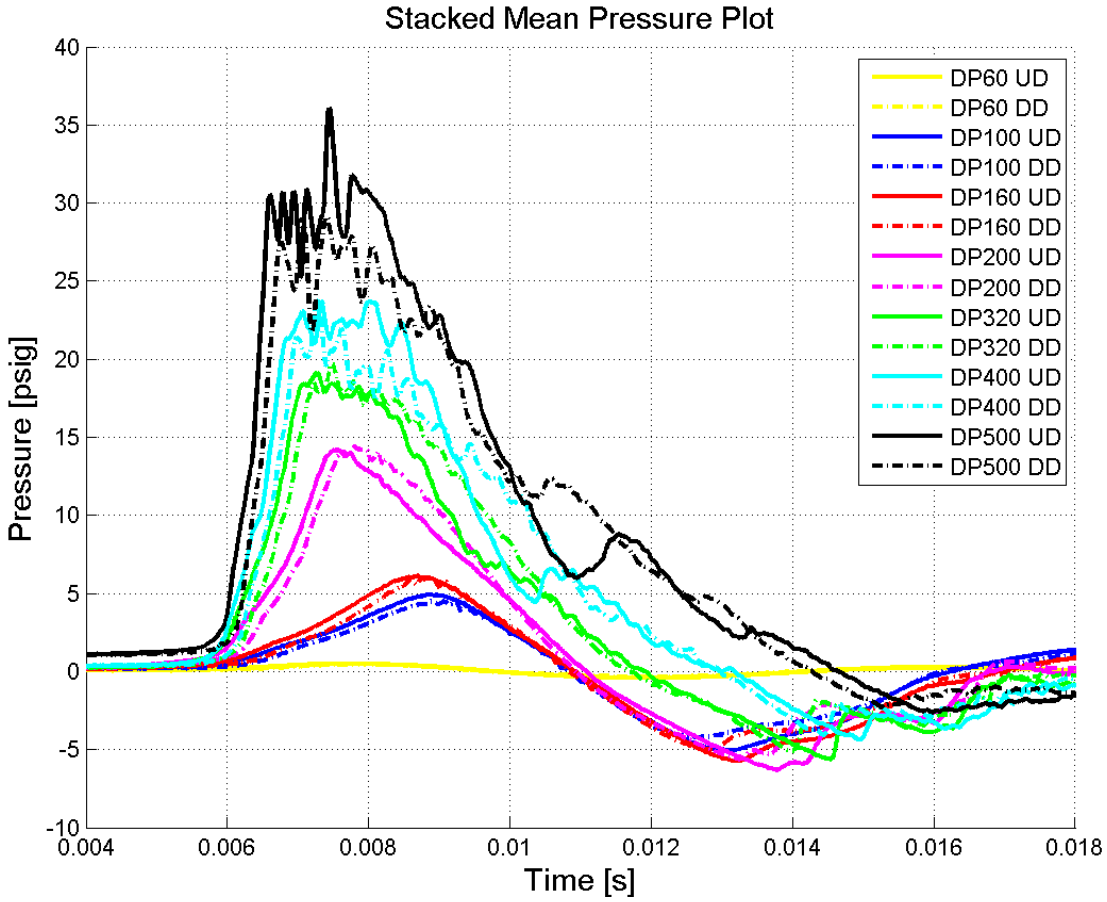

Figure 28 All Mean Pressures

Howerver, the accuracy analysis for the SG is not complete. Earlier in this section it was stated that in order to complete a comprehensive accuracy analysis of the

SG, the calculated shock wave Mach numbers (M_s) must be compared to the M_s predicted by ISTT. As described in Section 5.3.1, the M_s is calculated by taking the time difference (Δt) between the first pressure rise of each driven gas pressure transducer (DnT). Then obtain the velocity by dividing the known DnT separation distatnce (Δx) by the calcuated time difference (Δt). Using the calculated velocity and the thermocouple temperature the M_s is calculated.

Therefore, Figure 29 shows the shock wave Mach number (y-axis) as a function of the driver gas to driven gas pressure ratio or P4/P1 (x-axis). Represented on Figure 29 is the ideal curve predicted by ISTT and is represented by the solid black line. The blue line with markers represents the theoretical M_s based on the mean driver gas pressure (P4). The red line with markers represents the theoretical M_s based on the mean P4@PSP. The magenta line with markers represents the theoretical M_s based on the mean PSP. The green line with markers represents the mean M_s calculated from the unfiltered driven gas pressure data. The yellow line with markers represents the mean M_s calculated from the loess filtered driven gas pressure data. The cyan line with markers represents the mean M_s calculated from the normalized unfiltered driven gas pressure data and the black line with markers represents the mean M_s calculated from the normalized loess filtered driven gas pressure data. The error bars represent the standard deviations of the M_s. The mean shock wave Mach numbers and the standard deviations are calculated by the method described in Section 5.3.2.

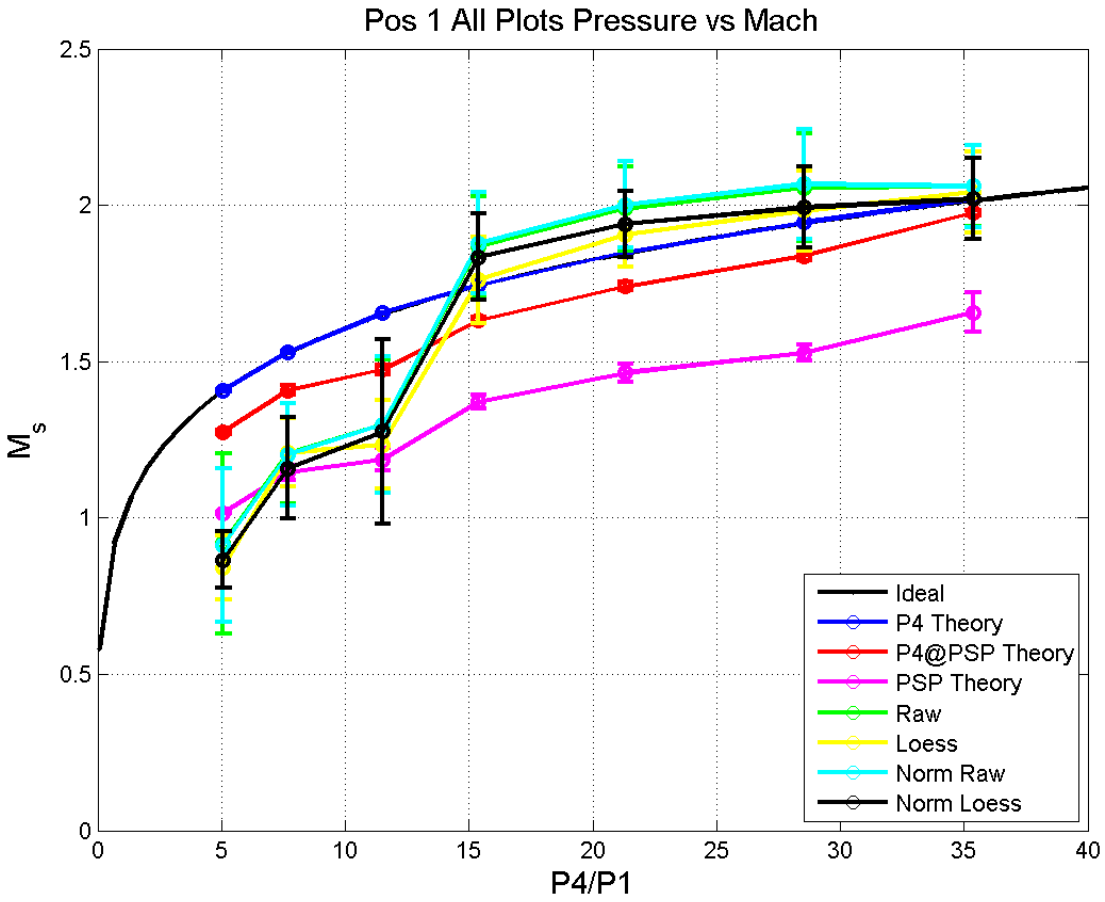

Figure 29 Performance – Threshold 30%-70%

The P4 theory line represents the upper theoretical limit of the obtainable M_s in the SG, because the P4 theory line represents the M_s predicted by ISTT assuming no losses in the system. The P4@PSP Theory line accounts for some losses in the system, by only considering the driver gas pressure after the door is opened. Therefore, the M_s predicted by the P4@PSP Theory line should be the actual upper limit of the SG. Furthermore, as illustrated and discussed previously the mean PSP is always less than

50% of the theoretical PSP, therefore, the PSP theory line should account for the most losses in the system and could represent the lowest obtainable M_s in the SG.

As one can see, in Figure 29, the calculated M_s from the unfiltered, loess filtered, normalized unfiltered, and normalized loess filtered driven gas pressure data line all follow the same trends, which is to be expected. The general trends suggests that an event separates M_s lines into two curves. One general curve follows the PSP theory line and another follows the upper limit predicted by ISTT. Although the lower curve falls below the PSP theory line and the upper curve is always above the upper limit, the error bars for all the lines generally falls inside these limits. Moreover, the P4@PSP theory line seems to be on the edge of most of the error bars, which suggests it may be an impropper theory line to compare too. Therefore, a conclusion cannot be made solely on where the mean path lies with respect to the limiting curves.

The event that separates the M_s lines into two general curves occurs between a mean driver gas pressure of 160 psig to 200 psig, or as represented in Figure 29 a mean driver gas pressure to driven gas pressure ratio (P4/P1 or DDPR) of 11.51 to 15.39. In between these two tested mean driver gas pressure regions the calculated M_s goes from ~25% below to ~1% above that which is M_s predicted by the mean driver gas pressure (P4), as described by the loess filtered driven gas pressure data in Table 2. Therefore, once again, something changes in the SG at a mean driver gas pressure of ~200 psig. Consequently, Figure 29 suggests that for driver gas pressures below 200 psig shock waves are not formed in the test section.

Table 2 shows how each filtering method changes the calculated M_s. It also contains the information in Figure 29. Referring to Figure 29 and Table 2 the loess filtered driven gas pressure data values are consistently the most accurate followed by the unfiltered or raw driven gas pressure data values. As mentioned in Section 5.3, normalizing the driven gas pressure data will probably alter the DPP, which is an undesirable affect, resulting in untrustworthy data. This assumption is now fact because in both Figure 29 and Table 2 the normalized driven gas pressure data differs from the non-normalized driven gas pressure data. Moreover, the normalized driven gas pressure data is less accurate than the non-normalized driven gas pressure data when one looks at the error bars and the mean values. Therefore, the normalized driven gas pressure data values will be ignored for the remainder of this study.

Table 2 shows that the SG increases in accuracy as the driver gas pressure increases, which is to be expected because as mentioned in Section 3.3 the higher the driver gas pressure, the faster the RD will open, resulting in more accurate shock wave Mach numbers. Therefore, Table 2 shows that for driver gas pressures of 200 psig the calculated M_s is less than ~7.2% and ~1.0% of that predicted by ISTT for the raw driven gas pressure data and the loess filtered driven gas pressure data, respectively. Additionally, for driver gas pressures of 500 psig the calculated M_s is less than ~2.1% and ~1.1% of that predicted by ISTT for the raw driven gas pressure data and the loess filtered driven gas pressure data, respectively. Because the purpose of loess filtering the data was to eliminate any extra EMI from the system, as discussed in Section 5.3.1, and

Table 2 proves that it is the most accurate filtering method, thus the loess filtered driven gas pressure data will be used as the accuracy metric for the SG.

Table 2 Results

Driver Pressure	Driver / Driven	Wave Speed (Mach Number)						
P4	P4 / P1	P4	P4 @ PSP	PSP	Raw	Loess Filtered	Normalized Raw	Normalized Loess Filtered
DP60	5.07	1.41	1.27	1.02	0.92	0.84	0.91	0.87
DP100	7.70	1.53	1.41	1.15	1.21	1.21	1.20	1.16
DP160	11.51	1.65	1.47	1.19	1.30	1.23	1.30	1.28
DP200	15.39	1.74	1.63	1.37	1.87	1.76	1.88	1.83
DP300	21.32	1.85	1.74	1.46	1.99	1.91	2.00	1.94
DP400	28.52	1.94	1.84	1.53	2.06	1.98	2.07	1.99
DP500	35.36	2.02	1.98	1.66	2.06	2.04	2.06	2.02
		Error Bars - Standard Deviation						
DP60	5.07	0.00	0.01	0.00	0.29	0.10	0.25	0.09
DP100	7.70	0.00	0.01	0.02	0.16	0.11	0.16	0.16
DP160	11.51	0.00	0.01	0.04	0.21	0.14	0.22	0.30
DP200	15.39	0.00	0.01	0.02	0.16	0.14	0.16	0.14
DP300	21.32	0.00	0.01	0.03	0.13	0.10	0.14	0.11
DP400	28.52	0.00	0.01	0.03	0.17	0.13	0.18	0.13
DP500	35.36	0.00	0.01	0.06	0.13	0.13	0.13	0.13
		Repeatability - Percent Standard Deviation						
DP60	5.07	0.31	0.62	0.24	31.30	12.40	26.90	10.50
DP100	7.70	0.30	1.25	2.10	13.30	8.99	13.60	14.00
DP160	11.51	0.08	1.16	2.95	16.00	11.50	16.80	23.20
DP200	15.39	0.23	0.68	1.63	8.60	7.82	8.65	7.52
DP300	21.32	0.05	0.90	1.94	6.71	5.33	6.85	5.50
DP400	28.52	0.04	0.79	1.67	8.31	6.45	8.52	6.47
DP500	35.36	0.07	0.42	3.84	6.25	6.38	6.36	6.41
		Accuracy - Percent from Ideal Shock Tunnel Theory - P4						
DP60	5.07	0.00	-9.54	-27.86	-34.81	-40.27	-35.27	-38.51
DP100	7.70	0.00	-7.99	-25.19	-21.16	-21.08	-21.37	-24.28
DP160	11.51	0.00	-10.96	-28.28	-21.63	-25.41	-21.54	-22.91
DP200	15.39	0.00	-6.40	-21.33	7.18	1.01	7.74	5.23
DP300	21.32	0.00	-5.85	-20.81	7.57	3.10	8.27	4.89
DP400	28.52	0.00	-5.55	-21.45	5.73	1.97	6.29	2.49
DP500	35.36	0.00	-2.16	-17.93	2.08	1.09	2.04	0.04

		Accuracy - Percent from Ideal Shock Tunnel Theory - P4@PSP						
DP60	5.07	10.55	0.00	-20.25	-27.94	-33.97	-28.45	-32.03
DP100	7.70	8.68	0.00	-18.69	-14.32	-14.23	-14.54	-17.71
DP160	11.51	12.31	0.00	-19.45	-11.99	-16.23	-11.89	-13.42
DP200	15.39	6.84	0.00	-15.95	14.51	7.92	15.10	12.42
DP300	21.32	6.21	0.00	-15.90	14.25	9.51	14.99	11.40
DP400	28.52	5.88	0.00	-16.84	11.95	7.96	12.54	8.51
DP500	35.36	2.21	0.00	-16.11	4.34	3.32	4.29	2.25
		Accuracy - Percent from Ideal Shock Tunnel Theory - PSP						
DP60	5.07	38.61	25.39	0.00	-9.64	-17.20	-10.28	-14.77
DP100	7.70	33.67	22.99	0.00	5.38	5.49	5.11	1.21
DP160	11.51	39.43	24.15	0.00	9.27	4.00	9.39	7.48
DP200	15.39	27.12	18.98	0.00	36.25	28.40	36.95	33.76
DP300	21.32	26.29	18.90	0.00	35.85	30.21	36.73	32.46
DP400	28.52	27.31	20.24	0.00	34.61	29.82	35.32	30.48
DP500	35.36	21.84	19.21	0.00	24.38	23.17	24.33	21.89

Therefore, from the complete accuacy analysis of the SG it appears that form analysing the post shock wave gas pressure (PSP) (<57.8% of ISTT), the driven gas pressure profiles (DPP), and the calculated shock wave Mach numbers (<3.1% of ISTT), shock waves are suggested to be present inside the test section only for driver gas pressures above 200 psig.

Moreover, the pressure threshold parameter method for obtaining the shock wave Mach numbers explained in Section 5.3.1 was tested to see how different values of the pressure threshold parameter would change the results. It was found that the pressure threshold parameter produces accurate shock wave Mach numbers regardless of its values. Further explaination can be found in Appendix E.

6.2. Repeatability

The repeatability of the Shock Generator (SG) is calculated as the percent standard deviation of the calculated shock wave Mach number (M_s). Therfore, all of the driven gas pressure profiles (DPP) for a desired driver gas pressure region will appear to be more similar the higher the repeatability becomes. Therefore, a higher repeatability has smaller percent standard deviations. Because it can be confusing to refer to a parameter as having a high repeatability but give it a low numeric value, the term repeatability varience will be used. The repeatability variance describes the run to run changes of the parameter and is calculated by the percent standard deviation.

From Table 2 the repeatability of the SG seems to increase as the driver gas pressure increases. However, at a driver gas pressure of 200 psig the repeatability appears to become independent of the driver gas pressure. Therefore, from the accuracy analysis in the previous section, the calculated M_s has a repeatability variance that is less than 7.9% for the loess filtered driven gas pressure data.

However, the repeatability of the SG can also be described by the the run to run variance or jitter of the driven gas pressure profile (DPP). Therefore, the DPP should be plotted ontop of each other such that a visual interpretation can be established. Figure 30 provides this information. A description of the manner used to create Figure 30 is in Section 5.3.3.

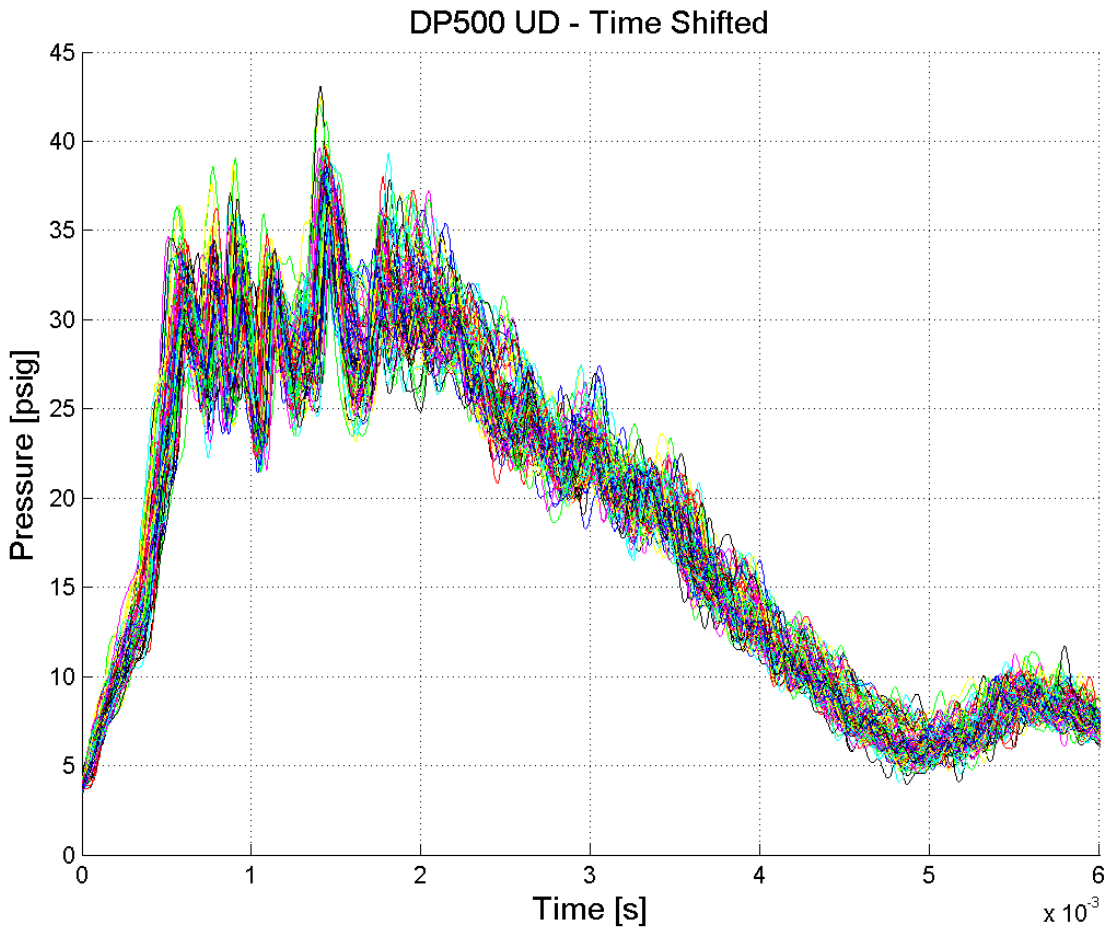

Figure 30 500 psig Time Shifted Upstream Driven Transducer Jitter

From Figure 30, one can ascertain that an estimate variance for the DPP would be the width of time, about half way along the first pressure rise. Thus, for Figure 30, the estimated repeatability variance would be ~0.25 milliseconds. Additionally, to represent the SG's degree of repeatability, Figure 31 illustrates the same plot as Figure 30, but for a driver gas pressure of 100 psig, where it appears that the first pressure rise slopes of the DPP are much shallower and further spread apart than those in Figure 30. The estimated repeatability variance for the DPP from a driver gas pressure of 100 psig is ~2

milliseconds. Therefore, there is a two order of magnitude difference in the estimated repeatability variance between a driver gas pressure of 100 psig and 500 psig. Thus, the same process for obtaining an estimated repeatability variance was completed for every driver gas pressure region.

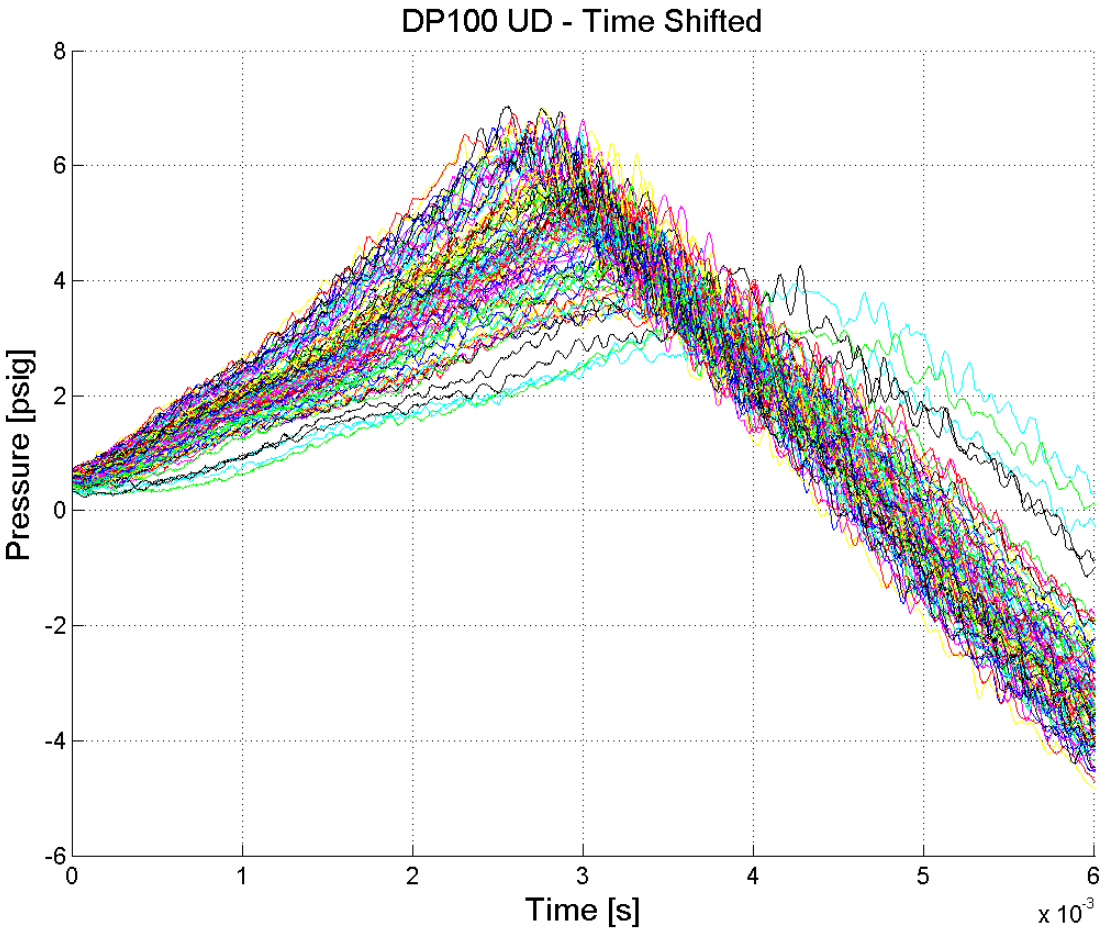

Figure 31 Time Shifted Pressure Profiles – 100 psig

From analyzing the estimated repeatability variance a trend appears, where for driver gas pressures below 200 psig, the DPP' first pressure rise slope was so shallow and scattered that an estimate became difficult to determine. Conversely, for driver gas pressures above 200 psig, the DPP' first pressure rise slope allowed for an easy estimate of the repeatability variance to be obtained. As the driver gas pressure increased from 200 psig, the estimated repeatability variance decreased from 1 millisecond in increments of a 0.25 milliseconds for every 100 psig driver gas pressure. Therefore, it appears that the SG is only repeatable for driver gas pressures above 200 psig.

Additionally, in Figure 30, one can see that the repeatability of the first pressure rise extends throughout the constant pressure region but not during the onset of the expansion fans. As a result, we can analyze the mean oscillations in the constant pressure region. From Figure 27, we can now see that oscillations in the measured mean DPP' constant pressure region are flow field induced, thus they are not mechanical oscillations from wall vibrations. This is evident by time shifting the two DPP such that their first pressure rises are aligned with each other. From this, we see that numerous peaks and valleys align with each other, indicating that the oscillations of the measured DPP are traveling at the flow velocity. If these oscillations were a result of wall vibrations then the oscillations of the measured mean DPP constant pressure region would be synchronized together when the DPP are separated, because vibrations through metal travel at a much faster velocity than vibrations through air.

Therefore, the repeatability of the M_s repeatability variance is < 7.9% as listed in Table 2 and the repeatability variance of the DPP' first pressure rise slope is < 1

millisecond. Moreover, the Shock Generator (SG) is only repeatable for driver gas pressures above 200 psig.

6.3. Shock Wave Mach Number Range

The shock wave Mach number range is determined by the difference between the largest and smallest M_s obtainable for the Shock Generator (SG). As stated in the accuracy analysis and the repeatability analysis the SG seems to suggest that shock waves could be produced in the test section for driver gas pressures above 200 psig. Therefore, the minimum obtainable M_s in the SG is the M_s calculated from a driver gas pressure of 200 psig, which is tabulated in Table 2 as $M_s = 1.76$. Furthermore, the maximum obtainable M_s in the SG is the M_s calculated from the highest tested driver gas pressure, which is at of 500 psig. Therefore, as tabulated in Table 2 as maximum $M_s = 2.04$. Thus, the shock wave Mach number range for the Shock Generator is $1.76 < M_s < 2.04$ as tabulated in Table 2 for the loess filtered driven gas pressure data.

6.4. The Shock Wave Formation Distance

The shock wave formation distance is measured by moving the driven gas pressure transducers (DnT or KPT) to various locations downstream of the driver section until the obtained driven gas pressure profiles indicate that a shock wave is present in between the two DnT by the methods decribed in the previous sections. However, a rigerous shock wave formation distance analysis was not conducted for the SG. Therefore, only a subjective shock wave formation distance analysis can be completed. From the RD's theoretical opening time model, the accuracy analysis, and the

repeatability analysis, only driver gas pressures above 200 psig may form shock waves in between the DnT. Therefore, the shock wave formation distance of the SG is ~8.7 test section heights.

7. CONCLUSIONS AND RECOMMENDATIONS

7.1. Conclusions

The feasibility and characterization of a novel diaphragmless shock tube was examined at the National Aerothermochemistry Laboratory at Texas A&M University. The goal was to design a facility that reliably and repeatedly produces strong (M_s ~ 1.0-2.0) shock waves in air without the drawbacks of traditional shock tubes. The device is modular, automated, and compact. The new low-duty-cycle diaphragmless shock tube uses a rotating door and locking cam-shaft mechanism to generate shock waves. This facility produced the desired driver gas pressure repeatable to within 0.31% at low-duty-cycle of 6 seconds. The driven gas pressure profiles within the test-section suggest that the shock wave formation process may have begun within test section for a driver gas pressure of 200 psig and above. Therefore, the performance metrics indicate the following:

1. Accuracy
    a. Wave Speed
        i. < 3.1% from P4 ideal shock tube theory
        ii. < 9.51% from P4@PSP ideal shock tube theory
    b. Post shock wave gas pressure
        i. < 57.8% of P4 ideal shock tube theory
        ii. < 61.3% of P4@PSP ideal shock tube theory
2. Repeatability Variance

a. Shock wave Mach number - < 7.9%

b. Post shock wave gas pressure - < 1 milliseconds

3. Shock wave Mach number range – $1.76 < M_s < 2.04$ (Upper limit is set by the highest tested driver gas pressure)

Therefore, the present concept is a viable low-duty-cycle (6 seconds) repeatable shock tube. Table 3 compares the present concept's performance to the other diaphragmless shock tube designs described in the Background Review. As indicated, the present performance is comparable. However, additional studies are required, as described in the next section.

Table 3 Repeatable Shock Tube Performance Comparison

Repeatable Shock Tube Performance Comparison				
Shock Wave Generating Device	**Accuracy to ISTT**	**Repeatability**	**"Shock Wave" Mach Number Range**	**Shock Wave Formation Distance (Test Section Diameters or Heights)**
Diaphragm	High	Low	< 3 < 5 with He	Short
Piston - Kosig et al.	1% to 9%		1.1 to 2.0 < 5 with He	20 - 40
Piston - Rego et al.	20% to 38%		2.0 to 5.0 with He	
Spring-loaded Piston - Kashitani et al.	11% to 30%	< 1%	1.2 to 2.1	20 - 100
Flexible Membrane - Hosseini et al.	3.3 % to 5% with Air and < 1% with He	0.20%	1.15 to 1.35 1.1 to 1.7 with He	
Shock Generator	**1.0% to 3.1%**	**< 7.9%**	**1.76 to 2.04**	

Assume air as the driver section and driven section gas unless otherwise stated.

7.2. Future Work and Lessons Learned

Although a great deal has been accomplished in producing the repeatable low-duty-cycle diaphragmless shock tube at Texas A&M University known as the Shock Generator, there is still much more that can be done. The following are four tasks that need to be completed in order to fully characterize the facility:

1. Obtain schlieren images of the flow field
2. Find the upper limit of the current O-ring and seal design
3. Obtain additional instrumentation for the facility
4. Correct the driver section to driven section area ratio

7.2.1. Schlieren Images

Conduct a statistical based parametric study of the flow field inside the test section by obtaining numerous schlieren images and changing various parameters:

- Driver gas pressure
- Test section location – I caution against physically moving the test sections because doing so would result in difficulties comparing results from one location to the next because there is no way to disassemble and reassemble the sections exactly the same way every time, where the flow path junctions between the sections could have different steps and gaps. Therefore, I suggest making multiple test sections that replace the driven sections. Furthermore, making a longer test section would be ideal.

- Time after the rotating door is fully opened – by using a time delay device one could trigger off the upstream driven gas pressure transducer and collect time accurate statistical measurements of the flow field.

Conducting this study could resolve several currently unanswered questions.

- What driver gas pressures form shock waves and which ones form compression regions?
- What is the shock wave formation distance?
- What is the boundary layer structure?
- What flow field characteristics cause the discrepancy between the theoretical and measured post shock wave gas pressure in the test section?
- Is the shock wave planar and is the flow two-dimensional? – This can only be answered by conducting both top down and side schlieren through all four windows in the test section.

Appendix F describes the previously attempted schlieren setup.

7.2.2. O-ring and Seal Upper Limit

Find the upper limit of the current O-ring and seal design by increasing the driver gas pressure until the seal fails. However, once the seal fails, replacement of the O-ring with a new one of the same type must occur. With the new O-ring the driver gas pressure should be set to a known working pressure (500 psig) as a benchmark to ensure the new O-ring is installed properly before moving up to a higher driver gas pressure.

7.2.3. Obtain Additional Instrumentation

As described, the facility has one slow-response driver gas pressure transducer, and two fast-response driven gas pressure transducers. However, I propose that the facility should have several fast-response pressure transducers for both the driver section and driven section. The proposed transducers are:

1. Driver Section
    a. One Kulite or Endevco, AC&DC coupled (psia), pressure transducer built in the form of a centerline pitot probe. The centerline pitot probe measurements are more accurate than flush-mounded wall measurements thus; a better understanding of how the driver gas responds to the opening of the rotating door can be obtained.
    b. Three PCB, AC component, time of arrival transducers at various locations, thus enabling expansion fan speed calculations:
        i. Two flush-mounted to the celling of the driver section
        ii. One flush-mounted to the driver section filling flange
2. Driven Section
    a. One Kulite or Endevco, AC&DC coupled (psia) pressure transducer built in the form of a centerline pitot probe. The pitot probe should be downstream such that it does not interfere with other measurements. This gas pressure transducer will measure the centerline driven gas pressure.

b. Two Kulite or Endevco, AC&DC coupled (psia), flush mounted pressure transducers, one on the ceiling and another in a wall. They should be at the same location downstream of the driver section to facilitate the measurement of flow dimensionality.

c. Three Kulite or Endevco, AC&DC coupled (psia), flush-mounted pressure transducers, placed along the ceiling centerline at different locations downstream of the driver section. This enables the characterization of driven gas pressure as a function of downstream distance.

d. Four PCB, AC component, time of arrival transducers that are placed at varying locations downstream of the driver section. AC component pressure transducers only capture the fluctuating pressures profiles, thus they cannot indicate pressure values. They also have nanosecond rise times and are perfect for time of arrival sensors, which would increase the accuracy of the wave speed calculations.

Additionally, I propose that the actuation section have additional instrumentation to analyze how fast the rotating door opens.

1. Two limit switches surrounding the rotating door. One limit switch will indicate when the rotating door is no longer closed and the other will indicate when it is open. This in conjunction with the servomotor odometry information will give a great understanding of the timing of the rotating door and locking cam-shaft valve mechanism during each cycle.

2. A high-speed camera should view the rotating door through the driven sections similar to the diaphragm opening time experiments conducted by the reference [11], [16], and [17].

7.2.4. Correct Driver Section to Driven Section Area Ratio

Correct the expanding area ratio between the driver section and the driven section by two methods:

1. The quick fix would be to manufacture a plate that would extend from the actuation section outlet flange to the muffler. This plate would run along the floor of the driven sections and test section. Therefore, the plate height would simply that which would create the desired driver section to driven section area ratio.
2. The better fix would be to build either a new driver section or a new driven section.
    a. If the driven section is redesigned, realize that the smaller the driven section height becomes the more dominant boundary layer interference and viscous effects become. Additionally, fully developed flow is more likely.
    b. If the driver section is redesigned then the actuation section and rotating door must be redesigned as well. The initial design of the rotating door used a short rotating door height to optimize rotating door opening time. Moreover, because a seal had to be placed inside the edges of the rotating door and structural considerations had to be

made, the cross sectional area of the flow path through the support piece became smaller than the cross sectional area of the driver section. Although redesigning all these pieces is more time consuming, it is the better approach in order to avoid boundary layer interference and viscous effects.

REFERENCES

[1] Kashitani, M., Yamaguchi, Y., Oki, G., Kitano, H., Esashi, S., "Preliminary Study on Diaphragmless Shock Tube for Transonic Airfoil Testing with PDI," *AIAA*, AIAA 2010-744, Orlando, Florida, 2010, pp. 4-7.

[2] Rêgo, I. Da. S., Miyoshi, Y., Ando, T., Goto, K., Misumi, K., Miyazaki, T., Nishiyori, S., Sato, K. N., Sakamoto, M., Kawashaki, S., Triam Team, "Development of a Large Diameter Diaphragmless Shock Tube for Use in Gas-Dynamic Laser Experiments," *Engineering Sciences Reports*, Vol. 29, No. 2, Kyushu University, Japan, 2007, pp. 283-288.
DOI: AA1147319X

[3] Tranter, R. S., Giri, B. R., "A Diaphragmless Shock Tube for High Temperature Kinetic Studies," *Review of Scientific Instruments*, Vol. 79, Issue 9, 2008.
DOI: 10.1063/1.2976671

[4] Anderson Jr., J. D., "Modern Compressible Flow – with Historical Perspective," 3rd Ed., McGraw-Hill, 2004, Illinois, Ch. 7., pp.263-300.

[5] "Shock Tube," *Wikipedia: the free encyclopedia*, Wikimedia Foundation, Inc., URL: http://en.wikipedia.org/wiki/Shock_tube [cited April 24, 2012].

[6] Takano, Y., Akamatsu, T., "A Diaphragmless Shock Tube," *J. Physics E: Scientific Instruments*, Vol. 17, Issue 8, 1984, pp. 644-646.
DOI: 10.1088/0022-3735/17/8/005

[7] Srulijes, J., Hruschka, R., Seiler, F., Sauerwein, B., "Shock Tube Experiments on Heat Transfer at Generic Re-Entry Bodies," *28th International Symposium on Shock Waves*, edited by K. Kontis, Vol. 1, Springer, New York, 2012, pp. 713-719.

[8] Jourdan, G., Houas, L., Schwaederlé, L., Layes, G., Carrey, R., Diaz, F., "A New Variable Inclination Shock Tube for Multiple Investigations," *Shock Waves*, Vol. 13, 2004, pp. 501-504.
DOI: 10.1007/s00193-004-0232-7

[9] Han, Z. Y., Wang, Z. Q., Yin, X. Z., Yao, J. C., Du, A. D., Wang, K., "A Method for Performing Oblique Shock-Bow Shock Interaction in Double Driver Shock Tube(Tunnel)," *Shock Waves and Shock Tubes*, edited by D. Bershader and R. Hanson, Stanford University Press, Berkeley, California, 1985, pp. 533-540.

[10] Numata, D., Ohtani, K., Takayama, K., "Diffuse Holographic Interferometric Observation of Shock Wave Reflection from a Skewed Wedge," *Shock Waves*, Vol. 19, 2009, pp. 103-112.
DOI: 10.1007/s00193-009-0204-z

[11] Rothkopf, E. M., Low, W., "Diaphragm Opening Process in Shock Tubes," *The Physics of Fluids*, Vol. 17, 1973, pp. 1169-1173.
DOI: 10.1063/1.1694860

[12] Kosing, O. E., Barbosa, F. J., Skews, B. W., "A New, Friction Controlled, Piston Actuated Diaphragmless Shock Tube Driver," *Shock Waves*, Vol. 9, Shock Waves, 1999, pp. 69-72.
DOI: 10.1007/s001930050140

[13] Rêgo, I. Da S., Sato, K. N., Miyoshi, Y., Ando, T., Goto, K., Sakamoto, M., Kawashaki, S., Triam Team, "A Newly Developed Large Diameter Diaphragmless Shock Tube for Studies on CO2-N2 Gas-Dynamic Laser," *Plasma and Fusion Research: Rapid Communications*, Vol. 2, 2007, pp. 33-34.
DOI: 10.1585/pfr.2.033

[14] Hosseini, S. H. R., Onodera, O., Takayama, K., "Characteristics of an Annular Vertical Diaphragmless Shock Tube," *Shock Waves*, Vol. 10, 2000, pp. 151-158.
DOI: 10.1007/s001930050001

[15] Mizoguchi, M., Shigeru, A., "The Effect of Diaphragm Opening Time on the Feasibility of Tuned Operation in Free Piston Shock Tunnels," *Shock Waves*, Vol. 19, 2009, pp. 337-347.
DOI: 10.1007/s00193-009-0214-x

[16] Gaetani, P., Guardone, A., Persico, G. "Shock Tube Flows Past Partially Opened Diaphragms," *Journal of Fluid Mechanics*, Vol. 602, 2008, pp. 267-286.
DOI: 10.1017/S0022112008000815

[17] "Shore Durometer," *Wikipedia: the free encyclopedia*, Wikimedia Foundation, Inc., URL: http://en.wikipedia.org/wiki/Shore_durometer [cited April 16, 2012].

[18] Alpher, R. A., White, D. R., "Flow in Shock Tubes with Area Change at the Siaphragm Section," *Journal of Fluid Mechanics*, Vol. 5, Issue 5, 1958, pp. 457-470.
DOI: 10.1017/S0022112058000124

APPENDIX A

Mean Driver Gas Pressure (psig): 60.44 – Standard Deviation – 0.9205

Upstream Driven Transducer – Mean Temperature (K): 299.9 – Stan. Dev.: 0.57308

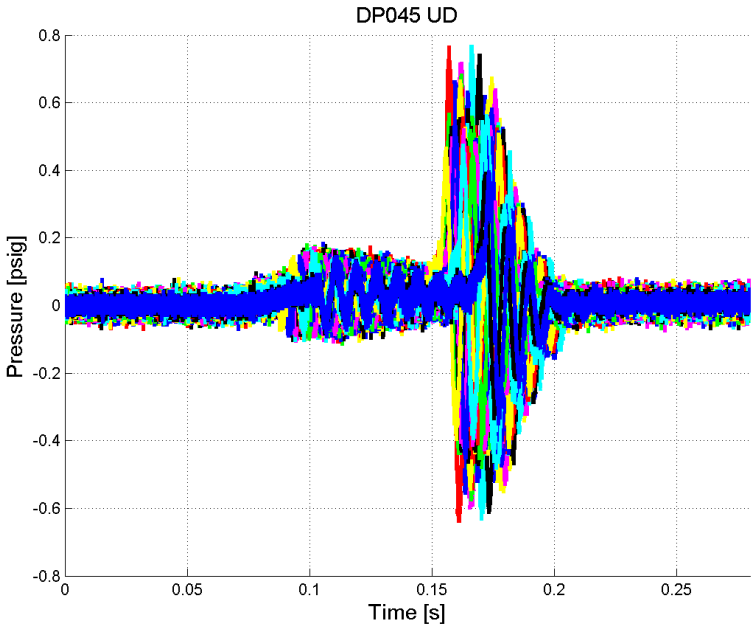

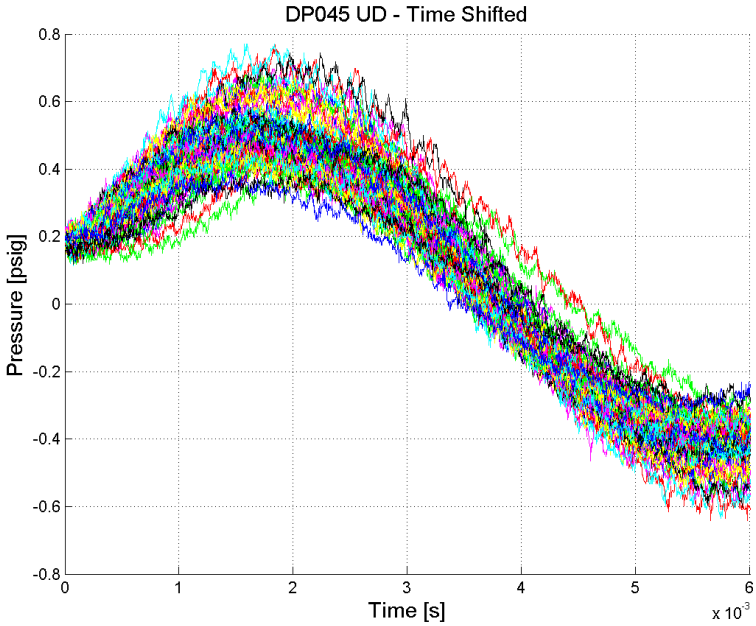

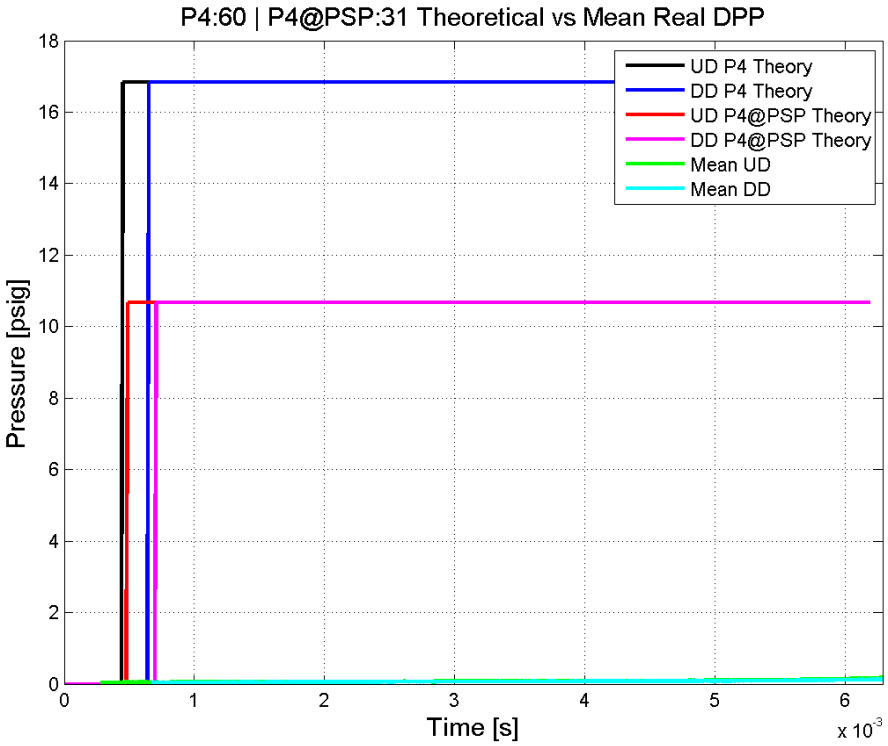
P4:60 | P4@PSP:31 Theoretical vs Mean Real DPP
UD P4 Theory
DD P4 Theory
UD P4@PSP Theory
DD P4@PSP Theory
Mean UD
Mean DD
Pressure [psig]
Time [s]
x 10^-3

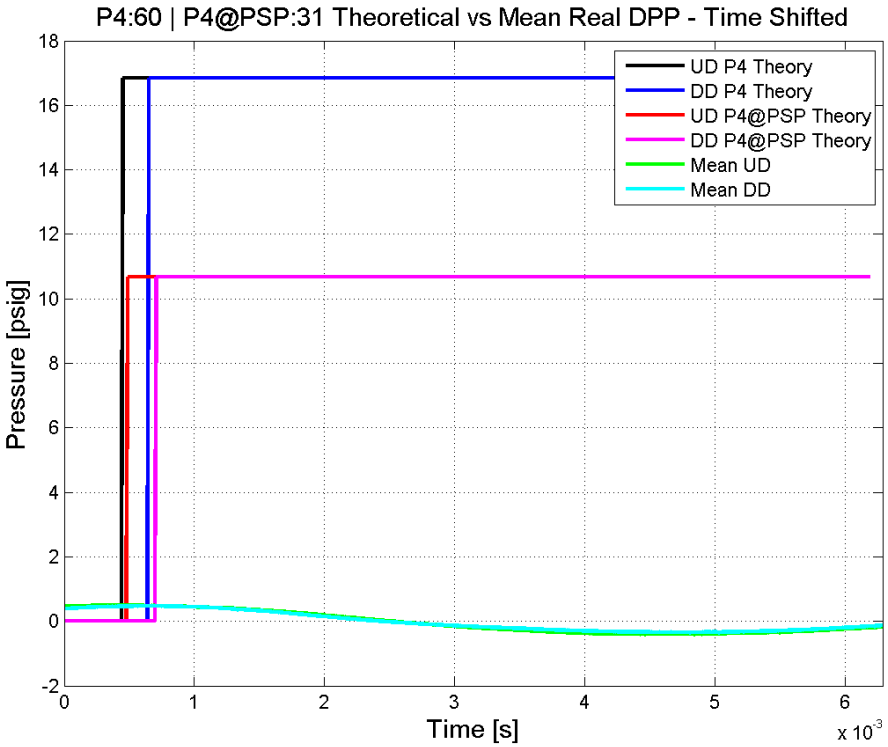
P4:60 | P4@PSP:31 Theoretical vs Mean Real DPP - Time Shifted
UD P4 Theory
DD P4 Theory
UD P4@PSP Theory
DD P4@PSP Theory
Mean UD
Mean DD
Pressure [psig]
Time [s]
x 10^-3

Mean Driver Gas Pressure (psig): 99.78 – Stan. Dev.: 1.4956

Upstream Driven Transducer – Mean Temperature (K): 298.2 – Stan. Dev.: 0.46356

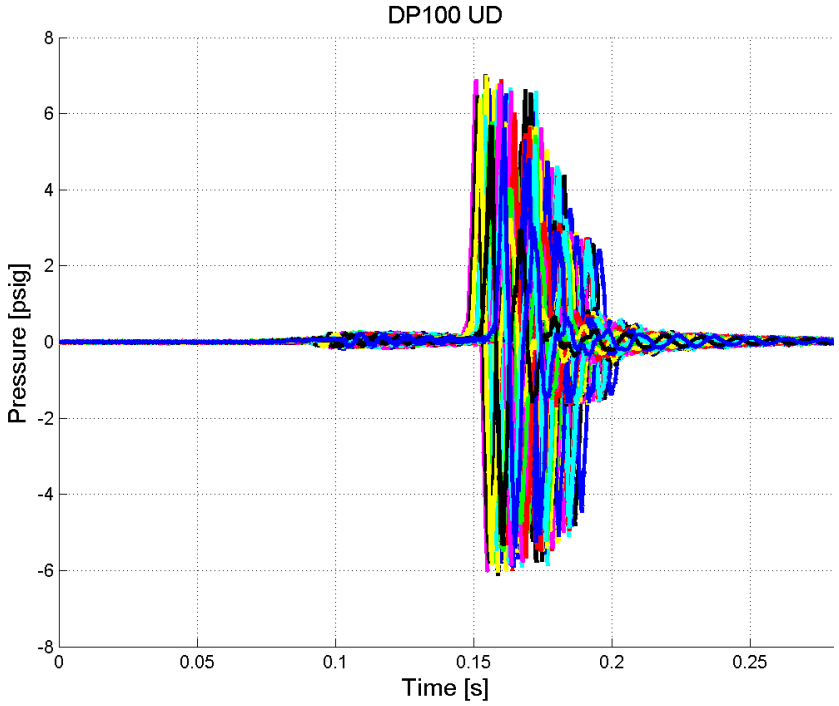

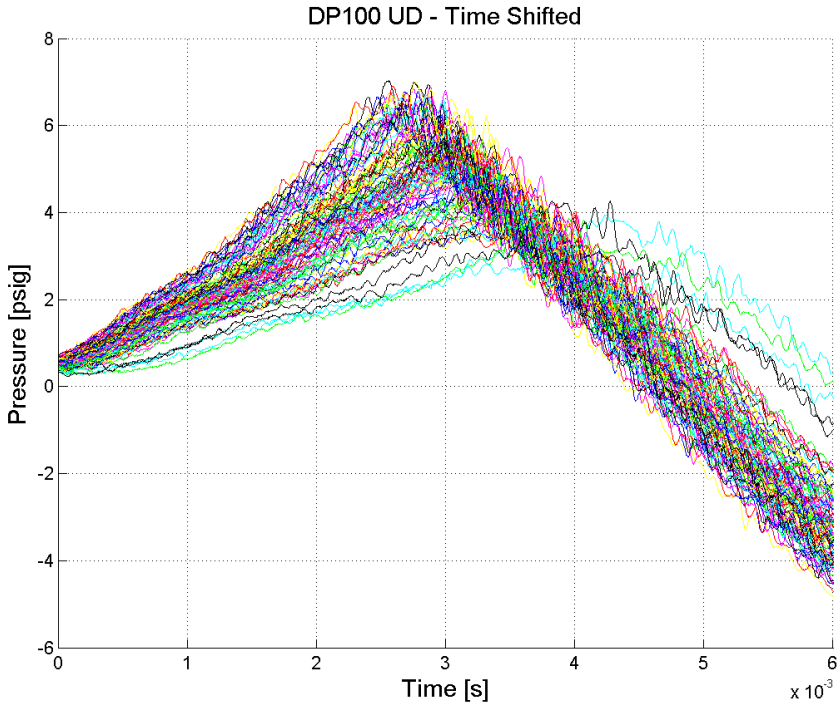

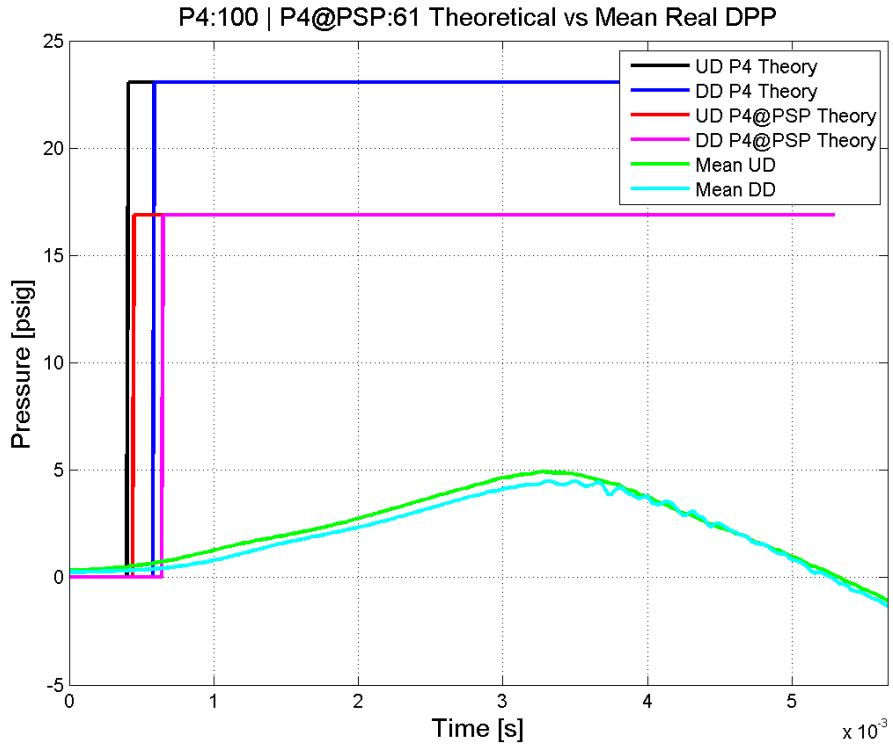
P4:100 | P4@PSP:61 Theoretical vs Mean Real DPP
UD P4 Theory
DD P4 Theory
UD P4@PSP Theory
DD P4@PSP Theory
Mean UD
Mean DD
Pressure [psig]
Time [s]
x 10^-3

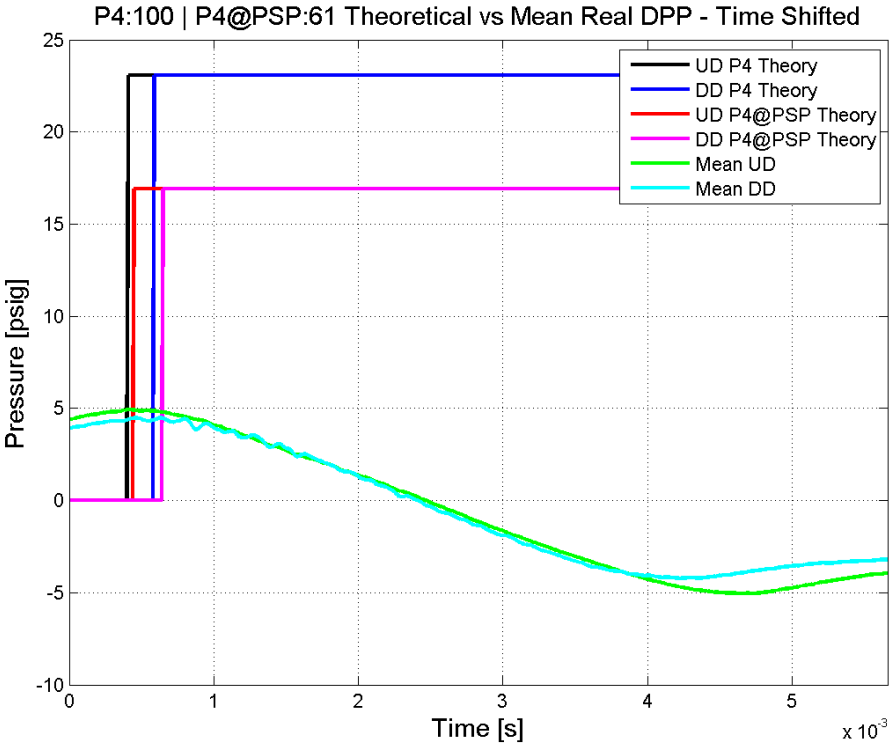
P4:100 | P4@PSP:61 Theoretical vs Mean Real DPP - Time Shifted
UD P4 Theory
DD P4 Theory
UD P4@PSP Theory
DD P4@PSP Theory
Mean UD
Mean DD
Pressure [psig]
Time [s]
x 10^-3

Mean Driver Gas Pressure (psig): 157.11 – Stan. Dev.: 0.68295

Upstream Driven Transducer – Mean Temperature (K): 289.1 – Stan. Dev.: 0.17586

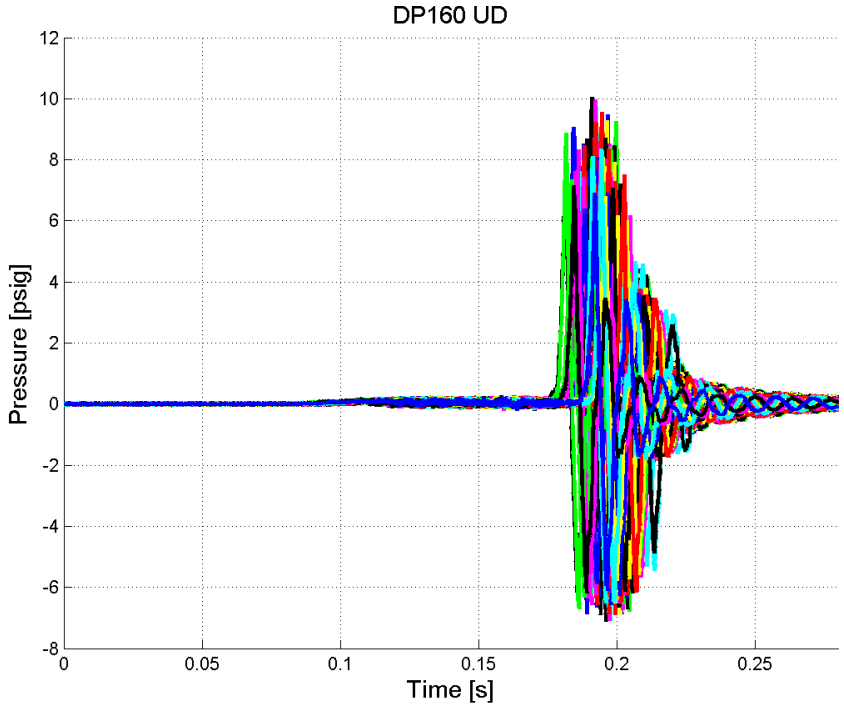

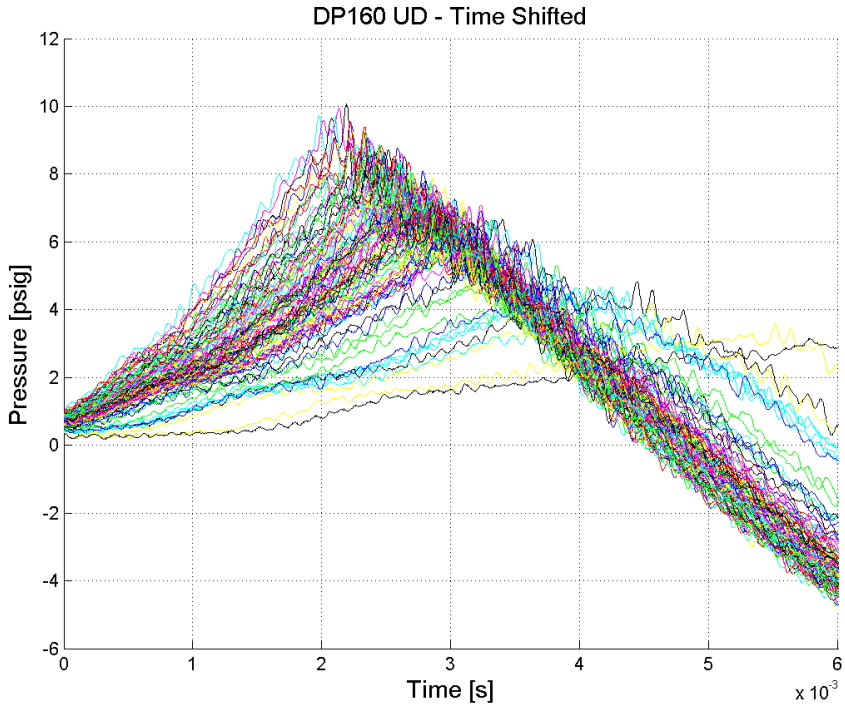

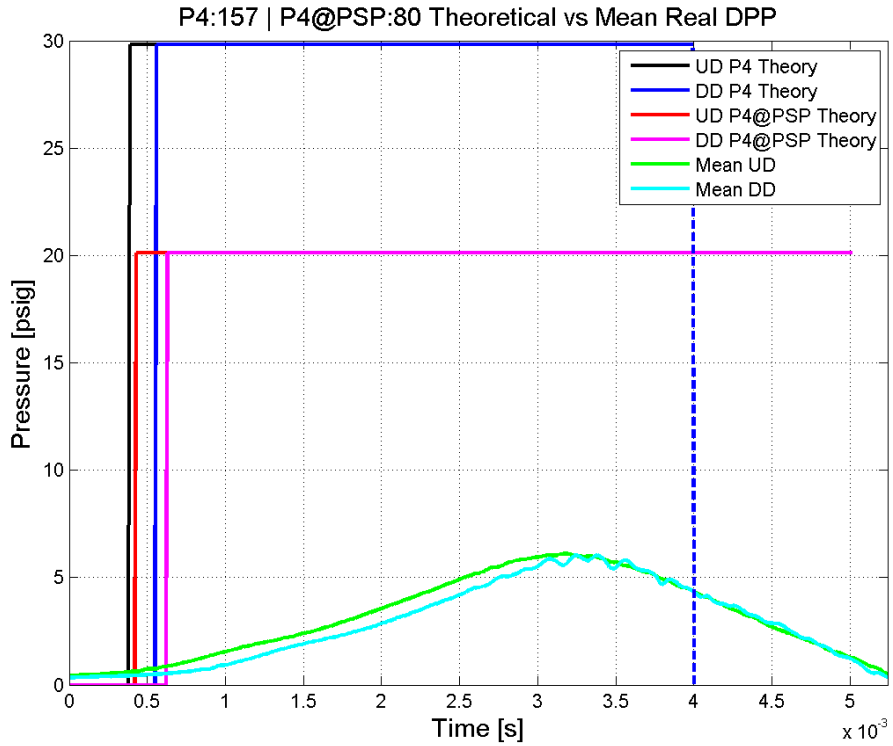
P4:157 | P4@PSP:80 Theoretical vs Mean Real DPP
UD P4 Theory
DD P4 Theory
UD P4@PSP Theory
DD P4@PSP Theory
Mean UD
Mean DD
Pressure [psig]
Time [s]
x 10^-3

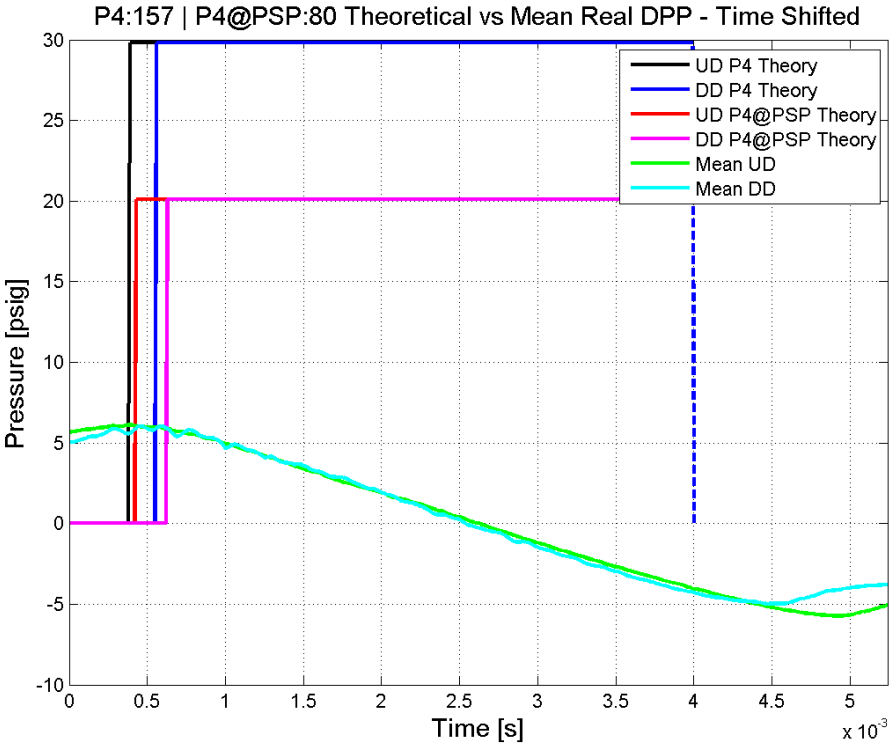
P4:157 | P4@PSP:80 Theoretical vs Mean Real DPP - Time Shifted
UD P4 Theory
DD P4 Theory
UD P4@PSP Theory
DD P4@PSP Theory
Mean UD
Mean DD
Pressure [psig]
Time [s]
x 10^-3

Mean Driver Gas Pressure (psig): 212.78 – Standard Deviation: 2.6858

Upstream Driven Transducer – Mean Temperature (K): 291.1 – Stan. Dev.: 3.2271

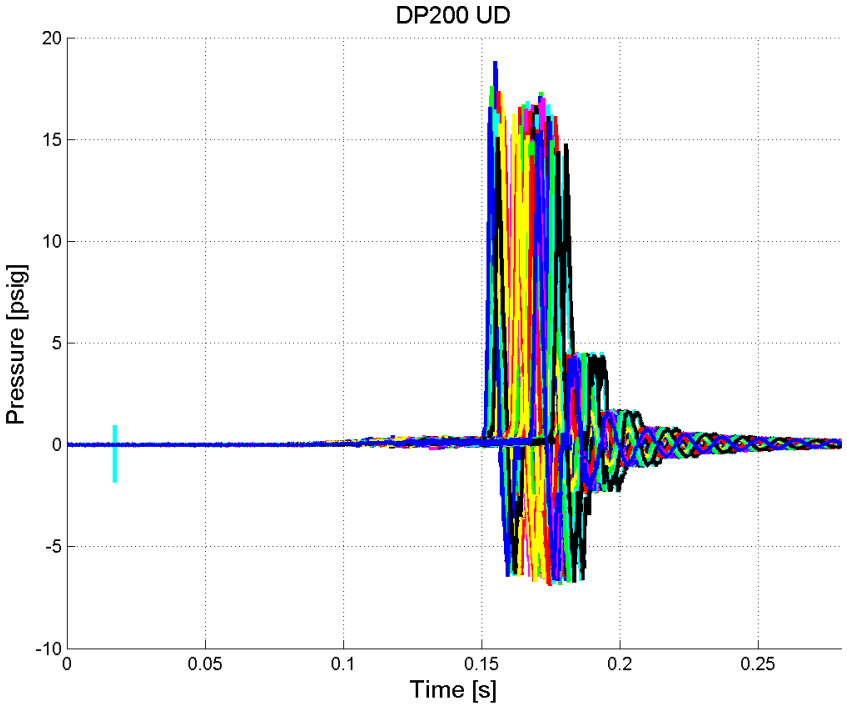

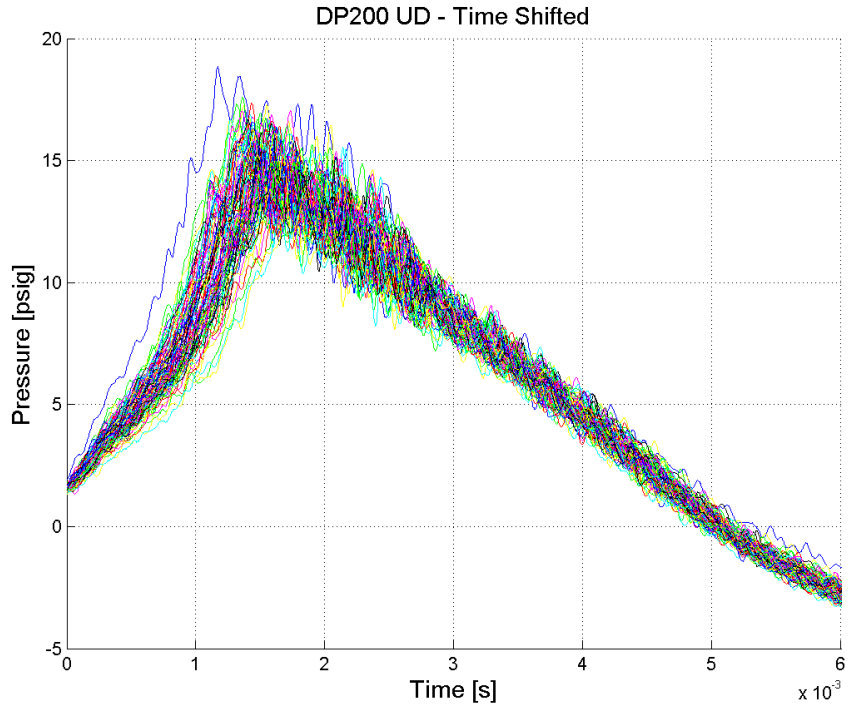

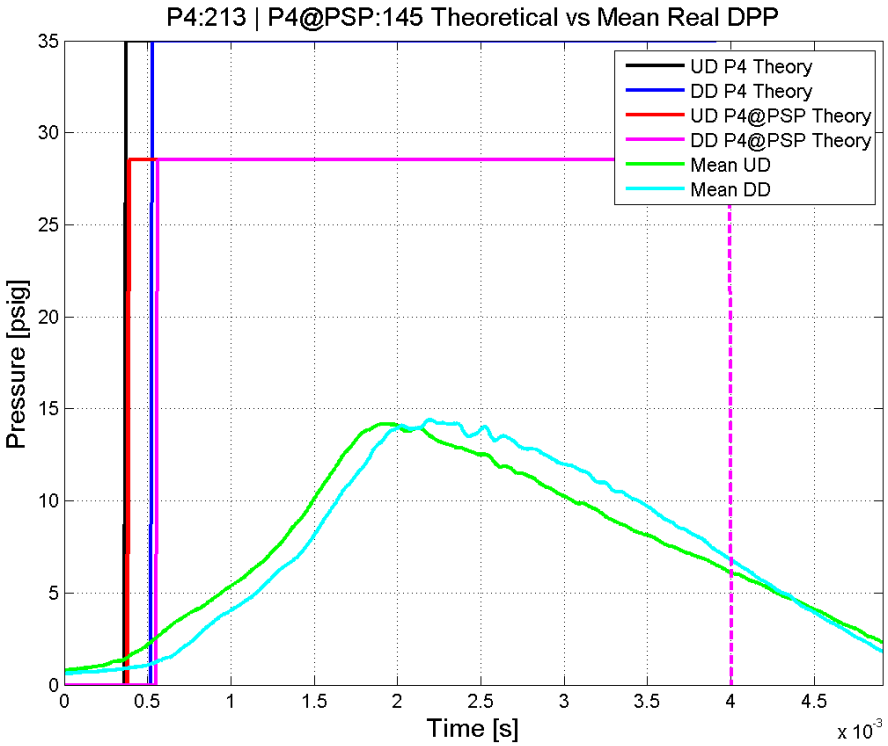
P4:213 | P4@PSP:145 Theoretical vs Mean Real DPP
UD P4 Theory
DD P4 Theory
UD P4@PSP Theory
DD P4@PSP Theory
Mean UD
Mean DD
Pressure [psig]
Time [s]
x 10^-3

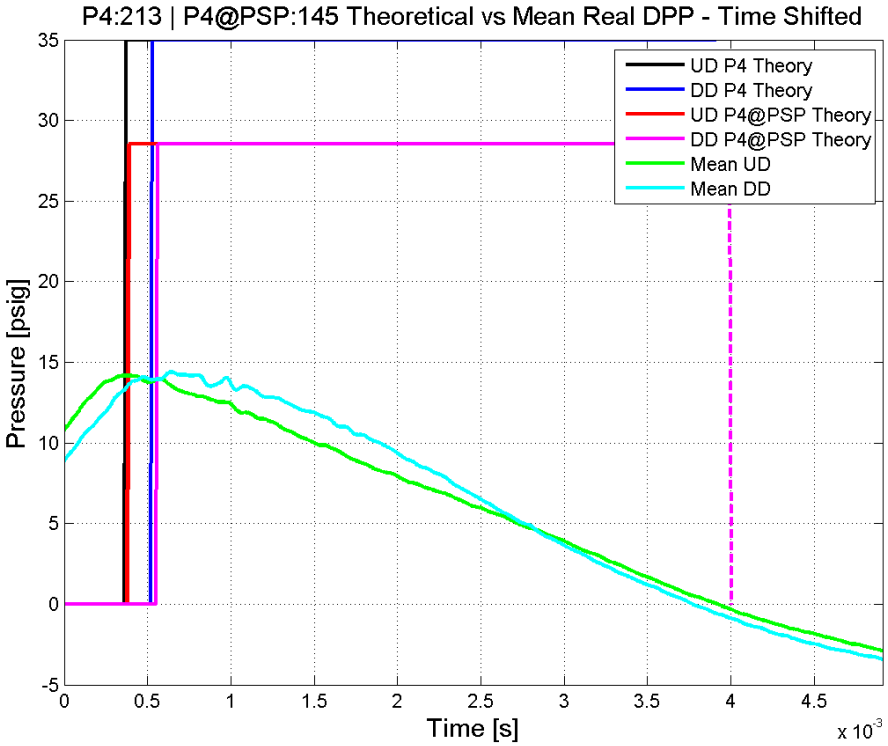
P4:213 | P4@PSP:145 Theoretical vs Mean Real DPP - Time Shifted
UD P4 Theory
DD P4 Theory
UD P4@PSP Theory
DD P4@PSP Theory
Mean UD
Mean DD
Pressure [psig]
Time [s]
x 10^-3

Mean Driver Gas Pressure (psig): 300.84 – Standard Deviation: 0.88851

Upstream Driven Transducer – Mean Temperature (K): 286.3– Stan. Dev.: 1.1309

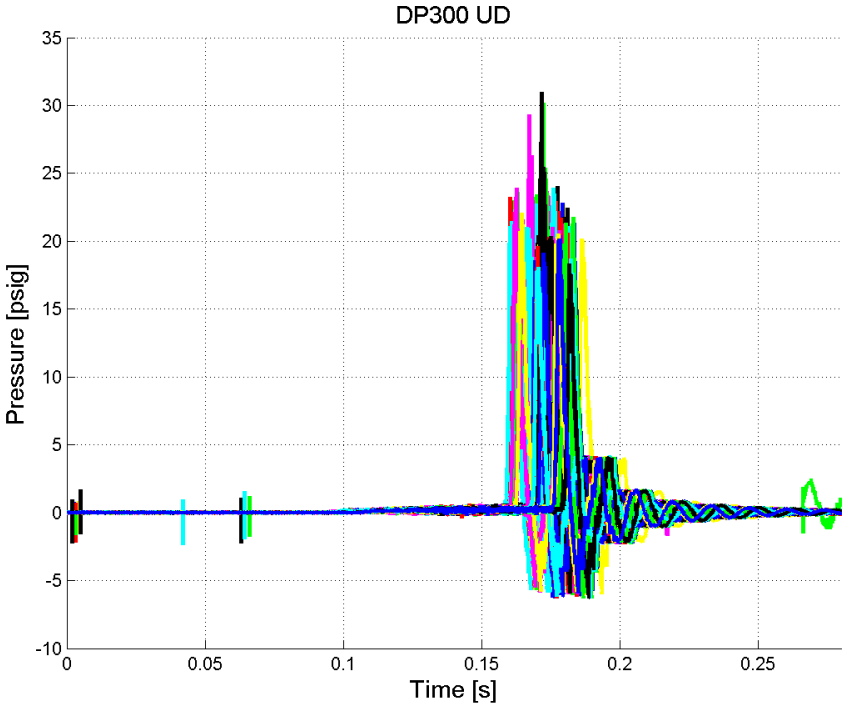

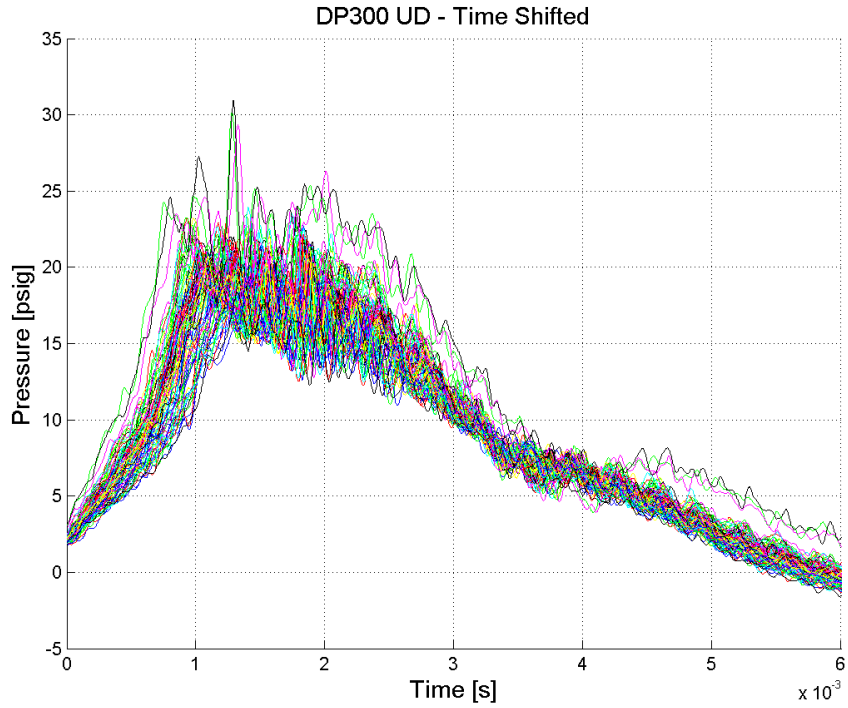

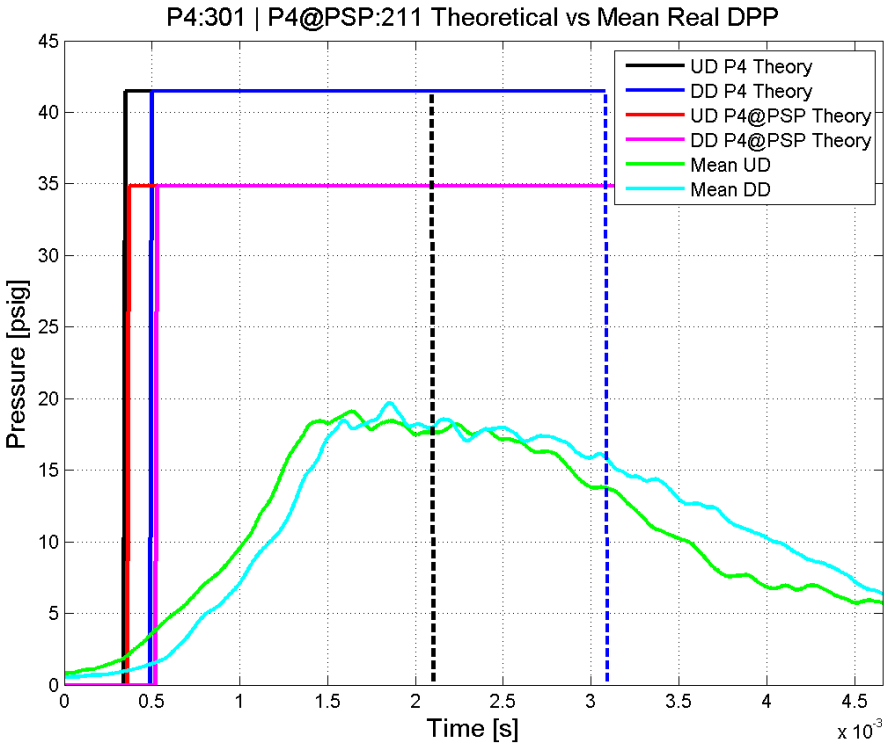
P4:301 | P4@PSP:211 Theoretical vs Mean Real DPP
UD P4 Theory
DD P4 Theory
UD P4@PSP Theory
DD P4@PSP Theory
Mean UD
Mean DD
Pressure [psig]
Time [s]
x 10^-3

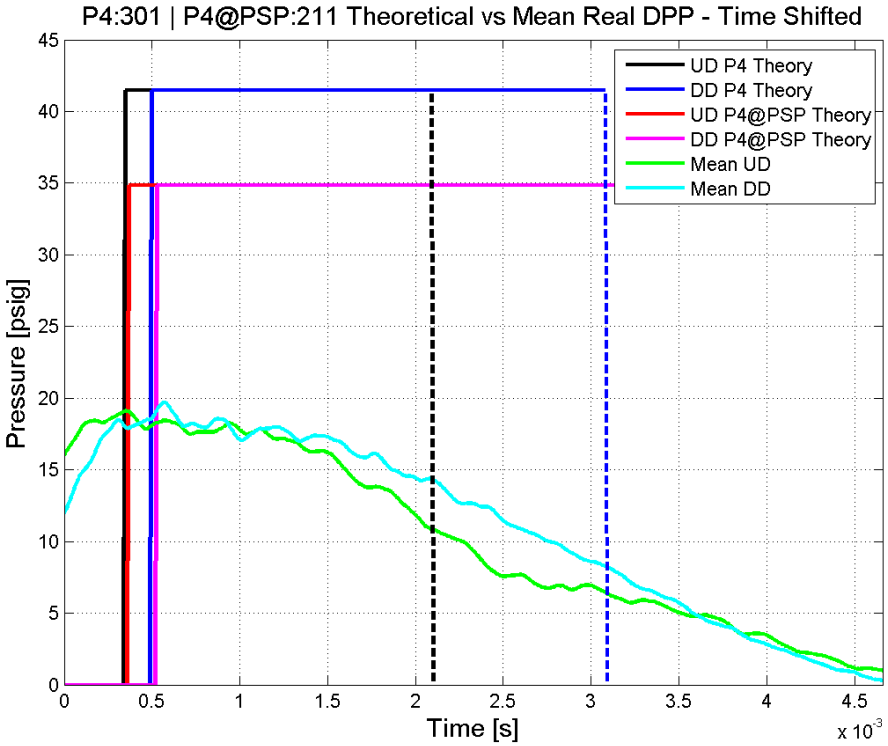
P4:301 | P4@PSP:211 Theoretical vs Mean Real DPP - Time Shifted
UD P4 Theory
DD P4 Theory
UD P4@PSP Theory
DD P4@PSP Theory
Mean UD
Mean DD
Pressure [psig]
Time [s]
x 10^-3

Mean Driver Gas Pressure (psig): 407.55 – Standard Deviation: 1.0505

Upstream Driven Transducer – Mean Temperature (K): 282.1 – Stan. Dev.: 1.3729

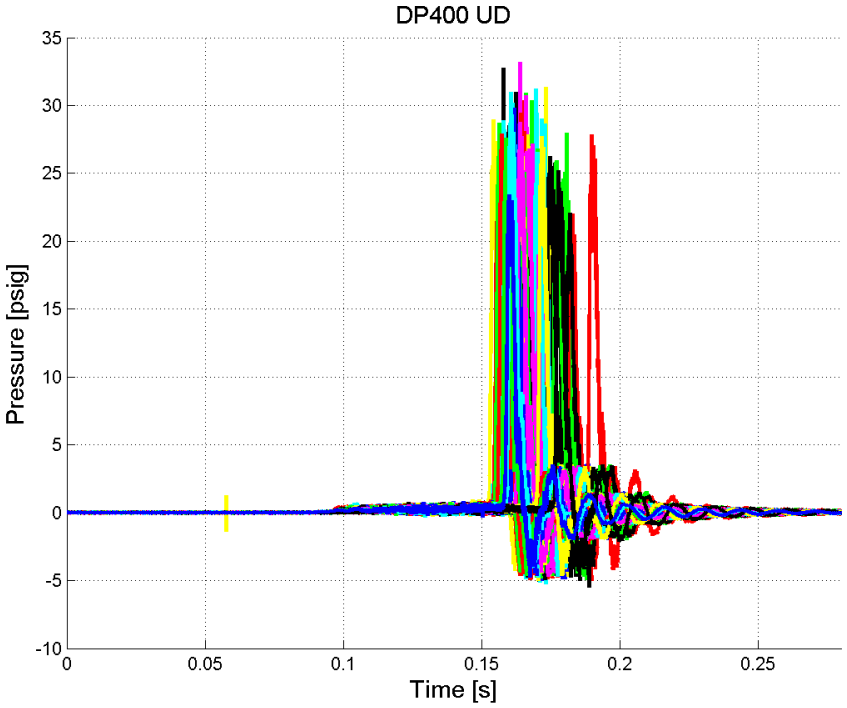

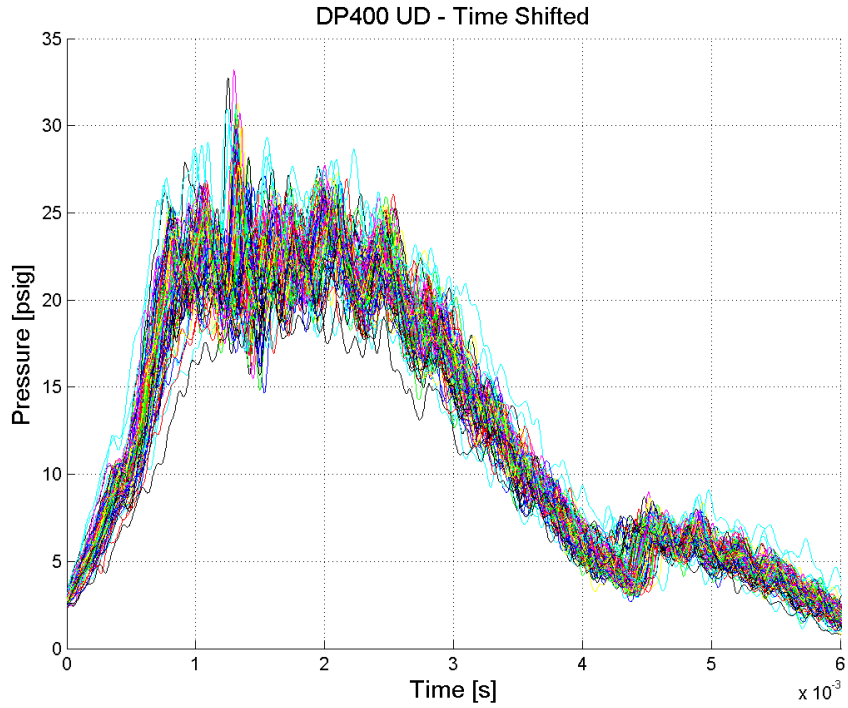

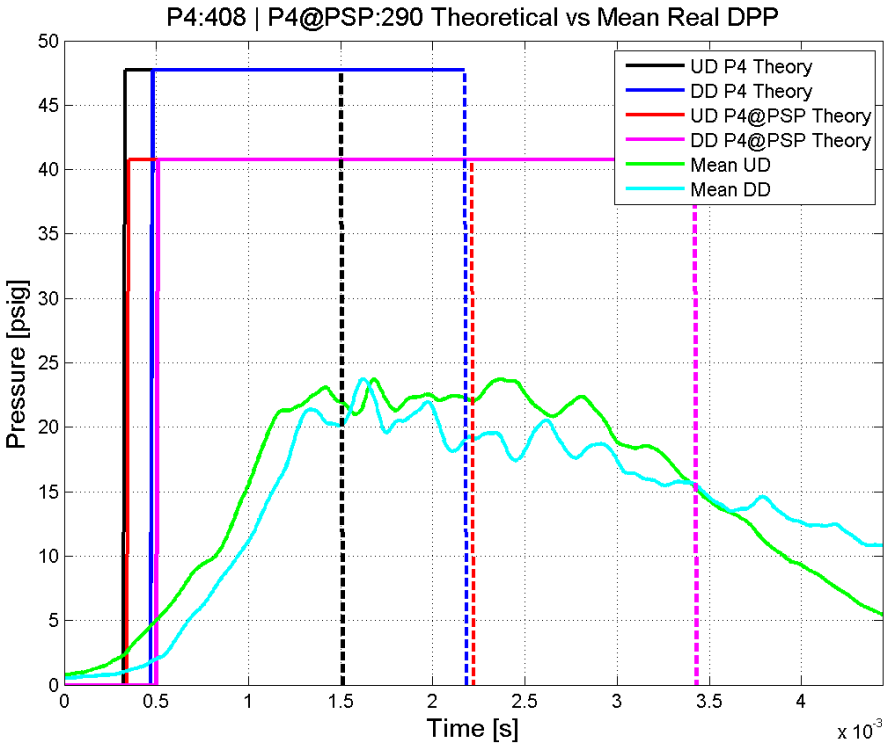
P4:408 | P4@PSP:290 Theoretical vs Mean Real DPP
UD P4 Theory
DD P4 Theory
UD P4@PSP Theory
DD P4@PSP Theory
Mean UD
Mean DD
Pressure [psig]
Time [s]
x 10^-3

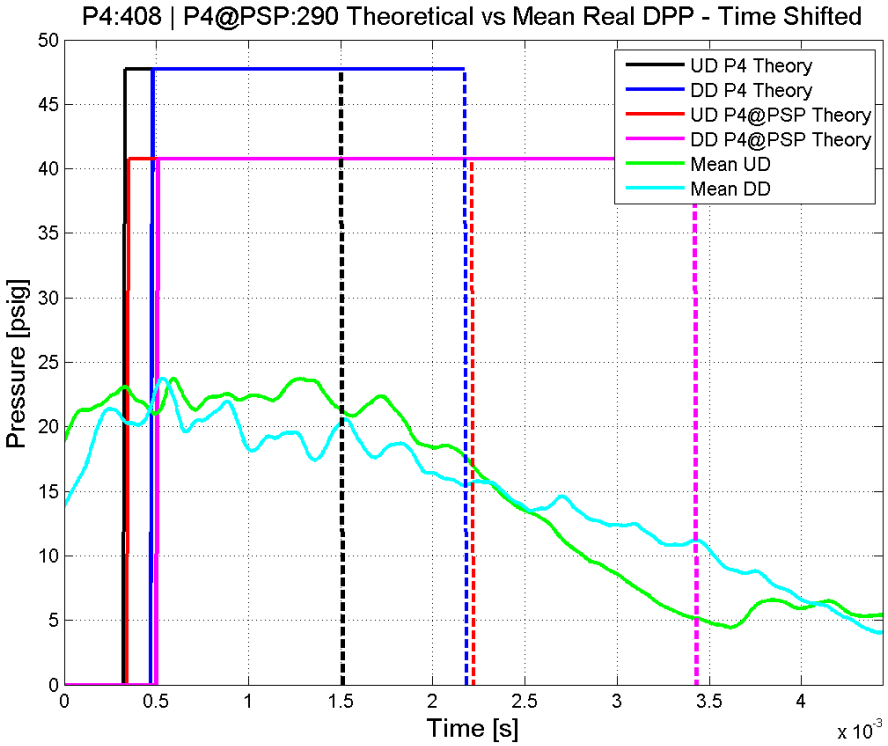
P4:408 | P4@PSP:290 Theoretical vs Mean Real DPP - Time Shifted
UD P4 Theory
DD P4 Theory
UD P4@PSP Theory
DD P4@PSP Theory
Mean UD
Mean DD
Pressure [psig]
Time [s]
x 10^-3

Mean Driver Gas Pressure (psig): 513.38 – Standard Deviation: 2.1634

Upstream Driven Transducer – Mean Temperature (K): 273.7 – Stan. Dev.: 1.7406

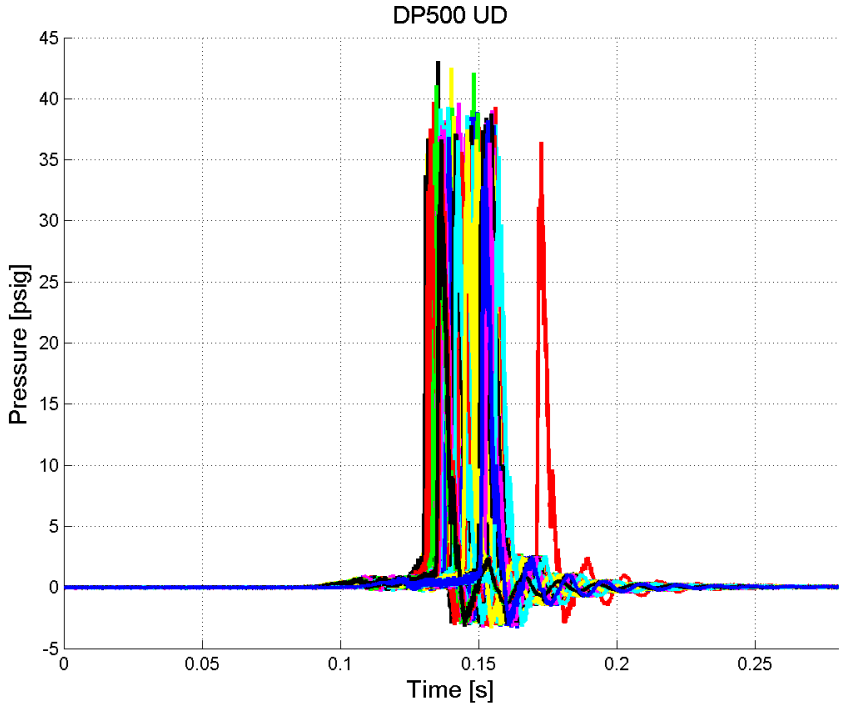

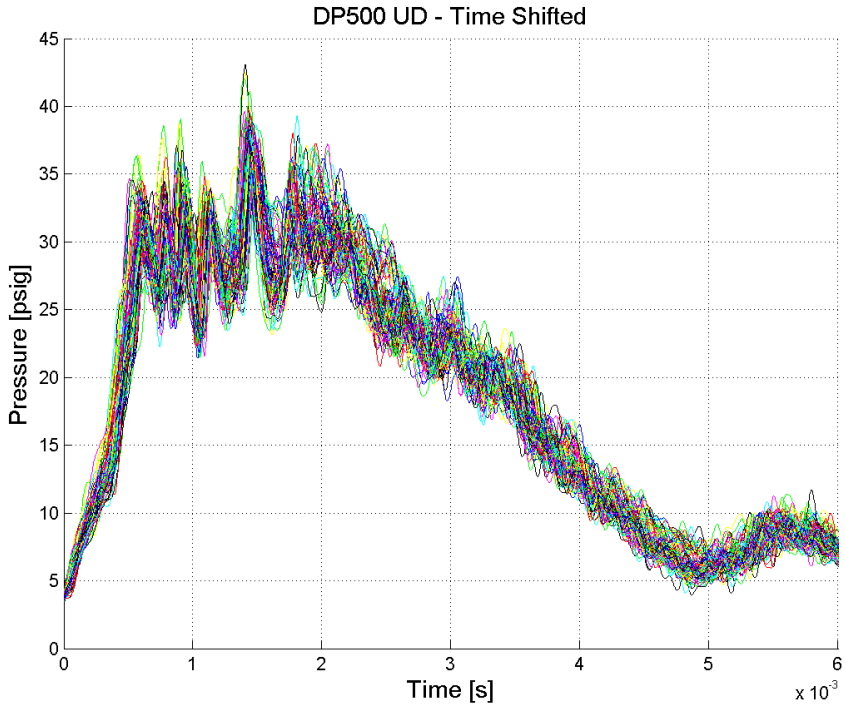

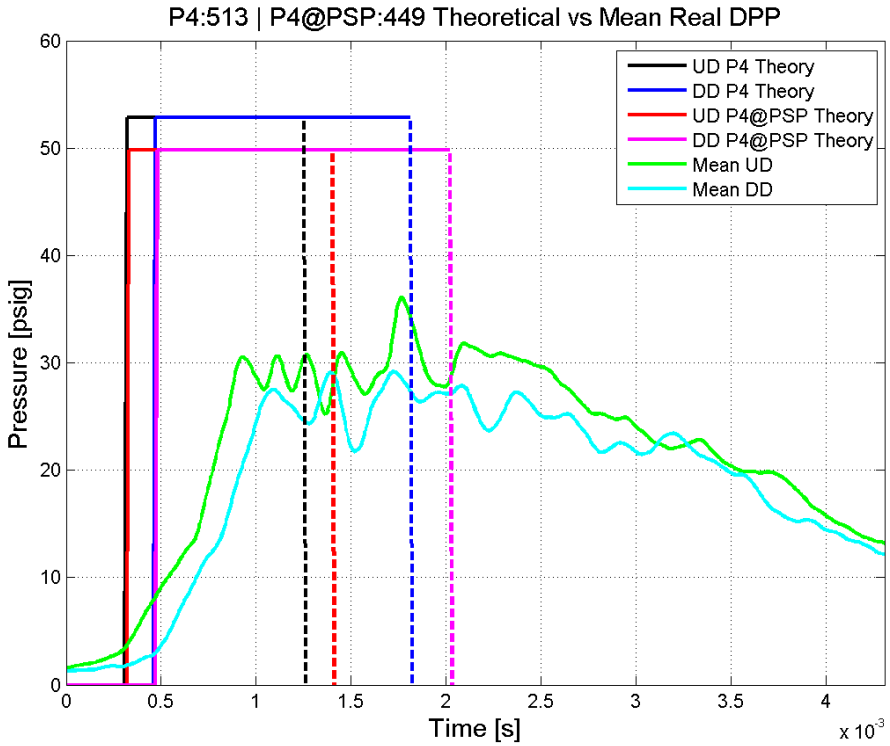
P4:513 | P4@PSP:449 Theoretical vs Mean Real DPP
UD P4 Theory
DD P4 Theory
UD P4@PSP Theory
DD P4@PSP Theory
Mean UD
Mean DD
Pressure [psig]
Time [s]
x 10^-3

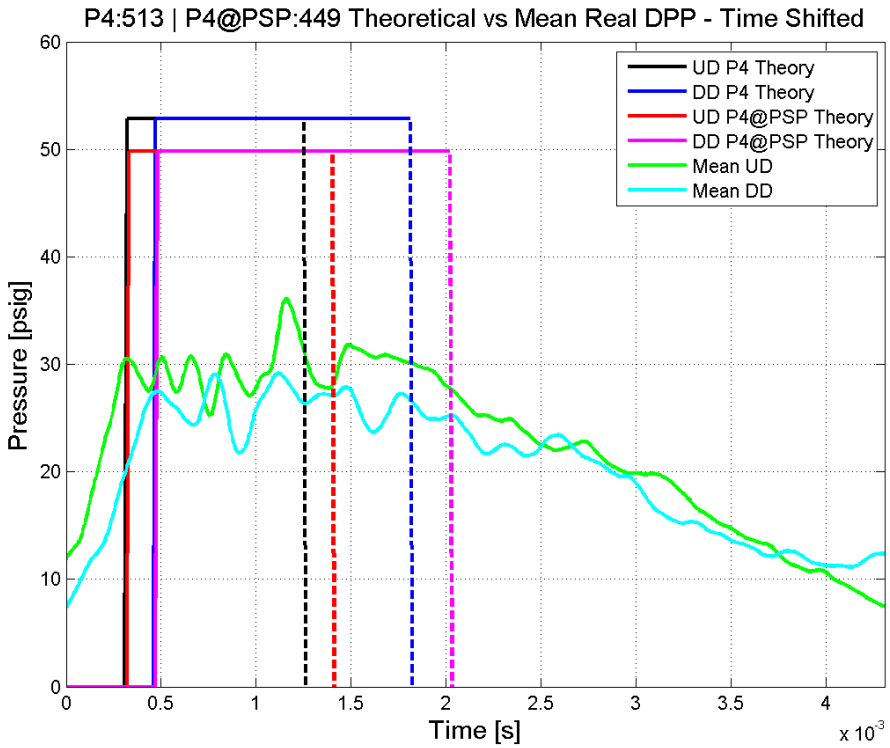
P4:513 | P4@PSP:449 Theoretical vs Mean Real DPP - Time Shifted
UD P4 Theory
DD P4 Theory
UD P4@PSP Theory
DD P4@PSP Theory
Mean UD
Mean DD
Pressure [psig]
Time [s]
x 10^-3

APPENDIX B

Start Up Procedure:

- NAL personnel check the test section and surrounding area to be cleared of any tools and/or loose items.
- Close the safety shield. Leave optical pathways open.
- Check that all Personnel are behind the safety glass and have hearing protection and safety glasses on.
- Lock doors to the NAL building to ensure no outside personnel accidently enter during a test.
- Turn safely light on and sound the alert siren to alert personnel outside of the NAL building that a test is being conducted.
- Turn off ambient lights if conducting a schlieren experiment.
- Open the Labview program and check all DAQ equipment is operating normally and all values are closed.
- Open camera control software and ensure the camera acquires images. Verify that light source and camera are triggered properly if conducting a schlieren experiment.
- Open air supply tanks and check pressure gauges.
- Start camera acquisition
- Run Labview program to actuate the servomotor, values, and record the pressure data.
- Run ACR program for the servomotor actuation (drive on x and run prog0)
- Press the Start Valves button in Labview program to Run Test.

Shutdown Procedures:

- Press the Shutdown button in the Labview program to close values and stop the motor.
- Press valve shutoff button to prevent the solenoid valve from opening
- Close air supply tanks.
- Vent air supply lines.
- Make sure the servomotor has stopped
- Turn off the servomotor (halt prog0 then drive off x)
- Turn off the camera if conducting a schlieren experiment.
- Ensure data was acquired and is backed up.
- Turn safely light off, ambient lights on, and unlock the doors to the NAL.

APPENDIX C

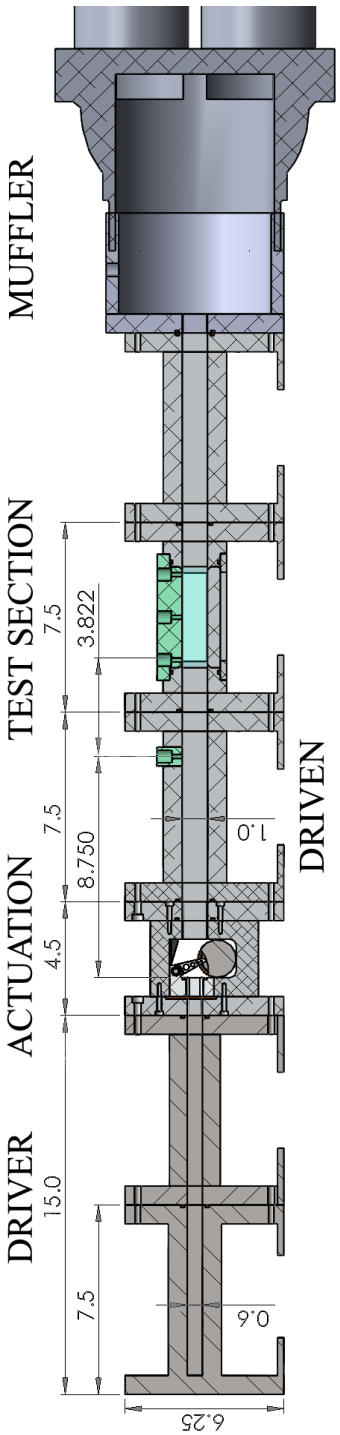
MUFFLER
TEST SECTION
ACTUATION
DRIVER
DRIVEN
7.5
3.822
7.5
8.750
4.5
15.0
7.5
1.0
0.6
6.25

APPENDIX D

Figure 32, illustrates pressure and time of the measured driver gas pressure and the measured driven gas pressure as functions of time. As one can see, when the servomotor allows the RD to open the driver gas starts to fall. However, the times scales indicates that the time between the beginning of fall of the driver gas pressure and the rise of the driven gas pressure is ~25 milliseconds, which is two orders of magnitude greater than predicted by ISTT. Therefore, the RD must have a finite opening time that enables the driver gas pressure to fall a non-negligible amount prior to being fully open.

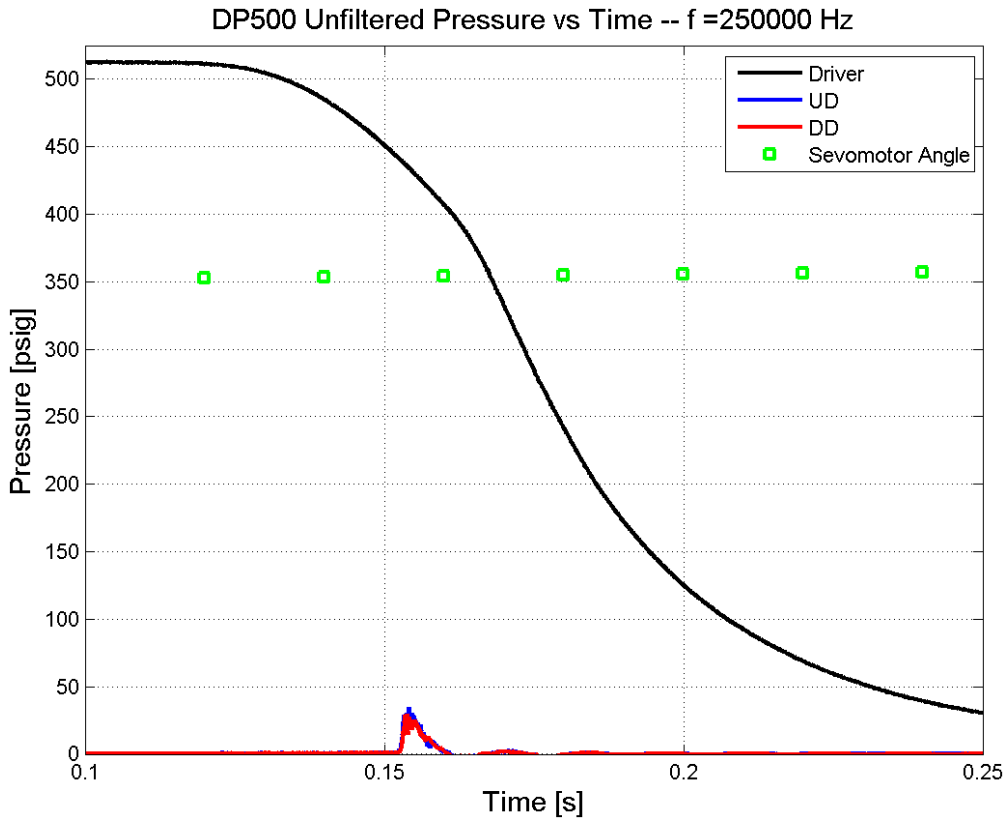

Figure 32 Driver and Driven Gas Pressures

APPENDIX E

As explained in Section 5.3.1, the calculated M_s is based on a pressure threshold parameter, where the only the driven gas pressure measurements within 30% to 70% of the first pressure rise are used to obtain a Δt. However, from Figure 29, the 30% to 70% pressure threshold parameter may need to change for each pressure region. In order to test this, the data was reprocessed using a pressure threshold parameter of 30% to 60%, where Figure 33 represents the new pressure threshold parameter. In Figure 33, the calculated M_s drops for those P4/P1s that are less than 30 and increases for those P4/P1s that are above 30. Additionally, the error bars seem to increase slightly. Therefore, the pressure threshold parameter is insentitive in producing accurate shock wave Mach numbers (M_s).

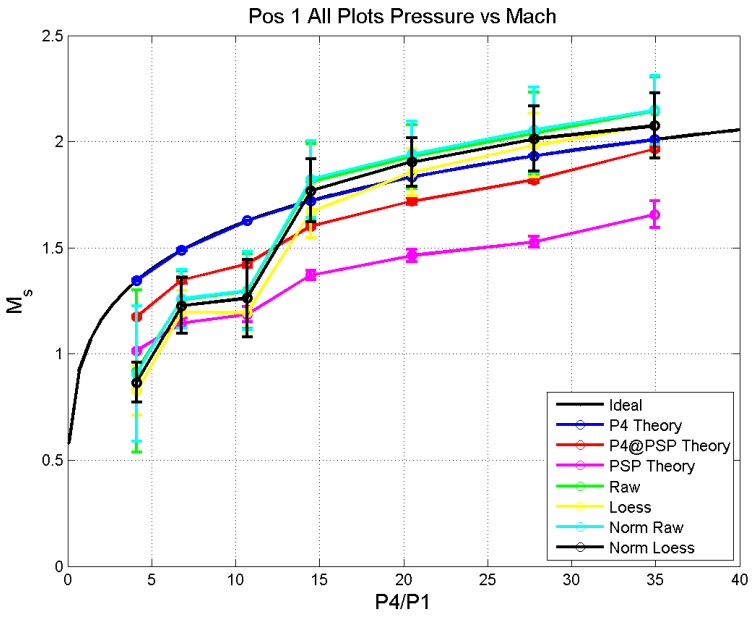

Figure 33 Performance – Threshold 30%-60%

APPENDIX F

During the final semester a schlieren setup was established, however due to space constraints a w-type setup was required, where

1. A 310 lumen LED shines light through a 2” condensing lens
2. That focused the light to a point onto a vertical slit made from two knife edges
3. The light expands and hits a 4” x5” rectangular first surface flat mirror
4. That reflects the light towards the f=48” 6” parabolic mirror
5. That collimates the light through the test section onto another f=48” 6”parabolic mirror
6. That focuses down to a point through the vertical knife edge
7. The light then expands past the vertical knife edge onto a 2” first surface flat mirror
8. That reflects the expanding light onto a 6.5” focusing optic
9. That focuses the light onto a cook cam PCO. 1600 camera through a 60 mm lens with a 20 mm extension ring

However, the main problem with this setup is that all of the optics were attached to the optics table of the Shock Generator thinking that if it moves, then all the optics thus would have no relative change in position. However, what really happened is that as the driver gas vacates the driver section the optics table vibrates such that the knife-edge moves into and out of the focal point. This results in some images being completely dark

from the knife-edge blocking the light and some images appearing as though there is no knife-edge. Furthermore, this vibrate occurs at driver gas pressures starting at 200 psig which is the lowest possible driver gas pressure in which the analysis suggests that a shockwave may be present. Additionally, this is complicated by the camera exposure time of 1 microsecond, which is necessary to keep the motion blur across the test section window around 1%.

Therefore, some possible improvement to the setup given above, are to use a proper point light source for schlieren, remove all optics from the optical table and attach them to floor stands that can absorb the vibrations that are transferred from the optics table to the floor.

VITA

Name: David Christopher Taylor

Address: Department of Aerospace Engineering
Texas A&M University
H.R. Bright Building, Rm. 701
3141 TAMU
College Station, TX 77843-3141

Email Address: DavidChristopherTaylor@gmail.com

Education: B.A., Aerospace Engineering, Texas A&M University, 2009
M.S., Aerospace Engineering, Texas A&M University, 2012